Summer 2019

Enhancing Thermal-Hydraulic Performance of Parallel and Counter Flow Mini-Channel Heat Sinks Utilizing Secondary Flow: A Numerical and Experimental Study

Amitav Tikadar

ENHANCING THERMAL-HYDRAULIC PERFORMANCE OF PARALLEL AND COUNTER FLOW MINI-CHANNEL HEAT SINKS UTILIZING SECONDARY FLOW: A NUMERICAL AND EXPERIMENTAL STUDY

by

Amitav Tikadar

Bachelor of Science
Bangladesh University of Engineering & Technology, 2015

Submitted in Partial Fulfillment of the Requirements

For the Degree of Master of Science in

Mechanical Engineering

College of Engineering and Computing

University of South Carolina

2019

Accepted by:

Jamil A. Khan, Director of Thesis

Chen Li, Reader

Titan C. Paul, Reader

Cheryl L. Addy, Vice Provost and Dean of the Graduate School

DEDICATION

This work is dedicated to the memory of my best friend, Mr. Mahamudul Hossain Sohel, who always inspired me through his hard work and brilliance. You are gone, but your support during my Bachelors has made this journey possible.

ACKNOWLEDGMENT

The author would like to express his sincere gratitude to his advisor, Prof. Jamil A. Khan, for his continuous support, encouragement, motivation, and guidance throughout all phases of this M.S. study in all these years. It has been a great privilege and honor for the author to work with him.

The author would like to thank his defense committee members, Prof. Chen Li, and Prof. Titan C. Paul, for their comments, suggestions, and time for reviewing this thesis.

The author would also like to thank his colleagues in the "Enhanced Heat Transfer Lab," Dr. Azzam S. Salman, Mr. Nabeel M. Abdulrazzaq, Mr. Nobbel Aumbee, and Mrs. Sowmya Raghu for their invaluable suggestions and comments during the research. Special thanks to Mr. Saad K. Oudah for his invaluable help to build up the experimental setup. The author would also like to acknowledge Dr. A.K.M. Monjur Morshed for his continuous support.

Finally, the author would like to thank his Father Dinesh Chandra Tikadar, Mother Mukti Rani Tikadar, all elder sisters Mrs. Binita Tikadar, Mrs. Eti Tikadar, and Mrs. Dipa Tikadar for their continuous support, patience and endless love.

ABSTRACT

Continual growth of hydraulic and thermal boundary layers along stream wise direction in conventional straight fin mini-channel heat sink causes gradual deterioration of their thermal performance. To enhance thermal-hydraulic performance by breaking and redevelopment of the boundary layers, this research aims to introduce a novel inter-connected mini-channel sinks. Two inter-connectors were positioned transversely between two adjacent mini-channels, which segmented the flow domain into three zones. Secondary flow was generated through the inter-connectors utilizing the pressure difference of the adjacent channels resulting in hydraulic and thermal boundary layers disruption and hence enhanced thermal-hydraulic performance of the mini-channel heat sink was achieved.

Firstly, this present work attempts to numerically analyze and compare the effects of inter-connectors width on the heat transfer and fluid flow behaviors of parallel and counter flow mini-channel heat sinks. Five different inter-connector width (case 1-5) were considered for a fixed inter-connector location (zones length). A corresponding conventional parallel flow mini-channel heat sink was chosen as the base case in contrast to the newly proposed inter-connected mini-channel heat sinks. The length, height, and width of the considered mini-channel heat sink were 26 mm, 0.5 mm, and 1.5 mm respectively, which provides a hydraulic diameter of 750 μm. Water was employed as the coolant, and the flow was in the single-phase regime under laminar flow condition at Reynolds numbers (Re) ranging from 150 to 1044. The non-dimensional pressure, velocity

temperature, friction factor, overall Nusselt number (Nu), and thermal resistance were calculated to evaluate the overall performance of the inter-connected mini-channel heat sink. Finally, the performance of the inter-connected mini channel was compared with the conventional parallel flow mini-channel by calculating the performance evaluation criteria (PEC). The results show that the inter-connector has negligible effect on the overall performance of the parallel flow mini-channel heat sinks because of the almost no transverse flow through the inter-connectors whereas, inter-connector has significant effect on the overall performance of the counter flow mini-channel heat sinks. For the counter flow mini-channel heat sink and for the highest considered inter-connectors width (case 5), Nu was enhanced by a maximum of 36% at $Re = 1044$ as compared to the conventional parallel flow mini-channel while a maximum of 31.13% reduction in friction factor was recorded at $Re = 150$. The PEC of the inter-connected counter flow mini-channel heat sink (case 5) went up to 1.33, and its value shows an increasing trend with as Re increases.

Secondly, to examine the combined effect of the inter-connectors width and location, i.e., zones length on the thermal-hydraulic characteristics of the counter flow mini-channel heat sink, the present numerical studies were carried out for nine different cases (case 1-9) by varying inter-connectors width and location. The results show that the amount of secondary flow reduces gradually as Re increases for any particular inter-connectors location and width. At the lowest considered Re ($Re = 150$), a maximum value of PEC was achieved to ~1.22 for the highest length of zone 1 and 3 and the lowest inter-connectors width (case 7), while at the highest Re ($Re = 1044$), the maximum PEC value (~1.42) was recorded for the intermediate length of zone 1 and 3 and the highest inter-connectors width (case 6).

Thirdly, to validate the numerical predictions, experimental investigations of heat transfer and fluid flow characteristics of conventional parallel and counter flow mini-channel heat sinks and also inter-connected parallel and counter flow mini-channel heat sinks were performed under laminar flow regime. For experimental analysis, numerically obtained optimum inter-connectors width, and location was chosen as fabrication parameters. The experimental heat transfer results for all the conventional and inter-connected mini-channel heat sinks show excellent agreement with the corresponding numerical results. On the contrary, experimentally obtained pressure drop were substantially less compared to the numerically predicted pressure drop, especially at low Re. Plausible reasons for the reduced pressure drop are discussed. Experimental results show that inter-connected parallel flow mini-channel heat sinks provide poor overall performance whereas inter-connected counter flow mini-channel heat sinks provide superior overall performance compared to the conventional parallel flow mini-channel heat sink.

TABLE OF CONTENTS

LIST OF TABLES

LIST OF FIGURES

LIST OF SYMBOLS

V	voltage, V
I	current, A
Q	heat, W
Q''	heat flux, $W.m^{-2}$
T	temperature, K
k	thermal conductivity, $W.m^{-1}.K^{-1}$
C_p	specific heat, $J.kg^{-1}.K^{-1}$
L	length, m
W	width, m
D_h	hydraulic diameter, m
A_c	cross-sectional area, m^2
u, v, w	velocity component in x, y, and z-direction
p	local pressure, Pa
Δp	pressure drop, Pa

h	convection heat transfer coefficient, $W.m^{-2}.K^{-1}$
P_p	pumping power, W
$\dot{Q}$	volumetric flow rate, $m^3.s^{-1}$
$\dot{m}$	mass flow rate, $kg.s^{-1}$
P_c	wetted perimeter, m
H	height, m
ΔX	distance, m
R	thermal resistance, $K.W^{-1}$
S	entropy generation rate, $W.K^{-1}$

Non-dimensional parameter

Re	Reynolds number
Nu	Nusselt number
f	friction factor
l	Length
α	aspect ratio
u_n, v_n, w_n	Velocity
P	Pressure

PEC	performance evaluation criteria
R	thermal resistance

Greek letters

ρ	density, $kg.m^{-3}$
μ	dynamic viscosity, $Pa.s$
θ	temperature

Subscript

eff	Effective
in	Inlet
out	Outlet
m	Mean
w, b	bottom wall
t	total base
p	Power
w	interface between solid and fluid
f	Fluid
fr	Friction

so	Solid
s	Substrate
c	cross-section
o	conventional channel
th	Thermal
min	Minimum
max	Maximum
t	Total
$cond$	Conduction
$conv$	Convection
cap	capacitance
i	inter-connector

"Imagination is more important than knowledge. Knowledge is limited. Imagination encircles the world."

-Albert Einstein

"If you shut the door to all errors, truth will be shut out."

-Rabindranath Tagore

"A man is but a product of his thoughts. What he thinks he becomes."

-Mahatma Gandhi

"Knowledge isn't power until it is applied."

"Remember, today is the tomorrow you worried about yesterday."

-Dale Carnegie

CHAPTER 1 INTRODUCTION

1.1 Motivation for the Study

In the last few decades, we are experiencing intense advancement of micro-electronic devices, and it is anticipated that this advancement will further boost up in the coming decades. As the micro-electronics industries advances in each generation, not only the number of transistors and functionality of the electronic devices increase but also the geometrical dimensions of those devices reduce gradually, hence the power density of the electronic devices increase dramatically. In 1965, the co-founder of Intel company, Gordon Moore first predicted the future growth trend of the electronic devices. He claimed that the number of transistors on a single chip would be doubled, and the physical dimensions of the transistors will be reduced by ~30% every two years [1], which has become the guideline for the micro-electronics industry, as illustrated by the CPU transistor count and feature size trend lines in Figure 1.1.

Due to the continual miniaturization of micro-electronic devices, intense circuit integrations, and increased power densities, conventional heat extraction techniques sometimes become inadequate. Therefore, an efficient cooling technology compatible with high heat flux generating micro-electronic devices is essential for the further development of these devices. To achieve high heat flux dissipation, numerous cooling technologies have been used for electro-mechanical devices. Among them, micro-channel heat exchangers have shown promising potential to serve this purpose because of their light

weight and high heat transfer area to volume ratio compared to other conventional cooling systems. Here by micro-channel heat sinks, we refer to channel with hydraulic diameters of 10 to 200 μm as classified by Kandlikar [3]

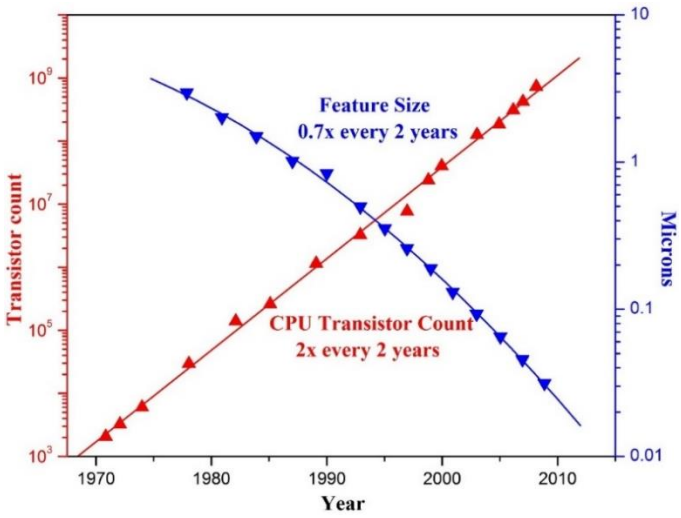

Figure 1.1: CPU Transistor count and feature size trend [2].

The concept of the micro-channel heat sink was first put forwarded by Tuckerman and Pease [4] in the early 1980s. The authors claimed that by reducing the hydraulic diameter, higher heat transfer coefficient could be achieved for the same Nusselt number value. For convective heat transfer in a channel having a hydraulic diameter of D_h, the heat transfer coefficient, h can be calculated as [5]:

$$h = \frac{Nuk_f}{D_h} \tag{1.1}$$

where k_f is fluid thermal conductivity of the coolant, and Nu is the Nusselt number for the appropriate flow condition. From equation 1.1, it can be seen that the higher heat transfer coefficient can be achieved by reducing the D_h, i.e., the channel size. To prove their claim, Tuckerman and Pease employed the direct circulation of water in rectangular

micro-channels fabricated into a 1 cm × 1 cm silicon chip [4]. The authors achieved a maximum heat flux dissipation of 790 W/cm^2 with a maximum substrate temperature to inlet water temperature difference of 71°C. However, the pressure drop encountered is very high, which is around 214 kPa.

Afterward, more detailed experimental and numerical investigations of the thermo-hydrodynamic characteristics of the micro-channel heat sink in laminar and turbulent flow regimes were performed by Phillips [6]. Since their pioneering work, micro-channel heat sink has drawn significant attention by the electronics industry as a long-cherished solution of high heat dissipation problems from the electronic devices. To date, several attempts have been reported to predict the thermal and hydraulic performance of a parallel flow micro-channel heat sink both experimentally and numerically [7-12]. Although almost all of the researchers reported superior thermal behaviors of micro-channel heat sinks compared to the convention heat sinks, at the same time, they identified some common limitations of the micro-channel heat sinks such as:

- High pumping power requirement.

To maintain a certain flow rate through a channel, the required pumping power can be calculated by using the following equation [13],

$$P_p = \Delta p v A_c = \frac{1}{2}\rho v^3 f \frac{L}{D_h} A_c \tag{1.2}$$

Where Δp is the pressure difference, A_c is the channel cross-sectional area, ρ is the fluid density, v is the fluid velocity, L is the channel length, and f is the friction factor. For fully developed laminar flow in a square channel, the friction factor, f can be written as follows:

$$f = \frac{56.8}{Re} = \frac{56.8\mu}{\rho v D_h} \quad (1.3)$$

Where Re is the Reynolds number, μ is the fluid dynamic viscosity.

By combining the equation (1.2) and (1.3),

$$P_p = 32u^2 \frac{L}{{D_h}^2} A_c \quad (1.4)$$

For a constant coolant velocity, v, $P_p \propto \frac{1}{{D_h}^2}$.

Since pumping power is inversely proportional to the square of the hydraulic diameter, therefore for reduced hydraulic diameter, i.e., micro-channel, pumping power is significantly higher compared to the conventional channel.

- Temperature non-uniformity along the channel wall because of the continuously growing thermal boundary layer.

When any coolant flows through a heated pipe, thermal boundary layer grows continuously along the flow direction, as shown in Figure 1.2. The thickness of the boundary layer increases in the developing flow regimes and reaches a constant thickness in the fully developed flow region. Since the thermal boundary layer works as resistance to heat transfer, therefore the wall temperature increases gradually along with the flow directions as shown in the Figure 1.2, which eventually creates high temperature non-uniformity along the heat sinks.

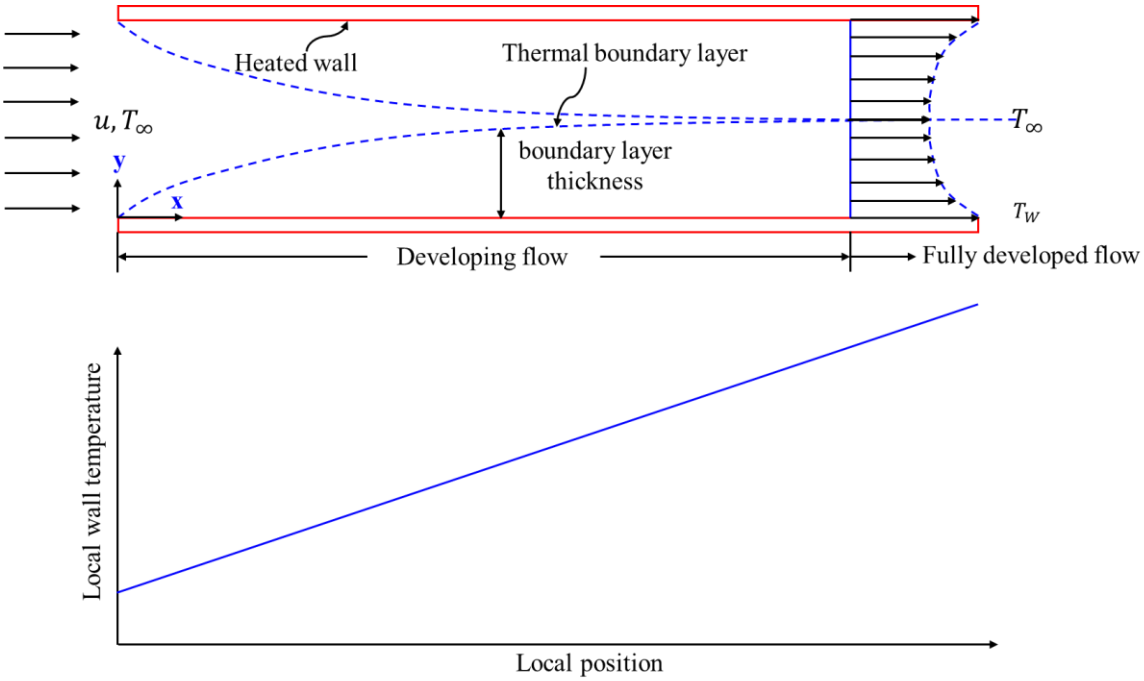

Figure 1.2 Thermal boundary layer and the corresponding local wall temperature profile (figure is not drawn to scale).

For practical applications, a significant reduction in pumping power requirement can be achieved by increasing the hydraulic diameter of the channel, i.e., by using mini-channel heat sink as an alternative of the micro-channel heat sink which offers comparable heat transfer coefficient with reasonably lower penalties of the pumping power requirements than the micro-channel heat sink. As per Kandlikar's [3] classification, a channel having a hydraulic diameter in the range of 200 μm to 3mm can be referred to as a mini-channel. Dang et al. [14] compared between mini and micro-channel heat sink both experimentally and numerically regarding heat transfer performance and the required pumping power. The authors concluded that mini-channel heat sink could be a good alternative to micro-channel heat sink due to lower pumping power requirement. To date, many strives have been made to study the overall performance of the mini-channel heat sinks [15-18]. Most of the researchers reached a general conclusion that the reduction of

pumping power requirement by using conventional mini-channel heat sinks can be offset by higher thermal boundary layer thickness compared to the conventional micro-channel heat sinks.

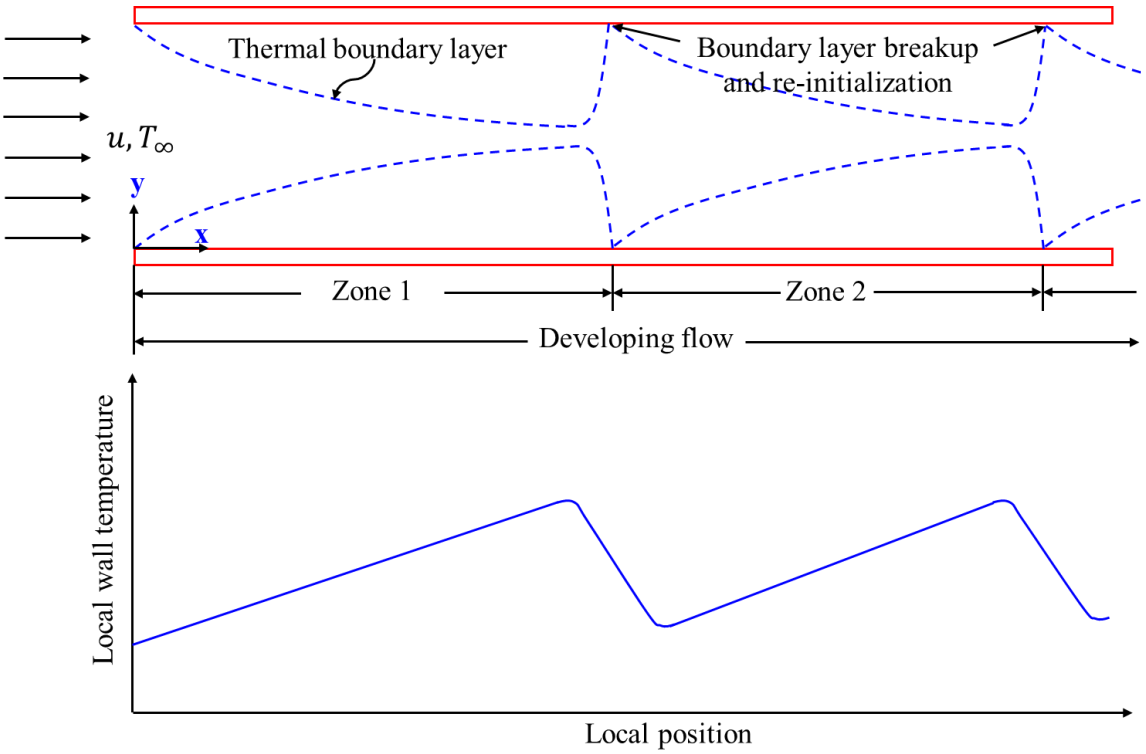

Figure 1.3 Disrupted thermal boundary layer and the corresponding local wall temperature profile (figure is not drawn to scale).

Continual growth of hydraulic and thermal boundary layers along stream wise direction in conventional micro/mini-channel heat sink causes temperature non-uniformity along the flow direction and eventually causes gradual deterioration of the thermal performance as discussed earlier. Therefore, by disrupting and re-initializing the thermal boundary layers in separate zones before the fully developed regime in micro/mini-channel heat sinks can ensure thermally developing flow in each zones along the coolant flow

direction resulting in more uniform surface temperature distribution and hence improved overall heat transfer performance as depicts in Figure 1.3.

Breakup of the boundary layers in the micro and mini-channel heat sinks and hence improved thermal performance can be potentially achieved by two different cooling approaches such as active and passive cooling approaches. In active cooling, some external power is needed in the form of external flow pulsation [19], synthetic jet [20], micro-nozzle [21], vibration, or electrostatic fields. Active heat transfer augmentation methods have lost their effectiveness because of the external power requirements. On the contrary, in the case of passive cooling, heat transfer performance of the micro and mini-channel heat sink can be enhanced by modifying the geometry [22-23], surface roughness [24-25], by enhancing coolant thermo-physical properties, i.e., by using nanoparticles in the coolant [26-27], channel curvature [28], and re-entrant obstructions [29] as studied by Kandlikar et al. [30]. Although improved heat transfer performance can be achieved by utilizing the passive heat transfer enhancement techniques, at the same time pumping power requirement increases significantly for the flow disruption, i.e., flow resistance compared to the conventional channel.

Therefore, to enhance heat transfer passively by using boundary layer re-developing concept and without increasing the pumping requirement, Xu et al. [31] introduced the concept of the transverse flow by utilizing the secondary channel. To enable transverse flow in-between parallel micro-channel, they fabricated some transverse micro-channels in-between parallel longitudinal micro-channels. Enhanced thermal performance, along with the reduced pumping power requirement was reported by the authors due to flow disruption and re-initialization of the thermal boundary layer in the junction of

longitudinal and transverse micro-channel. Afterward, numerous studies [32-33] have been conducted to quantify the effect of secondary channel on the thermo-hydrodynamic performance of parallel flow mini and micro-channel heat sink. One major disadvantage of the parallel flow mini/micro-channel heat sinks equipped with secondary channels is that the same coolant flow direction through the neighboring channels gives negligible pressure difference across the secondary channels and eventually reduces the secondary flow.

1.2 Research Goal and Objectives

In this study, we demonstrate the enhancement of heat transfer and the reduction in pressure drop by employing inter-connected counter flow mini-channel heat sink where inter-connectors servers as secondary channels. Hence the main objective of this study is to generate secondary flow through the inter-connector by using the pressure difference between two adjacent counter flow mini-channels and to investigate the effect of the secondary flow on the thermal and hydraulic performance of counter flow mini-channel heat sink and also make a comparison with the inter-connected parallel flow heat sink. A parametric study has been performed numerically to find the optimum inter-connectors width and location based on the thermal and hydraulic performance, and finally, experimental validation has been performed for the optimized inter-connected mini-channel heat sink.

The objective and specific task of this research are divided into the following sections:

1. Numerically studied the effect of five different inter-connectors widths for a specific location on the overall thermal-hydraulic performance of the mini-

channel heat sinks. The effect of inter-connectors on the overall performance of the parallel and counter flow mini-channel heat sinks will be compared and also optimum inter-connectors width will be identified.

2. Numerically studied the combined effect of the inter-connectors width and location on the heat transfer and fluid flow behaviors of the counter flow mini-channel heat sink. Three different inter-connectors locations and for each location, three different inter-connectors widths will be considered. Optimum inter-connectors location and width will be identified.
3. Conducted experimental study to quantify the thermal-hydraulic performance of the numerically optimized inter-connected mini-channel heat sink. Numerical results will be validated with the experimental findings.

1.3 Thesis Layout

CHAPTER 2 presents a critical review of the passive heat transfer enhancement techniques for micro/mini-channel heat sinks.

CHAPTER 3 illustrates the theoretical background of the parallel and counter flow mini-channel heat sinks along with their approximate pressure distribution. This chapter also summarizes the possible reasons of the secondary flow through the inter-connectors for the parallel and counter flow mini-channel heat sinks.

CHAPTER 4 comprises the computational domain, geometric parameters for five inter-connectors widths, detail numerical procedures, numerical model validations, and comparative pressure drop and heat transfer results for all five inter-connected parallel and counter flow mini-channel sinks. Optimized inter-connectors widths are also identified based on the overall performance of the inter-connected heat sink.

CHAPTER 5 includes the physical dimensions of the three different inter-connectors locations and three different inter-connectors widths, the combined effect of inter-connectors location and width on the overall performance of the counter flow mini-channel heat sinks. Optimized inter-connectors location and width are also identified based on the overall performance of the inter-connected counter flow mini-channel heat sink.

CHAPTER 6 includes the experimental facilities including the flow loop, power supply, data acquisitions system, test section assembly, experimental data reduction, experimental procedures and the experimental heat transfer and pressure drop results for parallel and counter flow mini-channel heat sink. In this chapter, numerical results are also compared with the experimental results.

CHAPTER 7 presents the conclusion of the numerical and experimental findings.

Finally, CHAPTER 8 presents suggestions for future research.

CHAPTER 2 LITERATURE REVIEW

2.1 Introduction

Although mini-channel heat sinks provide superior thermal-hydraulic performance over the overall performance of conventional heat sinks, however, continual growth of the thermal and hydraulic boundary layers causes gradual deterioration of the overall performance of the mini-channel heat sinks. Therefore, the overall performance of the mini-channel heat sinks can be enhanced by disrupting the thermal and hydraulic boundary layers which can be achieved by two different heat transfer enhancement approaches such as active and passive cooling enhancement approaches. In active cooling enhancements techniques, external power is required to disrupt the boundary layers. These external power requirements make active heat transfer enhancements techniques less attractive for practical applications. On the contrary, in passive cooling techniques, instead of using external power, boundary layer disruption can be achieved by employing surface roughness or secondary flow. In case of practical application, passive enhancement techniques are more viable because of no external power requirements. The following section summarize previous studies that have been performed on the passive heat transfer enhancement for single-phase mini-channel channel heat sinks. Since these techniques arevery similar for both mini and micro-channel heat sinks, the literature survey was not only limited to the mini-channel heat sinks.

2.2 Passive Heat Transfer Enhancement Techniques

In case of passive cooling, breakup and redevelopments of the thermal and hydraulic boundary layers and hence enhanced heat transfer performance of the micro and mini-channel heat sink can be achieved by employing surface roughness, modifying the geometry, coolant thermo-physical properties, flow disruption, secondary flows, channel curvature, re-entrant obstructions, and out of plane mixing. Figure 2.1 summarizes all passive heat transfer augmentation techniques as stated by Kandlikar et al. [30].

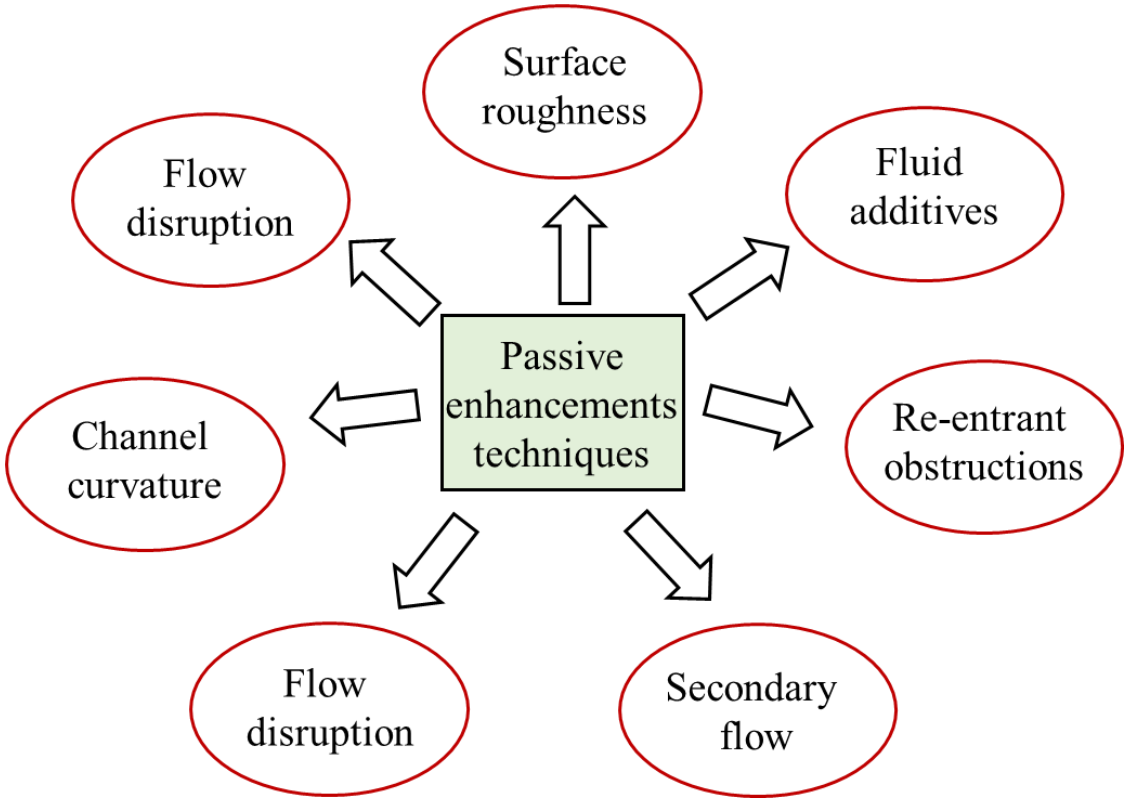

Figure 2.1 Passive heat transfer enhancement techniques [30].

2.2.1 Surface Roughness

The inclusion of surface roughness is perhaps the most attractive technique for micro/mini-channel heat sinks. Till date, numerous experimental and numerical studies

have been performed to quantify the effect of surface roughness on the thermal and hydraulic performance of the mini/micro-channel heat sinks. For example, Saad et al. [34] modified the bottom surface of the micro-channel heat sinks by knurling to break the thermal and hydraulic boundary layers within laminar flow regimes, as shown in Figure 2.2. The authors considered two different knurling height such as 0.25 mm and 0.17 mm for a constant pitch of 1 mm and the angle of corrugation of 45^{o}. The experimental results showed a maximum 255% increment of Nusselt number, while the friction factors increased by 360% compared to the conventional micro-channel at $Re = 500$ and for the knurling height of 0.25mm. Moreover, for the knurling height of 0.17 mm, Nusselt number and friction factor increased by a maximum ~68% and ~100% respectively at $Re = 500$.

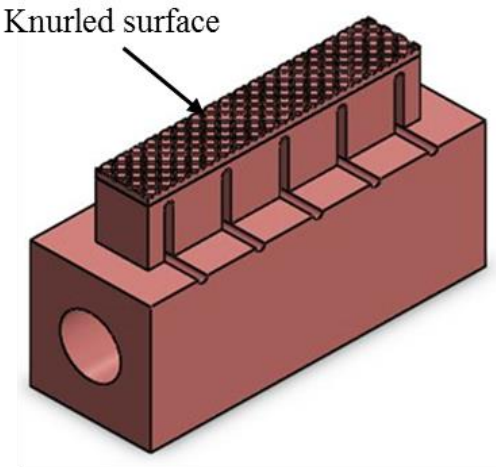

Figure 2.2 Knurled micro-channel heat sink [34].

The same group [35] also experimentally studied the thermal-hydraulic performance of hybrid sand-blasted (of elliptical patterns), and fully sand-blasted micro-channel heat sinks and compares with the overall performance of the conventional micro-channel heat sink. The authors reported that hybrid sand-blasted and fully sand-blasted

surface roughness improved the Nusselt number up to ~11-14% and ~2.5-9.55% respectively whereas the pressure drop increased by ~10% for both modified micro-channel heat sinks within a Reynolds number range of 85-650.

Xu et al. [36] numerically studied the effectiveness of micro-channel heat sinks with the dimpled surface at a constant Reynolds number of 500. The authors also examined the effect of dimple depth and dimple spacing on the overall performance of the micro-channel heat sinks. In comparison to the flat micro-channel heat sink, the dimpled micro-channel heat sinks reduced the surface temperature by 3.2 K and hence enhanced the Nusselt number by ~15%. Surprisingly the dimpled micro-channel heat sinks reduced the pressure drop requirement by 2% compared to the conventional micro-channel heat sink.

The characteristics of fluid flow and heat transfer in grooved micro-channel heat sink have been reported by Hamdi et al. [37]. The authors optimized the micro-channel heat sinks using triangular, trapezoidal, and rectangular grooves and by varying four geometry variables such as the depth, tip length, pitch, and orientation of the all shaped cavities. Their results demonstrated that the trapezoidal groove gave less stagnation region and provided a larger heat transfer surface area compared to the other two grooves. Consequently, the micro-channel heat sink equipped with trapezoidal grooves enhanced the computed Nusselt number up to 51.59% and increased the friction factor by only 2.35% compared to the conventional micro-channel.

The effects of sawtooth-shaped surface roughnesses on air and water flow through rectangular mini-channels with hydraulic diameters ranging from 325μm to 1819 μm for both laminar and turbulent flow regimes were investigated by Schmitt [38]. The authors considered two different surface roughness profile such as aligned sawtooth-shaped

roughness profile and offset sawtooth-shaped roughness profile. The aligned sawtooth roughness profile had the roughness elements lined up peak to peak, while the offset sawtooth roughness profile had the roughness elements lined up the peak to trough. The experimental results showed that aligned peak to peak roughness profile provided significantly higher friction factors compared to the offset peak to trough configuration.

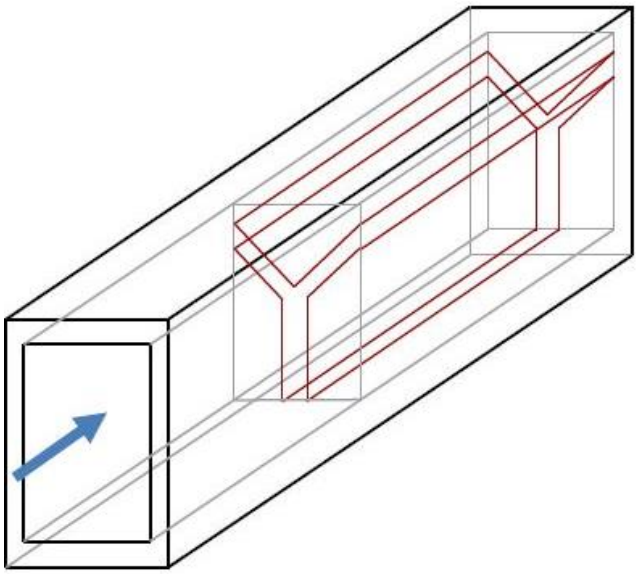

Figure 2.3 Micro-channel with Y-shaped bifurcation [39].

Xie et al. [39-40] designed a vertical Y-shaped bifurcation plates and inserted in the flow domain of a micro-channel to break-up the thermal and hydraulic boundary layer and also to enhance the heat transfer area as shown in Figure 2.3. The authors numerically optimized the length and the angle between the two arms of the Y profile based on the overall thermal-hydraulic performance. The numerical results showed noticeable improvement of the thermal performance of the modified heat sink, but at the same time, bifurcation plates increase the pressure drop dramatically which leads to a poor overall thermal-hydraulic performance compared to the conventional micro-channel heat sink.

Although improved thermal performance can be achieved by employing surface roughness in the micro/mini-channel heat sink, higher penalty of pressure drops, i.e., pumping power diminishes the effectiveness of the surface roughness in practical applications.

2.2.2 Channel Curvature

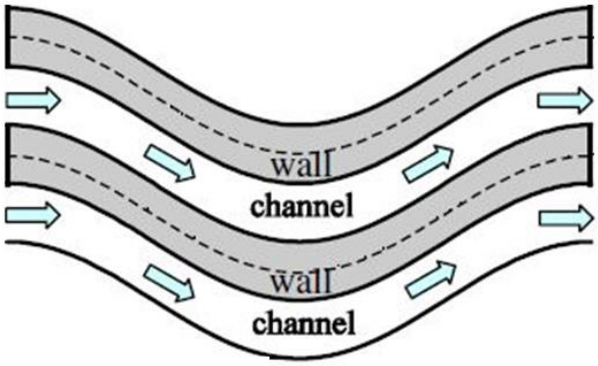

Figure 2.4 Wavy microchannel heat sink [41].

To compute the effect of three-dimensional channel waviness on the heat transfer and fluid flow behavior of a micro-channel heat sink, Sui et al. [41] developed a CFD model for a compact wavy micro-channel as shown in Figure 2.4. Flow field analysis showed that Dean vortices developed when liquid coolant flowed through the wavy microchannels, which results in chaotic mixing. Thus, the wavy microchannels heat sink provided significantly higher the heat transfer performance with a much smaller pressure drop penalty, as compared to straight baseline microchannels. The authors also suggested high relative waviness at high heat flux regions to increase the local heat transfer performance. Similar findings for wavy micro-channel heat sink were also reported by Mohammed et al. [42].

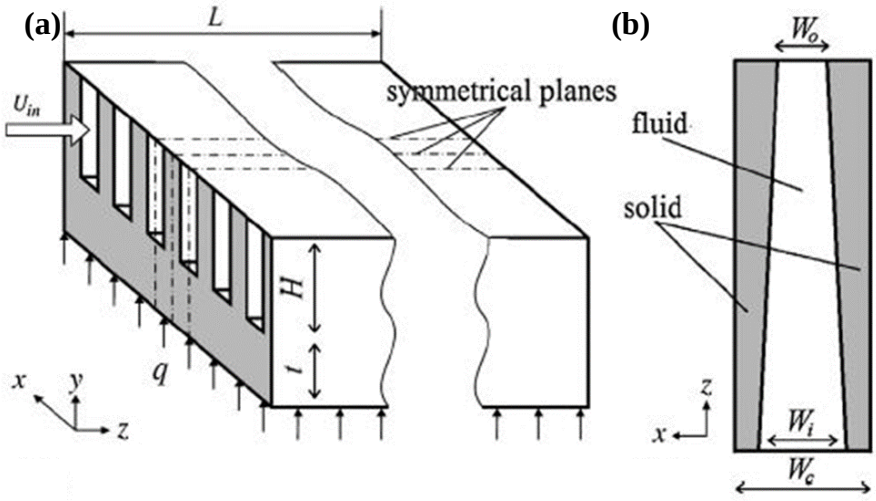

Figure 2.5 (a) Isometric, and (b) top view of the converging micro-channel heat sink [43].

Dehghan et al. [43] numerically studied and compared the fluid flow and conjugate heat transfer performance of converging micro-channel heat sink with the conventional straight micro-channel heat sink using the finite volume method (FVM) in the laminar regime. Figure 2.5 shows the schematic of the converging micro-channel heat sink. The authors examined the thermal performance of the converging micro-channel by varying the tapering configuration for a maximum pressure constraint of 3000 Pa across the micro-channel. The numerical results depicted that the width tapered ratio of 0.5 gives optimum heat transfer performance, in particular, for this tapering configuration, the pumping power reduced by a factor of 4 while the overall heat removal rate was kept fixed in comparison with a straight micro-channel.

Experimental and three-dimensional numerical investigation of single-phase fluid flow and heat transfer in diverging and converging micro-channels were carried out by Duryodhan et al. [44] for mass flux and heat flux range of 113–1200 kg/m^2.s (Re = 30–

274) and 0.3–9.5 W/cm^2 respectively as shown in Figure 2.6. The hydraulic diameter and divergence angle of the tested micro-channel were 156 μm and 8^o, respectively. Experimental and numerical results showed more uniform heat flux distribution and 35% higher heat transfer coefficient for converging micro-channel compared to the diverging microchannel. Surprisingly, the authors reported less pumping power requirement in diverging and converging micro-channels as compared with uniform cross-section microchannel.

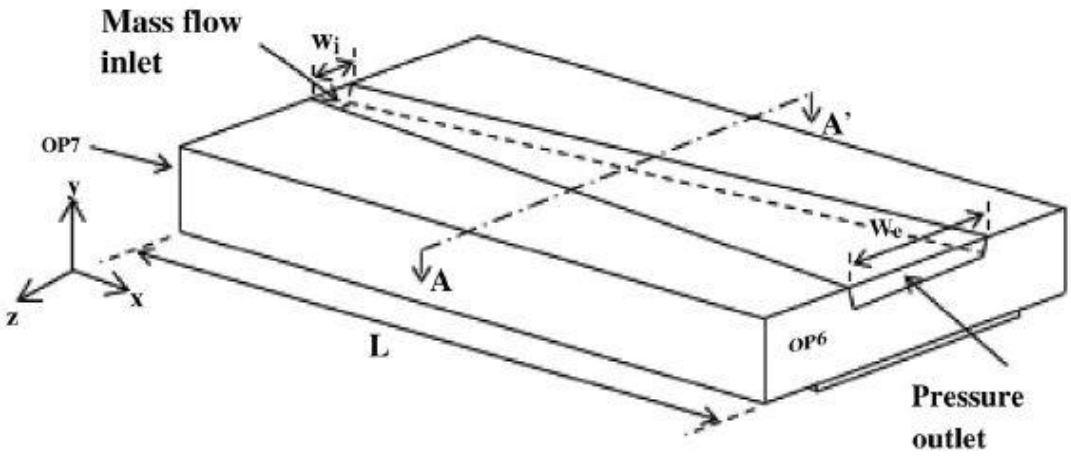

Figure 2.6 Diverging micro-channel heat sink [44].

Similarly, Ghaedamini et al. [45] introduced a planar converging-diverging micro-channel heat sink and numerically studied different geometric parameter such as aspect ratio, waviness, and expansion factor on the overall thermal-hydraulic performance under laminar flow regime. The authors reported significantly superior overall performance for converging–diverging design compared to the conventional channel especially at higher Re and they identified chaotic advection as the possible reason.

2.2.3 Reentrant Cavities

The effect of triangular reentrant cavities on water flow and heat transfer characteristics of the micro-channel heat sink was numerically investigated by Xia et al. [46] as shown in Figure 2.7. They also optimized the physical dimensions of the re-entrant cavities based on the overall performance of the modified micro-channel heat sinks. The authors claimed that the triangular re-entrant cavities not only accelerate the mixing but also interrupt and periodically redevelop the thermal and hydraulic boundary layers along the flow path. In addition, the vortices which were formed inside the triangular re-entrant cavities has led to chaotic convection and greatly improve the heat transfer performance compared to the conventional channel.

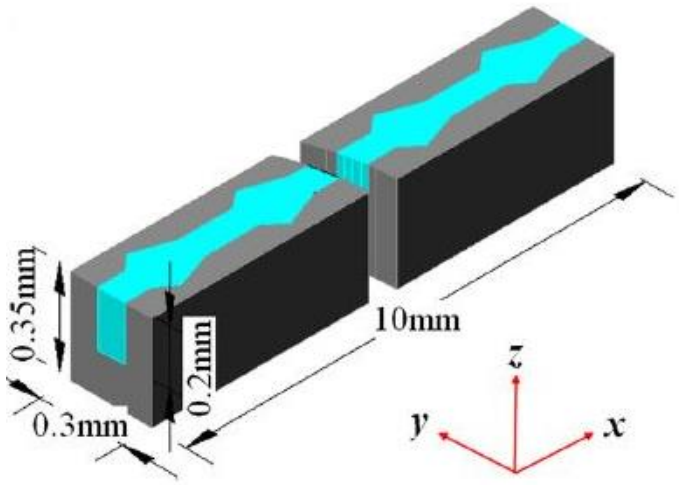

Figure 2.7 The micro-channel with triangular re-entrant cavities [46].

Later, the same group [47] numerically studied the thermal-hydraulic characteristics of a micro-channel heat sink with aligned fan-shaped re-entrant cavities. Figure 2.8 shows the micro-channel heat sink with aligned fan-shaped re-entrant cavities. For the re-entrant cavities, they considered different structural parameters such as the

different lengths and widths of the constant cross-section region and the arcuate region. The authors attributed to the interaction of the increased heat transfer surface area, the redeveloping boundary layers, the jet, and throttling effect as the possible reasons of enhanced heat transfer performance and pressure drop requirements of the micro-channel heat sink with aligned re-entrant cavities. On the contrary, the slipping over the reentrant cavities reduced the friction factor, but extremely impeded the heat transfer.

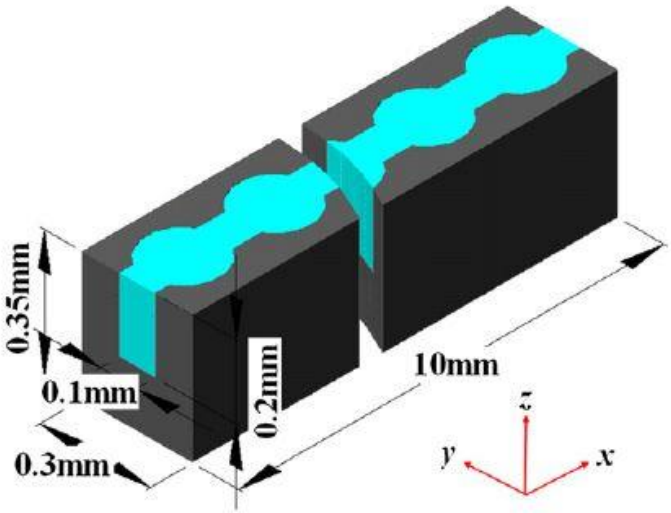

Figure 2.8 The microchannel with aligned fan-shaped reentrant cavities [47].

Numerical investigation of fluid flow and heat transfer in a micro-channel heat sink with offset fan-shaped re-entrant cavities in sidewall was performed Chai et al. [48] as shown in Figure 2.9 under laminar flow regime ($Re = 138 - 880$). The length, height, and width of their considered micro-channel heat sink were 10 mm, 200 μm, and 100 μm respectively, which provides a hydraulic diameter of 133.3 μm. The space between two adjacent fan-shaped reentrant cavities was 290 μm, and the field angle of the fan-shaped reentrant cavity was 120°, and the radius was 100 μm. The numerical results showed that

at smaller Re, the friction factor of the modified heat sink was significantly lower compared to the conventional micro-channel heat sink. However, the friction factor value increased significantly as Re increased. The authors also claimed improved heat transfer performance for the micro-channel heat sink with offset fan-shaped re-entrant cavities because of the combined effects of increased heat transfer surface area, and the thermal and hydraulic boundary layer breakup.

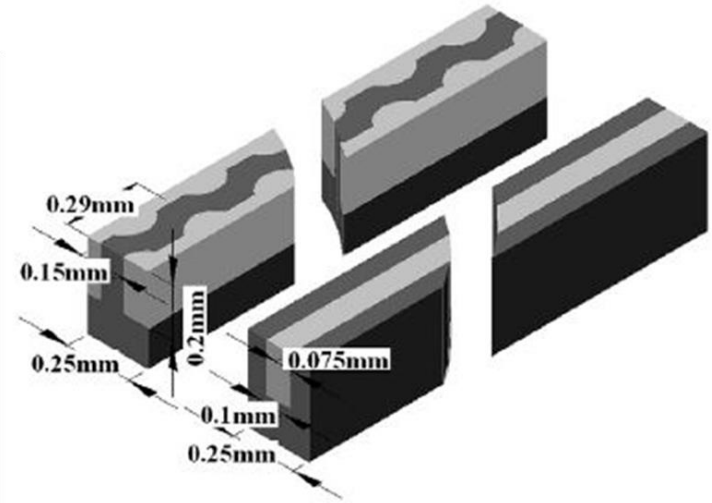

Figure 2.9 The microchannel with offset fan-shaped reentrant cavities [48].

Fluid flow and heat transfer analysis in micro-channel heat sinks with different inlet/outlet locations (I, C and Z-type), header shapes (triangular, trapezoidal and rectangular) and micro-channel cross-section shapes (the conventional rectangular micro-channel, the micro-channel with offset fan-shaped reentrant cavities and the micro-channel with triangular reentrant cavities) are numerically studied by Xia et al. [49]. The authors reported that I-type and rectangular shaped header provided better flow uniformity, and

also the micro-channel heat sink with triangular re-entrant cavities performed slightly better than the micro-channel heat sink with offset fan-shaped re-entrant cavities.

Xia et al. [29] numerically investigated heat transfer in micro-channel heat sink with fan-shaped re-entrant cavities and internal ribs with different rib height for Reynolds number ranging from 150 to 600. Their results indicated an enhancement of Nusselt number up to 167% with friction factor 1.2 to 6.5 higher than the conventional rectangular channel.

2.2.4 Nanofluids

Higher heat transfer coefficient can be achieved by enhancing the thermal conductivity of the coolant. Thermal conductivity of the coolant can be increased by using some high thermal conductive metal particle, i.e., nanoparticle in the coolant. Based on this concept, in 1995, the term ‘nanofluids’ has been introduced by dispersing solid nanoparticles into base coolant [50].

The first numerical investigation on the heat transfer performance of a micro-channel heat sink with nanofluids was done by Seok and Choi [51] in 2006. The authors considered two nanofluid such as 1 vol.% 6 nm Cu-in-water and 2 nm diamond-in-water and developed a new model to quantify the effective thermal conductivity. The governing equations with the newly defined thermophysical properties of nanofluids were solved by control-volume-based finite difference method. The numerical results showed that the cooling performance of micro-channel heat sink with diamond and copper nanofluids were enhanced by about 10% and 4% respectively compared to the water-cooled micro-channel heat sink for a fixed pumping power.

Chein et al. [52] conducted theoretical and experimental analysis on micro-channel heat sink using nanofluid as a coolant. They fabricated a silicon micro-channel heat sink and used 0.2 to 0.4 vol.% CuO–H_2O mixtures as the coolant without a dispersion agent. The authors claimed that the nanofluid was found to absorb more heat, especially at the low flow rate; however, at high flow rates, nanoparticles contributions to extra heat absorption were very minimal. The experimental results also showed a slight increment in pressure drop due to the nanoparticles in micro-channel heat sink.

Afterward, several research groups have been experimentally and numerically studied the thermal-hydraulic performances of nanofluid cooled micro/mini-channel heat sinks. For example, Ho et al. [26] used 1 and 2 vol.% of Al_2O_3/water nanofluid to investigate forced convective heat transfer in copper micro-channel heat sink at Reynolds number ranging from 226 to 1676. For 1 vol.% of nanoparticle, the experimental results showed 70% enhancement of average heat transfer coefficient and 25% reduction of thermal resistance at the largest flow rate compared to the water-cooled micro-channel heat sink. Interestingly, the authors claimed negligible enhancement of friction factor for nanofluid-cooled heat sink despite of increased dynamic viscosity of nanofluid compared to the water.

Experimental and numerical investigation of the thermal and hydraulic performance of Al_2O_3 nanofluid-cooled mini-channel heat sinks was performed by Saeed et al. [53]. They considered two different nanofluid concentration, such as 0.01 and 0.025 vol.%, three different fin spacings (0.5 to 1.50 mm) and five different flow rates (0.50 to 1.50 LPM). The experimental results showed an enhancement of 24.9%, 27.6%, and 31.1% of the convective heat transfer coefficient of the heat sink with fin spacing of 1.5

mm, 1.0 mm, and 0.5mm, respectively. The authors also claimed that higher heat transfer enhancement could be achieved by dreading the fin spacing (hydraulic diameter) of the flow channel at the same value of volume concentration and coolant flow rate. For example, enhancement factor at 1.5 vol.% of nanoparticles and 1.5 LPM flow rate were observed as 1.28, 1.29, and 1.33 for fin spacing value of 1.5,1.0 and 0.5 respectively.

Although a higher heat transfer coefficient can be achieved by utilizing nanofluids, however, suspension of micrometer or millimeter-sized nanoparticles has led to severe problems such as channel clogging and poor suspension stability. These disadvantages bring into question the over-all merit of using nanofluids in practical applications.

2.2.5 Secondary Flow

The concept of secondary flow was first introduced by Xu et al. [31]. The authors demonstrated a new silicon microchannel heat sink equipped with transverse micro-channel, as shown in Figure 2.10. The heat sink composing of parallel longitudinal triangular shaped micro-channels and several trapezoidal transverse microchannels, which separate the whole flow length into several independent zones, in which the thermal boundary layer is in developing. The redeveloping flow was repeated for all the independent zones, and thus a 26.4% higher overall heat transfer was achieved. Meanwhile, the pressure drops were decreased by 27% compared to the conventional micro-channel heat sink. The authors identified the reduced “effective flow length” as the possible reason for the reduced pressure drop requirements.

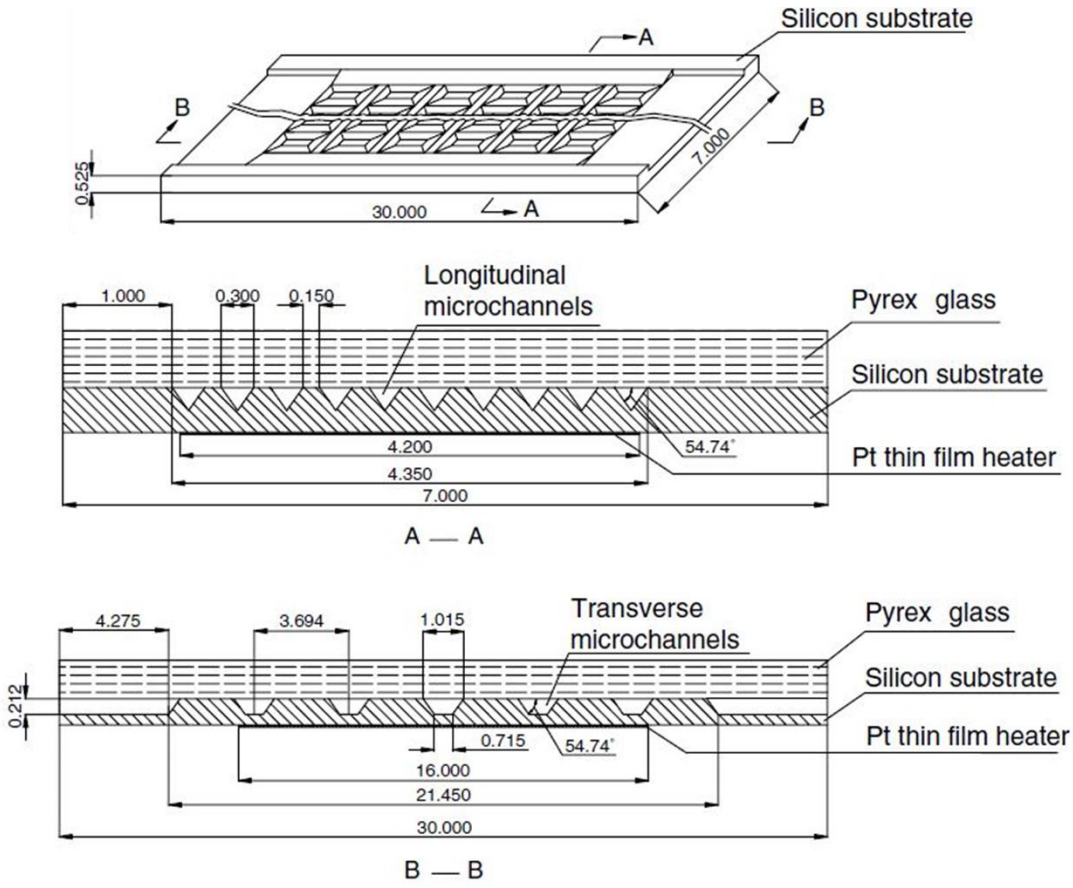

Figure 2.10 Micro-channel heat sink with transverse micro-channel (all dimensions are in mm) [31]

In 2010, Lee et al. [54] presented the concept of oblique fin a shown in Figure 2.11 in contrast to the continuous fin to enable significantly higher transverse flow in-between two parallel streams. The authors argued that the breakage of the continuous fin into oblique sections would break up and re-initialize the thermal boundary layer at the leading edge of each oblique fin and eventually will reduce the boundary-layer thickness. This regeneration of the entrance effect will cause the flow to be always in a developing state, thus resulting in better heat transfer. In order to prove their arguments, the authors performed a comparative experimental heat transfer and pressure drop study for an oblique

finned copper micro-channel heat sink and a conventional straight finned micro-channel heat sink by employing water as the working fluid. Their experimental data showed that oblique finned heat sink enhanced the heat transfer performances as much as 80% and reduced the thermal resistance as much as 18% compared to the conventional channel. Interestingly, there was a negligible pressure drop penalty associated with the novel oblique finned micro-channel heat sink in contrast to conventional enhancement techniques.

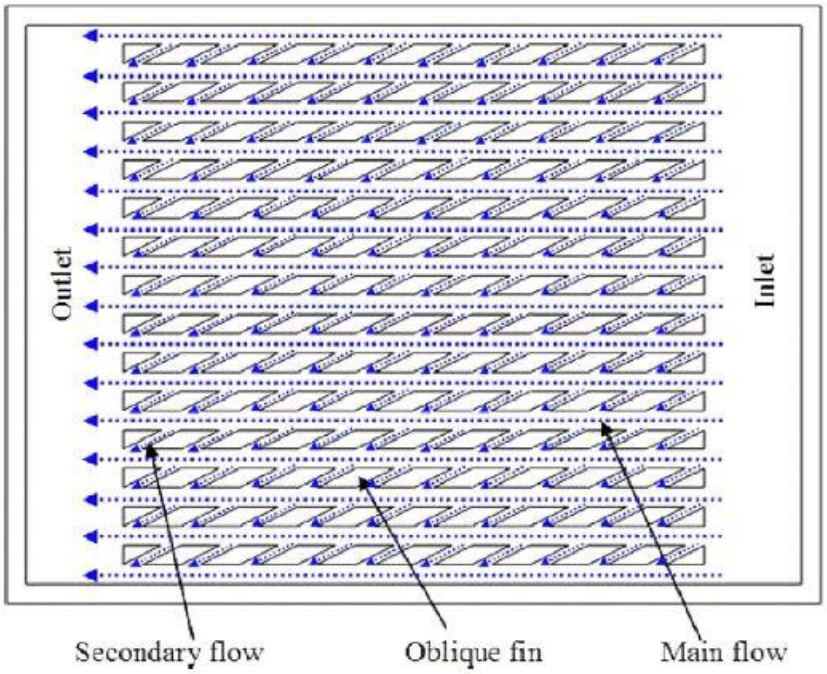

Figure 2.11 Oblique finned micro-channel heat sink.

Afterward, the same group has been performed numerous experimental and numerical studies [55-56] to examine the effect of the oblique fin on the thermal-hydraulic performance of micro-channel heat sink. They reported superior overall performance over the conventional micro-channel heat sinks because of the re-initialization of the thermal boundary layer at the leading edge of each oblique fin.

The same group also experimentally and numerically [57-58] studied the effect of secondary flow on the thermal-hydraulic performance of the cylindrical mini-channel heat sinks by employing oblique fin as shown in Figure 2.12 and claimed similar overall performance improvement as the planner oblique finned mini-channel heat sinks over the conventional heat sink.

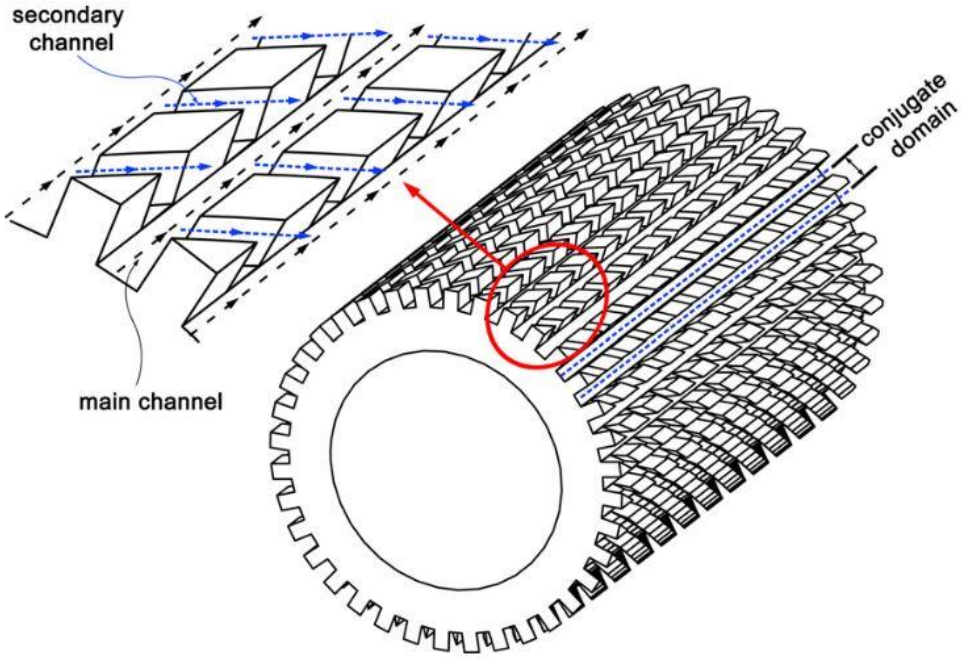

Figure 2.12 Cylindrical oblique finned mini-channel heat sink [57].

Kuppusamy et al. [59] enabled secondary flow by utilizing slanted passage in the channel wall between the adjacent channels in alternating orientation, as shown in Figure 2.13. The authors numerically studied the effects of the slanted passage distance, number and also inclination angle on the overall thermal-hydraulic performance of the micro-channel heat sink. Interestingly, the results showed that the overall performance of the micro-channel heat sink with alternating slanted passage increased by 146% together

with ~6% reduction in pressure drop due to the combined effect of flow mixing and thermal boundary layer re-development.

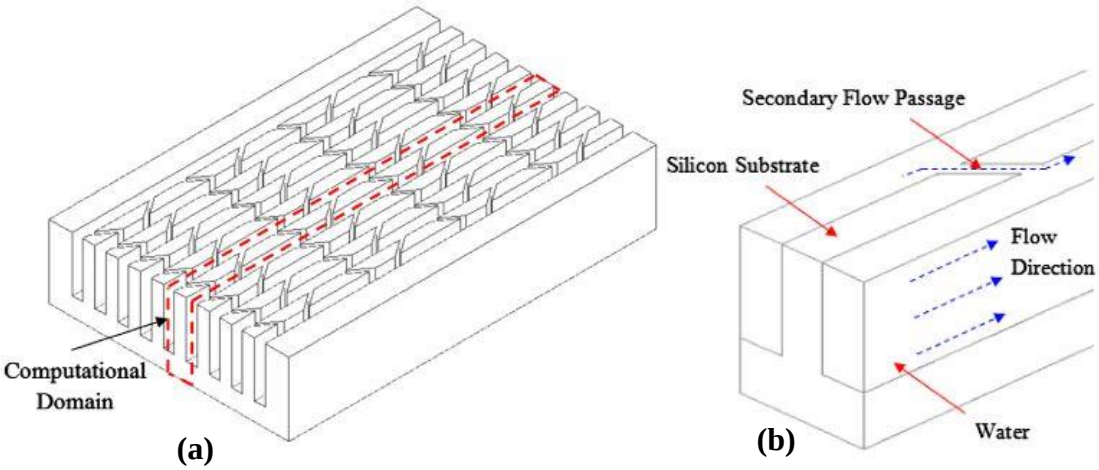

Figure 2.13 (a) schematic diagram of the computational domain, (b) coolant flow directions [59].

The fluid flow and heat transfer behaviors of a novel sinusoidal micro-channels with secondary branches were examined both numerically and experimentally by Chiam et al. [60]. To enable cross-channel mixing, the authors fabricated secondary branches in an alternating fashion at an angle of ±45^{o} to the peaks and the troughs of the wavy micro-channel configuration. The authors concluded that at low Re ($Re < 100$), the benefits of secondary branches were more pronounced while at high Re ($Re > 100$), the enhancement in heat transfer performance could not match the corresponding pressure drop penalty incurred. The results also showed that the small sinusoidal wave amplitude to wave length ratio along with secondary branches provided better thermal performance without a pressure drop tradeoff.

The effects of secondary flow induced by two differently shaped surface roughnesses (rectangular and triangular) and inter-connectors between two parallel flow mini-channels were numerically studied by Hossain et al. [61] in the laminar flow regime. In case of inter-connected mini-channel heat sink without roughness, the results illustrated negligible secondary flow and comparable thermal performance compared to the conventional mini-channel heat sink. However, the authors reported significant secondary flow in case of roughened inter-connected mini-channel heat sink.

Japar et al. [62] numerically studied the combined effect of rectangular rib, secondary channel, and triangular cavity on the overall performance of the micro-channel heat sink for Reynolds number (Re) ranging from 100 to 450. They claimed extraordinary thermal performance could be achieved by employing rectangular rib and triangular cavity along with the secondary channels due to the shared effect of flow interruption, redevelopment of the thermal boundary layer, drastic flow disturbance, chaotic advection, and flow mixing between adjacent channel. Surprisingly, the results showed a significant reduction in pressure drop requirement for the modified heat sink with rectangular rib, secondary channel, and triangular cavity.

The effects of geometrical parameters of transverse micro-channels such as height and density (number) of the transverse micro-channels, on the pressure drop, temperature distribution and heat transfer rate inside the micro-channel heat sink were investigated numerically by Soleimanikutanaei et al. [63] for a wide Re number range. Figure 2.14 shows the computational domain along with the transverse micro-channel. The numerical results showed that both pressure drop, and Nusselt number increase with the decrease of the height and increase of the number of transverse microchannels due to the entrance effect

introduced to the heatsink by adding the transverse microchannels. Additionally, more pronounced heat transfer enhancement was reported by the authors for narrower transverse micro-channels.

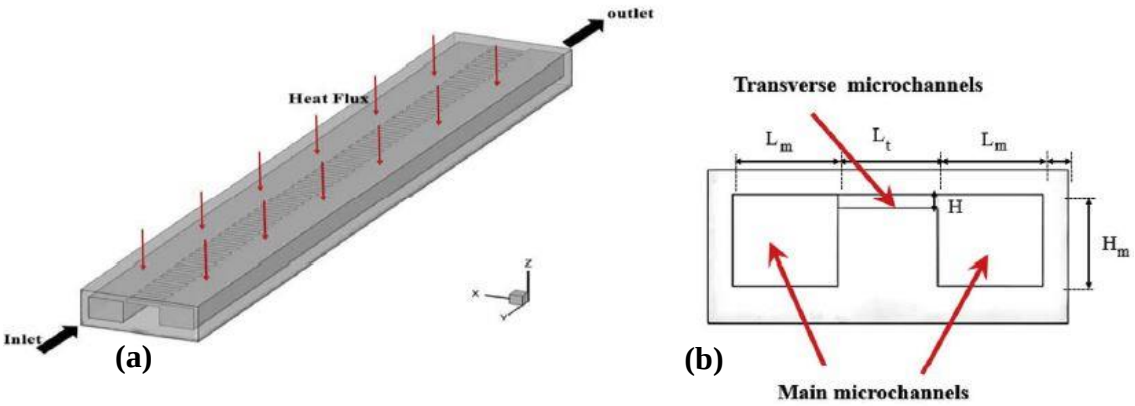

Figure 2.14 (a) Isometric and (b) cross-sectional view of the micro-channel heat sink with transverse micro-channel [63].

2.3 Summary

In the brief literature of passive heat transfer enhancement techniques, it was observed that improved heat transfer performance of micro-channel heat sink can be achieved by employing surface roughness, geometric modification, and reentrant cavities with a cost of high pumping power. Moreover, coolant thermo-physical properties enhancement using nanoparticles suffer from poor suspension stability. On the contrary, thermal boundary layer disruption and re-initialization via transverse flow is the most viable passive heat transfer augmentation technique with marginal pumping power penalty. For micro/mini-channel heat sinks equipped with secondary channels to enable secondary flow, to date, most studies are focused on parallel flow heat sinks. Same coolant flow direction through neighboring channels gives negligible pressure difference across the

secondary channel and eventually reduces the secondary flow. To overcome this limitation, in the present thesis, the concept of counter flow mini-channel heat sink along with secondary channel has been introduced.

CHAPTER 3 THEORETICAL BACKGROUND

3.1 Introduction

In the present research, the effect of secondary flow on the thermal-hydraulic performance of the water-cooled inter-connected parallel and counter flow mini-channel heat sinks was quantified numerically and experimentally. Secondary flow improves the overall performance of the mini-channel heat sinks by breaking and re-initializing the thermal and hydraulic boundary layers. In this thesis, the secondary flow was generated by employing two inter-connectors in-between two parallel mini-channels. Since incompressible fluid flow (like water) is triggered by pressure difference, therefore, to comprehend the secondary flow mechanism clearly, it is essential to understand the pressure distribution of the parallel and counter flow mini-channel heat sinks. Hence, In the present chapter, the detailed pressure distribution and the corresponding fluid flow behaviors for the both conventional and inter-connected parallel and counter flow mini-channel heat sinks are discussed.

3.2 Parallel Flow Mini-Channel Heat Sink

In parallel flow mini-channel heat sinks, coolant flow through some parallel channels in the same directions. Figure 3.1 (a) shows the top view of the two parallel flow mini-channels separated by a solid wall where coolant is flowing from left to right directions through the both channels. During coolant flow through any conventional channel, pressure magnitude reduces linearly (approximately) from the inlet to the outlet

of the channel. Figure 3.1 (b) depicts the corresponding pressure distribution for both channels, along with the flow directions. Since coolant is flowing in the same directions through both channels 1 and 2, therefore pressure magnitudes are linearly reducing for both channels. Also, from Figure 3.1 (b), it can be seen that, for both channels, pressure profile overlaps on each other because of the same coolant flow rate through the both channels.

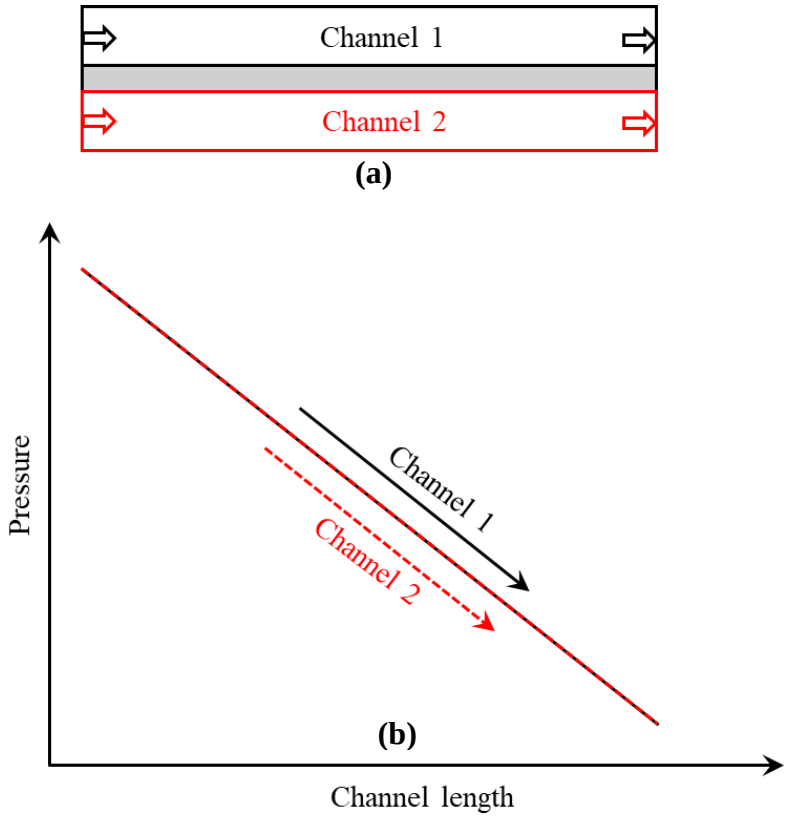

Figure 3.1 (a) Top view of parallel channels along with flow direction, (b) local pressure distribution along channel length (figure is not drawn to scale).

Figure 3.2 (a) depicts the top view of inter-connected parallel flow mini-channel heat sink, and Figure 3.2 (b) shows the corresponding local pressure distribution of both channels. It is worth mentioning that same pressure magnitude across the inter-connectors results in same amount of the secondary flow from both channels in opposite directions.

These two opposite secondary flow streams eventually engender a stationary recirculation zone inside the inter-connectors. Therefore, in case of parallel flow, secondary flow can not be generated by implementing straight inter-connectors and hence, inter-connected parallel flow mini-channel heat sinks provide very similar pressure profile compared to the conventional channel as shown in Figure 3.2 (b).

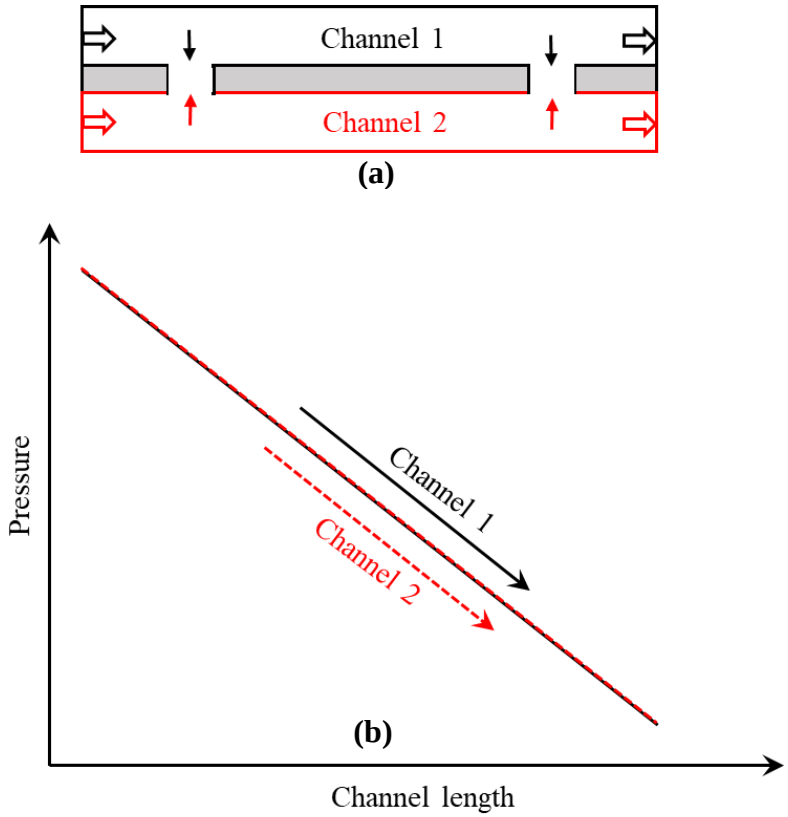

Figure 3.2 (a) Top view of inter-connected parallel flow channels along with flow directions, (b) local pressure distribution along the channel length (figure is not drawn to scale).

3.3 Counter Flow Mini-Channel Heat Sinks

In counter flow mini-channel heat sink, coolant flow in the opposite direction through two adjacent channels. Figure 3.3 (a) shows the top view of the two counter flow mini-channels separated by a solid wall where through channel 1, coolant is flowing from

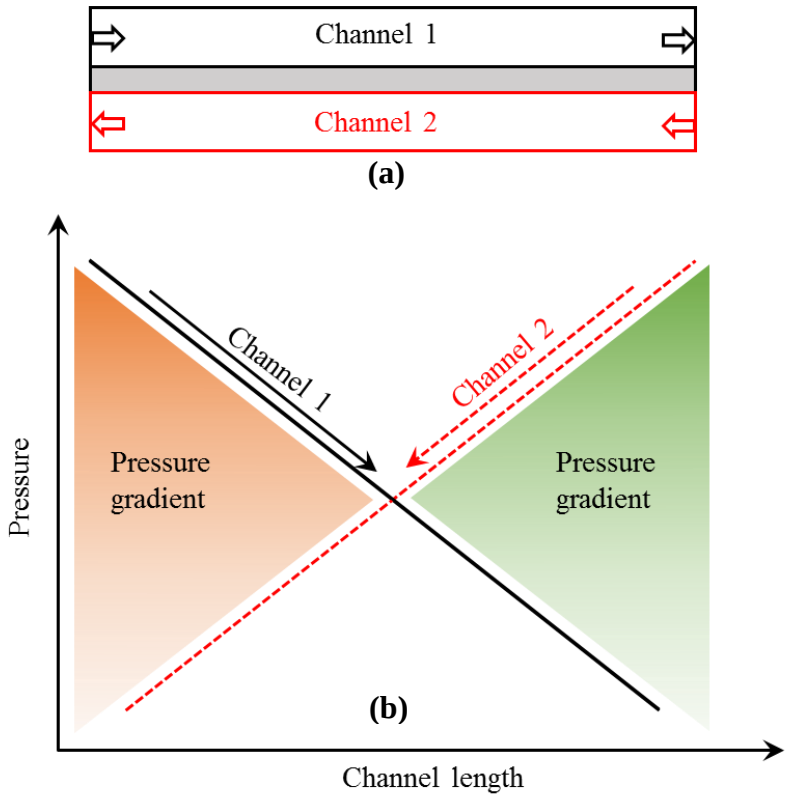

Figure 3.3 (a) Top view of counter flow channels along with flow directions, (b) local pressure distribution along the channel length (figure is not drawn to scale).

left to right and coolant is flowing from right to left direction through channel 2. Therefore, for channel 1, pressure magnitude reduces linearly from left to right (inlet to outlet) as shown in Figure 3.3 (b). On the contrary, for channel 2, pressure magnitude reduces linearly from right to left. Apart from that, two opposite pressure profile intersects at the middle point of the heat sinks. These two opposite pressure distributions in the adjacent channels provide significant local pressure gradient between two channels except the intersecting point. Positive pressure gradient is evident from channel 1 to channel 2 in the left side of the middle intersecting point whereas, negative pressure gradient is evident in the right side as shown in Figure 3.3 (b). Therefore, by utilizing this pressure difference in-

between two adjacent counter flow channels, secondary flow can be generated by incorporating inter-connectors.

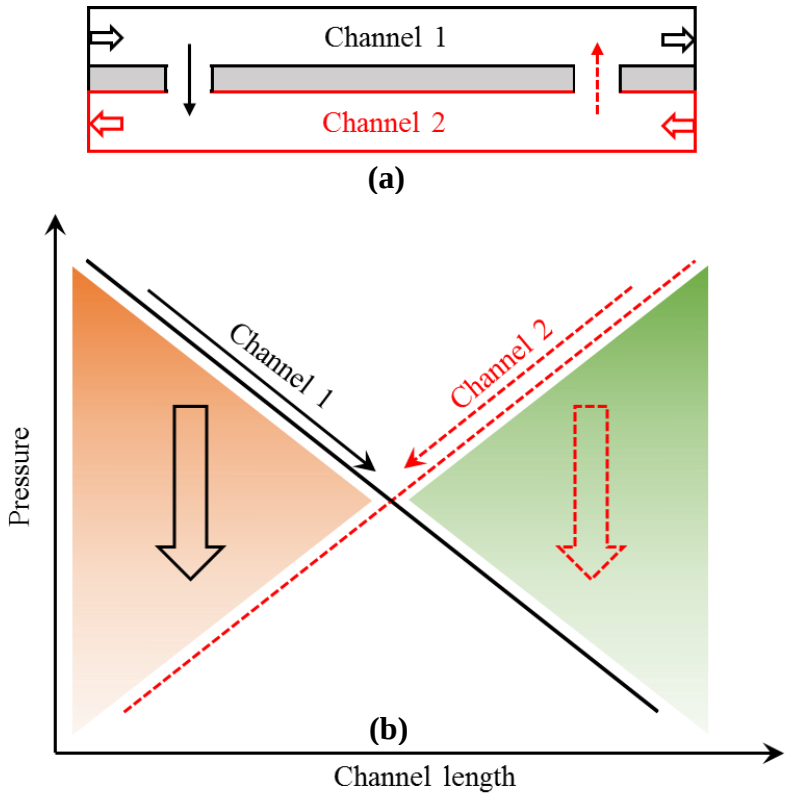

Figure 3.4 (a) Top view of inter-connected counter flow channels along with flow direction, (b) local pressure distribution along the channel length and secondary flow directions (figure is not drawn to scale).

In order to create secondary flow, two inter-connectors were employed in the middle solid wall. It is worth mentioning that positive pressure gradient from channel 1 to 2 across the left inter-connector results in some secondary flow from channel 1 to 2 as shown in Figure 3.4 (a) and (b). Similarly, positive pressure gradient from channel 2 to 1 across the right inter-connector results in some secondary flow from channel 2 to 1. This secondary flow breakup the thermal and hydraulic boundary layers and eventually enhance the overall performance of the mini-channel heat sinks compared to the conventional mini-channel heat sinks.

CHAPTER 4 EFFECT OF SECONDARY CHANNELS WIDTH ON OVERALL PERFORMANCE OF PARALLEL AND COUNTER FLOW MINI-CHANNEL HEAT SINKS

4.1 Introduction

The thermal-hydraulic performance of an inter-connected parallel and counter flow mini-channel heat sinks depend on thermal and hydraulic boundary layers disruption, which depends on the amount of secondary flow through the inter-connectors. Moreover, the amount of secondary flow depends on the width of the inter-connectors. Therefore, in the present chapter, the effect of inter-connectors width for a specified inter-connectors location on the overall performance of the parallel and counter flow mini-channel heat sinks have been investigated numerically. A 3D numerical model has been developed using ANSYS FLUENT, and the optimum inter-connector width has been identified based on non-dimensional pressure, velocity, temperature, friction factor, overall Nusselt number (Nu), thermal resistance, and performance evaluation criteria (PEC).

4.2 Computational Domain

Figure 4.1 shows the schematic of the computational domain of conventional mini-channel heat sink along with the coordinate system and key notations. For conventional parallel and counter flow mini-channel heat sink, two mini channel configuration was generated as shown in Figure 4.1. In parallel flow mini-channel heat sink, coolant flows in the same direction through the adjacent channels, and in counter flow heat sink, coolant flows in the opposite direction. Total area of the heat sink base is $W_t \times L$. The individual

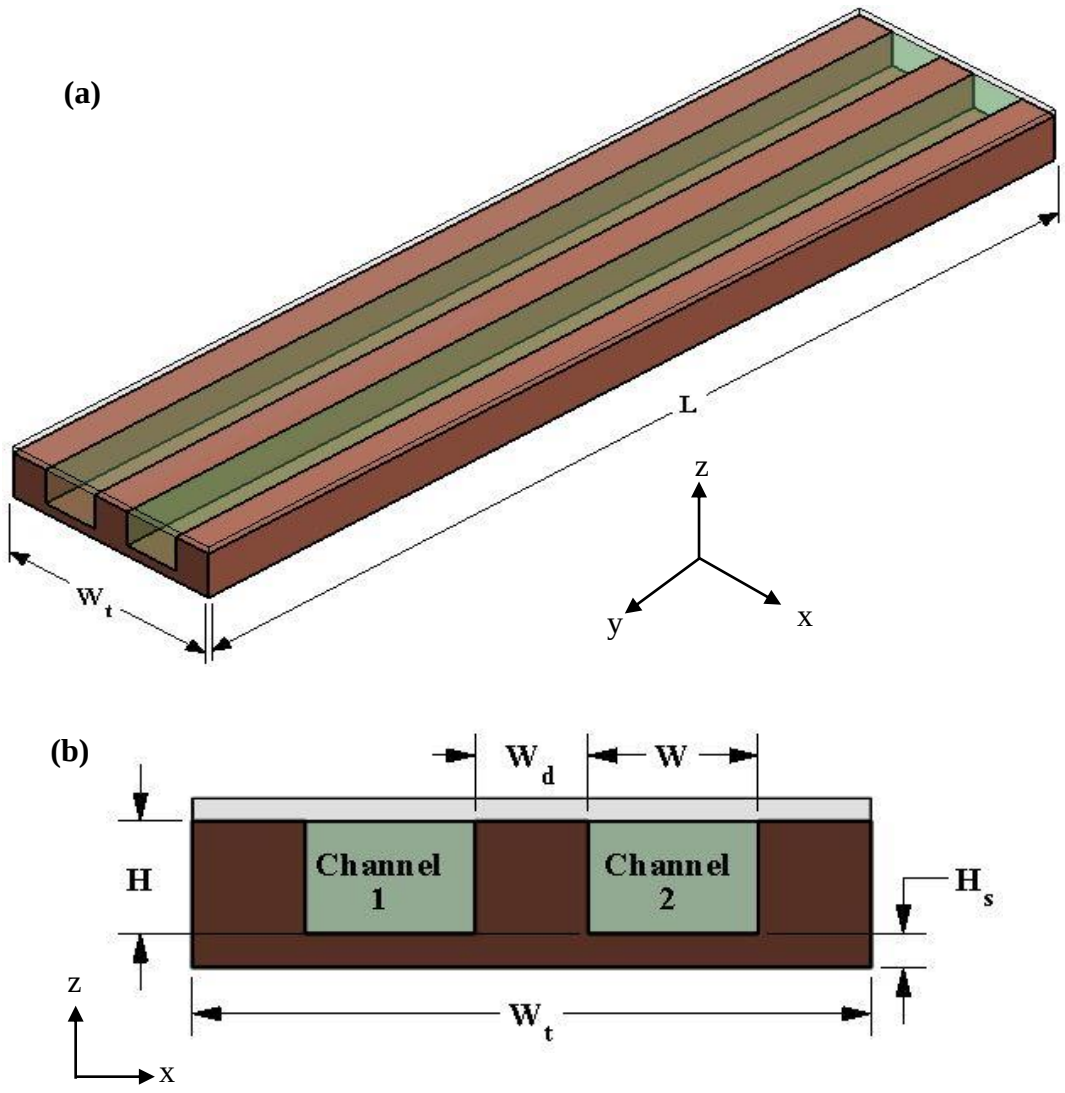

Figure 4.1 Schematic of the conventional mini-channel heat sink (a) isometric view (b) front view.

channel height, width, and length are H=0.50 mm, W=1.5 mm, and L=26 mm respectively. Two channels are separated by a solid copper wall with a constant thickness, W_d=2W/3. The thickness of each side wall is same as that of W_d. The height of the bottom substrate is H_s=H/3. Figure 4.2 illustrates the computational domain of the inter-connected mini-channel heat sink. Two inter-connectors are located at same distance from the inlet and outlet of the heat sink and have the same depth of the mini-channel. L_i is defined as the

distance between the center point of the inter-connectors and the inlet/outlet of the heat sink, W_i is defined as the width of the inter-connector, and i is defined as the case number as shown in Figure 4.2. Detailed dimensions of the inter-connectors are listed in Table 4.1. The conventional parallel and counter flow heat sink is denoted as Case 0. Copper was selected as the heat sink material because of its high thermal conductivity and water was chosen as the coolant for their superior heat transfer capability. Uniform heat flux is being applied from the bottom surface of the copper substrate.

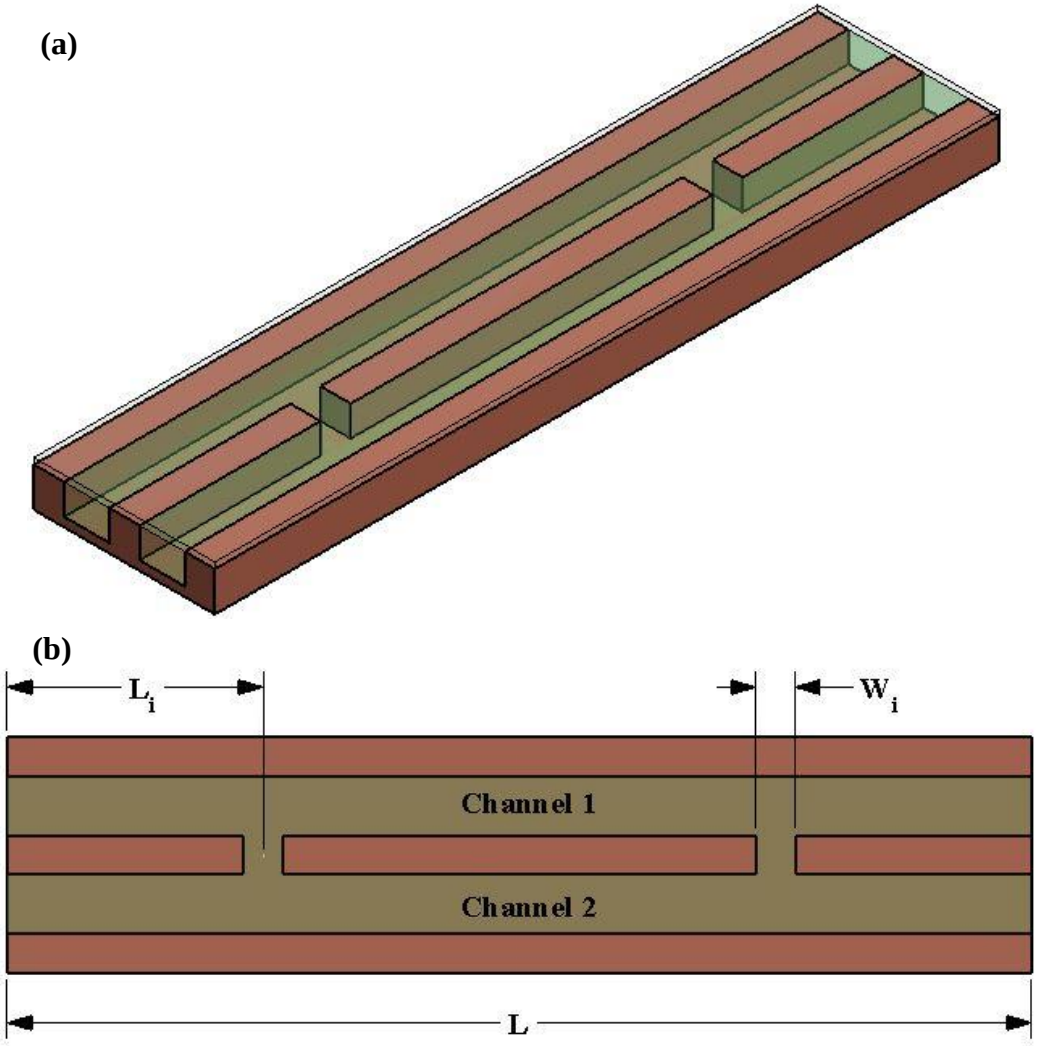

Figure 4.2 Schematic of the inter-connected mini-channel heat sink (a) isometric view (b) front view.

Table 4.1 Case specific inter-connector dimensions

Case number, i	L_i (mm)	L_i/L	W_i (mm)	W_i/W
0 (base case)			-	-
1			0.5	1/3
2	6.5	¼	0.75	1/2
3			1	2/3
4			1.25	5/6
5			1.5	1

4.3 Governing Equations

To study the thermal-hydraulic characteristics of the MCHS, a numerical model is developed under the following assumptions:

(a) since in present study Knudsen number (Kn) is less than 10^{-3} [64], hence continum assumptions are applicable for the fluid flow. Therfore, Navier-stokes equation and no-slip boundary conditions are employed.

(b) steady-state heat transfer and fluid flow.

(c) incompressible and laminar flow.

(d) constant thermo-physical properties for the working fluid and solid as shown in Table 4.2.

(e) radiation heat transfer is negligible.

(f) effect of viscous dissipation and gravity are negligible.

Table 4.2 Thermo-physical properties of the solid and fluid domain

Properties	Density, ρ (kg/m^3)	Sp. Heat, C_p (j/kg-K)	Thermal conductivity, k (W/m-K)	Viscosity, μ (kg/m-s)
Water	998.2	4182	0.6	0.001003
Copper	8978	381	387.6	-

According to the above assumptions, the conservation equation of mass, momentum, and energy can be written in the following form:

Continuity equation:

$$\frac{\partial u}{\partial x}+\frac{\partial v}{\partial y}+\frac{\partial w}{\partial z}=0 \tag{4.1}$$

Momentum equation:

$$u\frac{\partial u}{\partial x}+v\frac{\partial u}{\partial y}+w\frac{\partial u}{\partial z}=-\frac{1}{\rho_f}\frac{\partial P}{\partial x}+\frac{\mu_f}{\rho_f}\left[\frac{\partial^2 u}{\partial x^2}+\frac{\partial^2 u}{\partial y^2}+\frac{\partial^2 u}{\partial z^2}\right] \tag{4.2}$$

$$u\frac{\partial v}{\partial x}+v\frac{\partial v}{\partial y}+w\frac{\partial v}{\partial z}=-\frac{1}{\rho_f}\frac{\partial P}{\partial y}+\frac{\mu_f}{\rho_f}\left[\frac{\partial^2 v}{\partial x^2}+\frac{\partial^2 v}{\partial y^2}+\frac{\partial^2 v}{\partial z^2}\right] \tag{4.3}$$

$$u\frac{\partial w}{\partial x}+v\frac{\partial w}{\partial y}+w\frac{\partial w}{\partial z}=-\frac{1}{\rho_f}\frac{\partial P}{\partial z}+\frac{\mu_f}{\rho_f}\left[\frac{\partial^2 w}{\partial x^2}+\frac{\partial^2 w}{\partial y^2}+\frac{\partial^2 w}{\partial z^2}\right] \tag{4.4}$$

Energy equation :

$$u\frac{\partial T_f}{\partial x}+v\frac{\partial T_f}{\partial y}+w\frac{\partial T_f}{\partial z}=\frac{k_f}{\rho_f C_{p,f}}\left[\frac{\partial^2 T_f}{\partial x^2}+\frac{\partial^2 T_f}{\partial y^2}+\frac{\partial^2 T_f}{\partial z^2}\right] \tag{4.5}$$

where, $u, v\ and\ w$ are the velocity components along $x, y\ and\ z$ direction respectively (for 3D) as shown in Figure 4.1, T_f is the coolant temperature,

$\rho_{f,}\ k_{f,}\ \mu_{f,}\ and\ C_{p,f}$ are the coolant density, thermal conductivity, viscosity and specific heat.

Energy equation for the solid region:

$$k_{so}\left[\frac{\partial^2 T_s}{\partial x^2}+\frac{\partial^2 T_s}{\partial y^2}+\frac{\partial^2 T_s}{\partial z^2}\right]=0 \tag{4.6}$$

where, k_{so} is the thermal conductivity and T_s is the temperature of the solid substrate.

4.4 Boundary Conditions

The hydrodynamic boundary conditions are as follows: At the inlet of the mini-channel, fluid velocity is assumed uniform.

$$u=0, v=v_f=v_{in}, and\ w=0 \tag{4.7}$$

At the outlet, a pressure outlet boundary condition is applied.

$$P_{out}=P_f \tag{4.8}$$

On the inner wall of the mini-channel heat sink, no-slip boundary conditions are applied: $u_\Gamma=v_\Gamma=w_\Gamma=0$. (4.9)

The thermal boundary conditions are given as follows:

At the inlet of the heat sink, coolant temperature is set at a constant value,

$$y=0: T_{in}=T_f \tag{4.10}$$

On the bottom surface of the computational domain, constant heat flux boundary condition is imposed.

$$z = 0: q'' = -k_{so} \frac{\partial T_s}{\partial z} \quad (4.11)$$

Adiabatic boundary condition is applied on all other sides of the computational domain.

$$z = H + H_s: Q'' = -k_{so} \frac{\partial T_s}{\partial z} = 0 \quad (4.12)$$

$$x = 0, W_t : Q'' = -k_{so} \frac{\partial T_s}{\partial x} = 0 \quad (4.13)$$

$$y = 0, L : Q'' = -k_{so} \frac{\partial T_s}{\partial y} = 0 \quad (4.14)$$

The computational parameters used in this study are listed in Table 4.3.

Table 4.3 Computational parameters

Inlet velocity, v_{in} (m.s^{-1})	Inlet temperature, T_{in} (K)	Outlet pressure, P_{out} (Pa)	Heat flux, Q'' (W.m^{-2})
0.2-1.4	293	0 (gage pressure)	200000

4.5 Data Reduction

For numerical measurement of wall temperature, coolant velocity, and pressure, area-weighted average value was used while mass-weighted average value was used for coolant temperature measurement.

Reynolds number, Re is calculated using the following equation:

$$Re = \frac{\rho_f v_m D_h}{\mu_f} \quad (4.15)$$

where, D_h is the hydraulic diameter of the mini-channel which is defined as:

$$D_h = \frac{4A_c}{P} = \frac{2WH}{W+H} \tag{4.16}$$

where, W and H are the width and height of the mini-channel, $A_c(= WH)$ is the cross-sectional area and $P\big(= 2(W + H)\big)$ is the wetted perimeter of the channel.

Effective heat flux is calculated using the following equation:

$$Q''_{eff} = \frac{Q}{A_{int}} = \frac{Q'' A_b}{A_{int}} = \frac{Q'' L W_b}{A_{int}} \tag{4.17}$$

Where, Q is the total heat transfer rate, $A_b = LW_b$ is the base surface area of the substrate, and A_{int} is the interfacial area of the solid and fluid domain.

The average heat transfer coefficient, h, and Nusselt number, Nu can be determined using the following equations:

$$h = \frac{Q''_{eff}}{(T_{int} - T_m)} \tag{4.18}$$

$$Nu = \frac{hD_h}{k_f} \tag{4.19}$$

where, $T_{int} = \frac{\int T dA}{\int dA}$ is the area-weighted average interfacial temperature, and $T_m = \frac{T_{in}+T_{out}}{2}$ is the mass-weighted average bulk fluid temperature.

The apparent friction factor, f is calculated as:

$$f = \frac{-2\Delta p D_h}{\rho_f L {v_m}^2} \tag{4.20}$$

where $\Delta p = p_{in} - p_{out}$ is the average pressure difference between inlet and outlet of the mini-channels.

The non-dimensional length, velocity components, pressure, and temperature are given as follows [65-66],

$$l = \frac{x}{L}, u_n = \frac{u}{v_{in}}, v_n = \frac{v}{v_{in}}, w_n = \frac{w}{v_{in}}, \; P = \frac{p}{\rho_f v_{in}^2}, \theta = \frac{T - T_{min}}{T_{max} - T_{min}} \tag{4.21}$$

where T_{max} the maximum temperature calculated for the parallel flow mini-channel heat sink and T_{min} the inlet temperature of the coolant.

Heat transfer mechanism from the bottom surface of the solid substrate to the flowing coolant through the mini-channel can be described in three steps: (1) heat transfer by conduction from bottom of the substrate to the interfacial wall, (2) convection heat transfer from solid fin to the coolant, and (3) capacitive heat transfer which is described by temperature increment of the coolant while flowing through the channel [67]. The corresponding thermal resistance, R_{th} can be expressed as follows,

$$R_{cond} = \frac{T_{w,b} - T_{int}}{Q} \tag{4.22}$$

$$R_{conv} = \frac{T_{int} - T_f}{Q} \tag{4.23}$$

$$R_{cap} = \frac{T_f - T_{in}}{Q} \tag{4.24}$$

where, R_{cond}, R_{conv}, R_{cap} are the conductive, convective and capacitive thermal resistance, $T_{w,b}$ is the area weighted average bottom surface $(z = 0)$ temperature of the heat sink.

The overall thermal resistance, R_{th} can be expressed as follows [67],

$$R_{th} = R_{cond} + R_{conc} + R_{cap} = \frac{T_{w,b} - T_{int}}{Q} + \frac{T_{int} - T_f}{Q} + \frac{T_f - T_{in}}{Q} = \frac{T_{w,b} - T_{in}}{Q} \tag{4.25}$$

The obtained thermal resistance at each coolant flow rates are non-dimensionalized [68] as follows:

$$R = \frac{R_{th}}{R_{th,0}} \tag{4.26}$$

where, $R_{th,0}$ is the overall thermal resistance for the conventional mini-channel heat sink.

To evaluate the pumping cost, pumping power, P_p was calculated which is defined as the product of the pressure drop across the mini-channel and the volumetric flow rate of the coolant,

$$P_p = \Delta P\dot{V} = n\Delta P v_{in} A_c \tag{4.27}$$

Where $n = 2$ is the number of mini-channel, and $\dot{V}$ is the coolant volumetric flow rate.

The combined effect of thermal resistance and pumping power can be assessed by total entropy generation rate, S which is the summation of thermal entropy generation rate and friction entropy generation rate [69] and can be expressed as follows:

$$S = S_{th} + S_{fr} = \frac{Q(T_{int} - T_{in})}{T_{int}T_{in}} + \frac{\dot{m}\Delta P}{\rho_f T_{in}} \tag{4.28}$$

Where, $\dot{m}$ is the coolant mass flow rate, S_{th} and S_{fr} are the thermal and frictional entropy generation rate respectively.

By considering the effect of heat transfer performance and friction factor of the newly proposed mini-channel heat sink, performance evaluation criteria [70-71] is defined as the ratio of the heat transfer co-efficient of the inter-connected mini-channel heat sink

to the heat transfer co-efficient of the parallel flow mini-channel heat sink without inter-connector at same pumping power and is given by,

$$\text{PEC} = \frac{Nu}{Nu_0}\Big|_{pp} = \frac{Nu/Nu_0}{(f/f_0)^{1/3}} \tag{4.29}$$

where, Nu_0 and f_0 are the overall Nusselt number and friction factor of the conventional mini-channel heat sink.

4.6 Numerical Solving Procedure and Convergence criteria

To solve four governing differential equations for pressure, velocity, and temperature fields simultaneously with appropriate boundary conditions, finite volume based commercial computational fluid dynamics software ANSYS FLUENT 16.0 was used. Semi-implicit method for pressure linked equations (SIMPLE) algorithm was used for the pressure-velocity coupling because of its stable solving capabilities [72]. The under-relaxation factors for density, pressure, momentum, energy, and body forces were set at the solver default values such as 1, 0.3, 0.7, 1, and 1 respectively. When the normalized residual values were less than 10^{-5} for all variables except temperature, the solution was considered to be converged. Only for the energy equation, the convergence criteria was set at 10^{-8}. To ensure proper convergence of the numerical model, inlet pressure, interface temperature, and volume average temperature of the fluid domain were also monitored.

4.7 Grid Generation and Grid Independence Test

Figure 4.3, Figure 4.4, and Figure 4.5 shows the structured hexahedral mapped grid of the computational domain generated by pre-processing software ICEM CFD. To avoid the difficulties of generating structured mesh for the modified micro-channel heat sink, solid substrate and fluid domain were meshed separately in ICEM CFD as shown in the

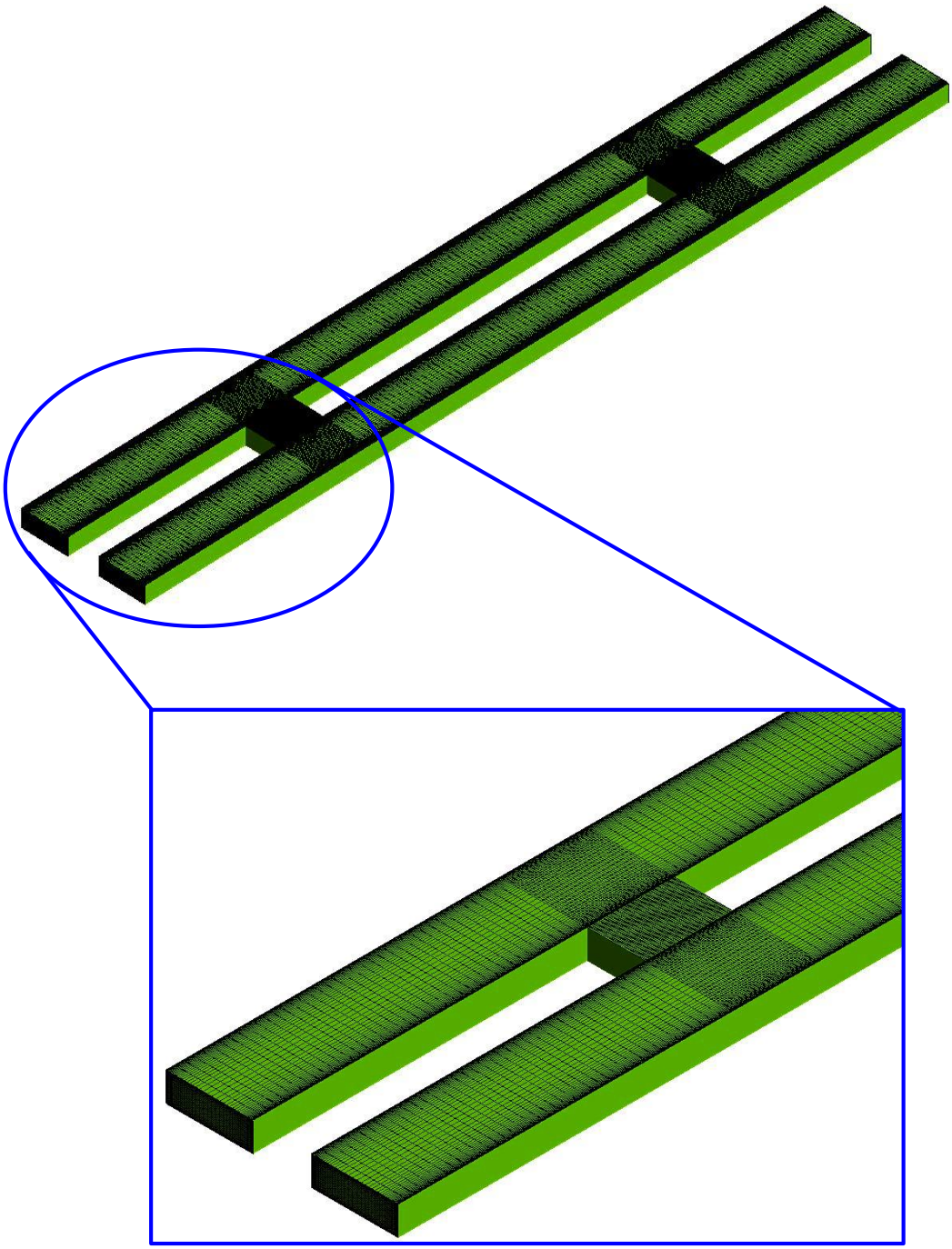

Figure 4.3 Grid generation for fluid domain.

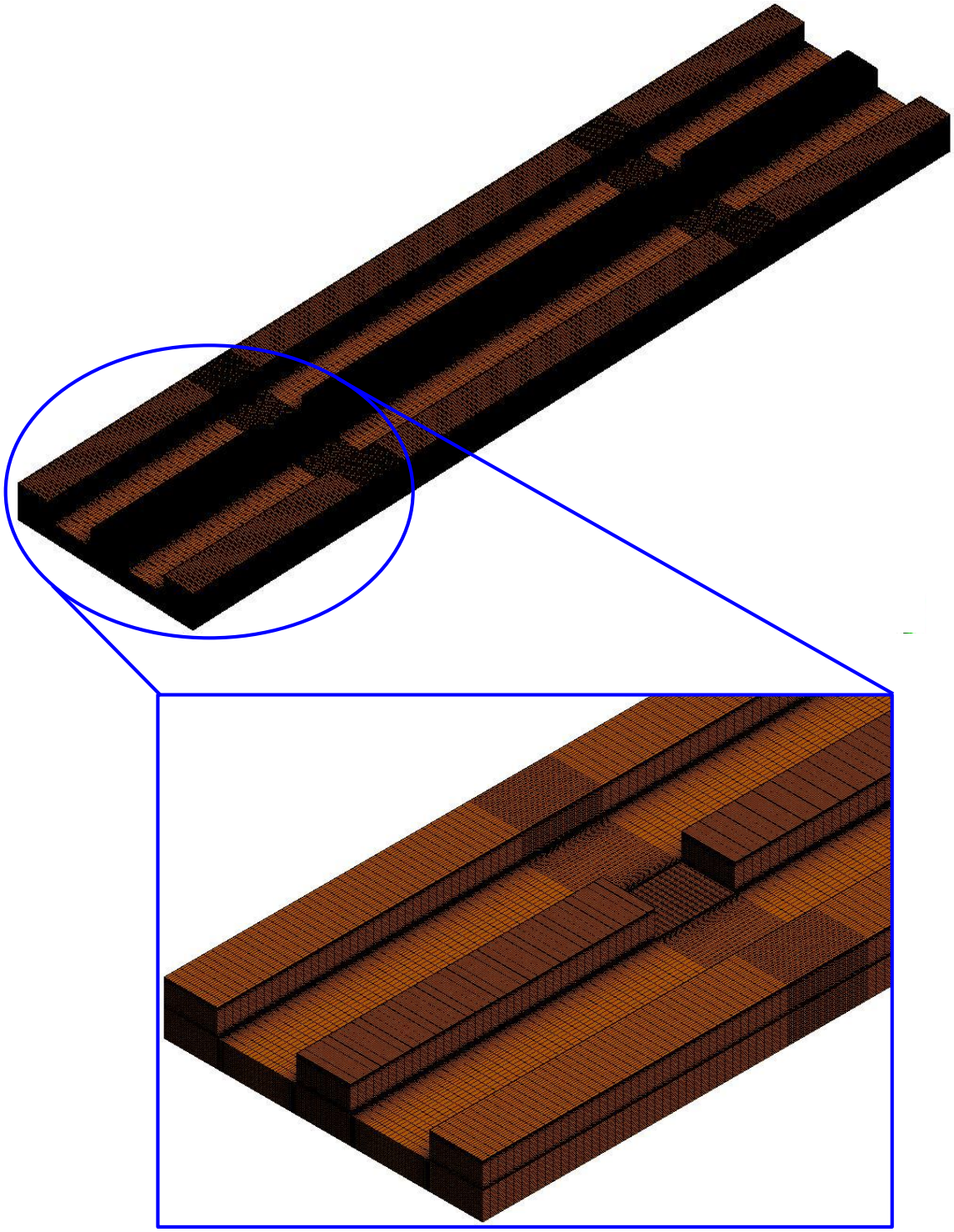

Figure 4.4 Grid generation for sold domain.

(a)

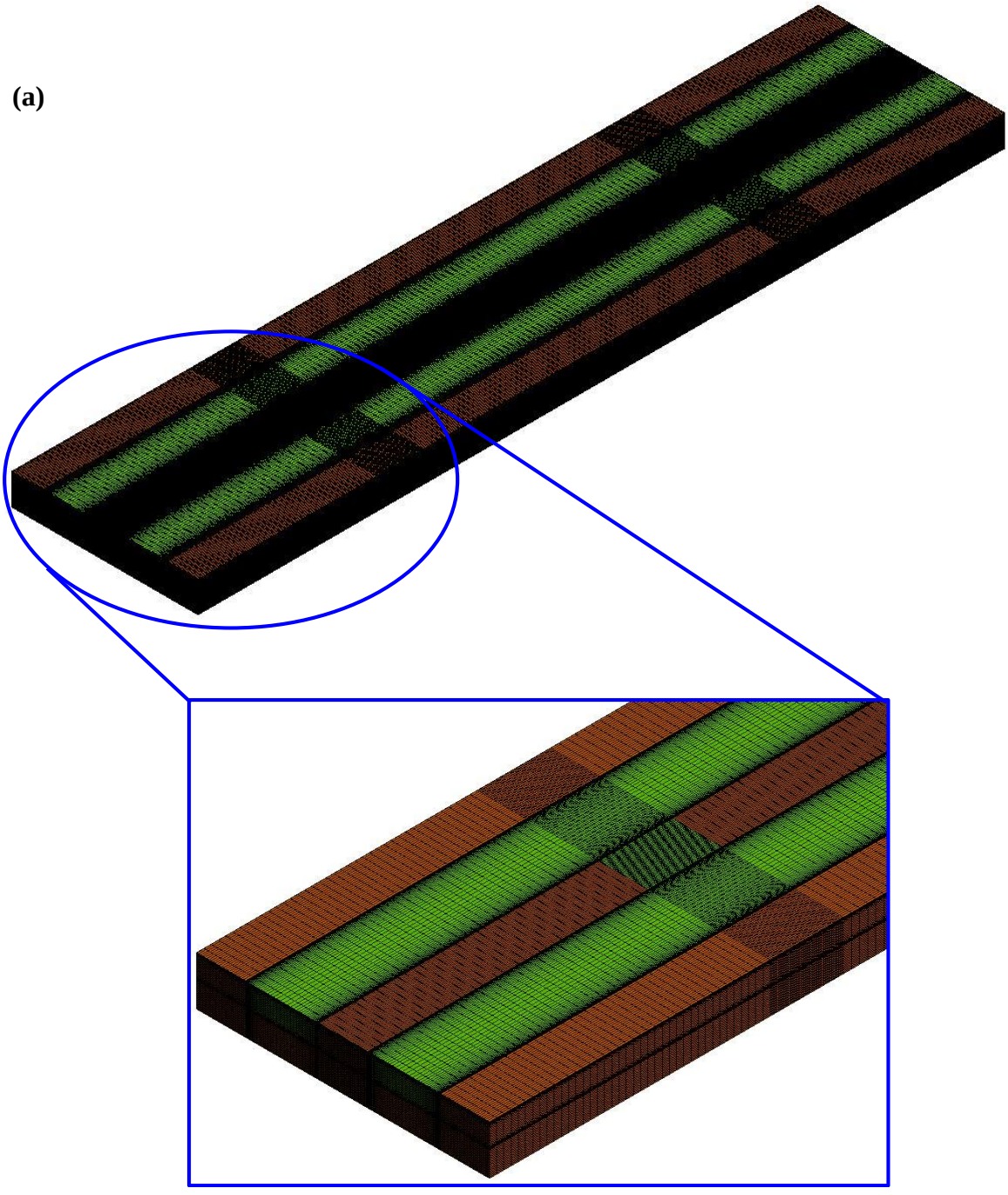

(b)

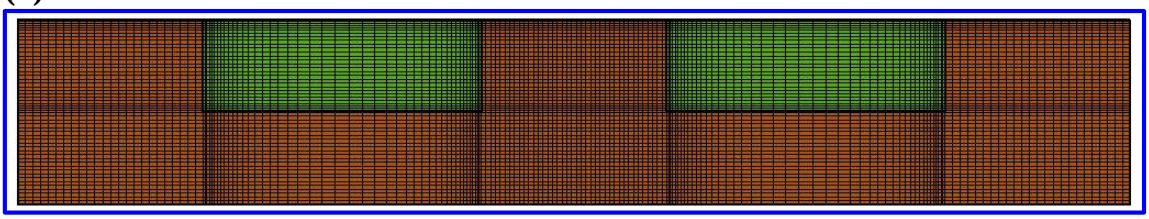

Figure 4.5 Grid generation for solid-fluid domain (a) isometric view and (b) front view.

Figure 4.3 and Figure 4.4. Afterwards those separate mesh files were combined together in ANSYS FLUENT [41] as evident in the Figure 4.5. To capture the flow behavior inside the inter- connector of the mini-channel heat sink, very fine structured mesh was generated inside the inter-connector as shown in the Figure 4.3. Grid independence test was performed for both conventional and inter-connected counter flow mini-channel heat sink at Re=746. For three different mesh number (Mesh 1-3), Table 4.4 summarizes all results of friction factor and Nusselt number for case 0 and 5 of counter flow mini-channel heat sink with Mesh 1 being the baseline. From Table 4.4, it can be seen that for both conventional and inter-connected counter flow mini-channel heat sinks, the deviation of the average friction factor and Nusselt number for Mesh 2 are less than 1%, as compared to Mesh 3. Therefore, Mesh 2 was selected for all mini-channel heat sinks.

Table 4.4 Grid independence test (Re=746)

	Mesh No.	Friction factor, f	% Deviation	Nusselt number, Nu	% Deviation
Case 0	707750	0.1233	-	10.197	-
	1866819	0.1244	0.94	10.085	1.079
	2897440	0.1245	0.125	10.094	0.10
Case 5	807500	0.1230	-	13.325	-
	2204535	0.1244	1.18	13.160	1.25
	2948400	0.1247	0.18	13.226	0.50

4.8 Results and Discussion

4.8.1 Numerical Model Validation

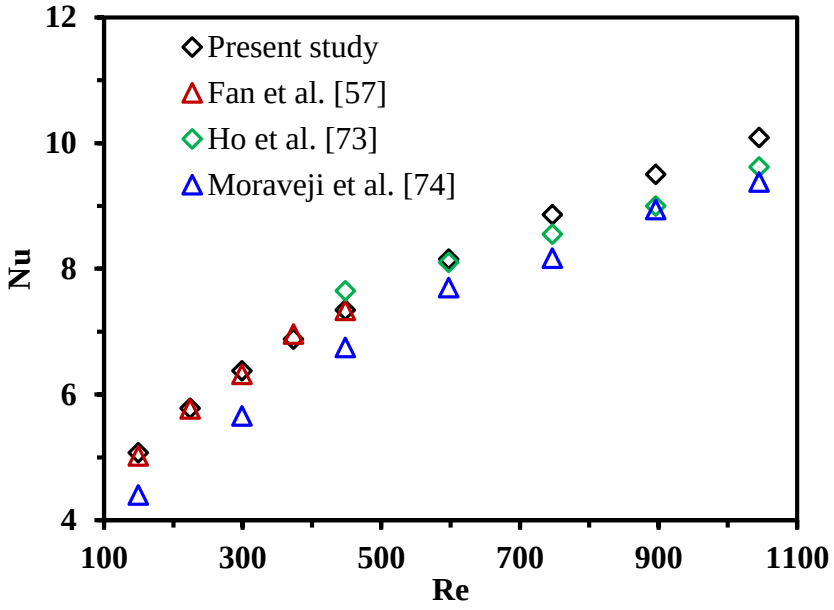

Figure 4.6 Comparison of numerical result of Nu number with the experimental results of Fan et al. [57] and Ho et al. [73] and numerical results of Moraveji et al. [74] at different Re.

To verify the accuracy and reliability of the developed CFD model, the numerically obtained Nu for parallel flow mini-channel heat sink without inter-connectors (case 0) was compared with experimental results of Fan et al. [57] for Re ranging from 150 to 450, Ho et al. [73] for Re ranging from 450 to 1044, and numerical results of Moraveji et al. [74] as shown in Figure 4.6. It was evident that the numerical results are within the uncertainty limit of both experimental results. The average deviation between Fan et al., Ho et al., and computational results are less than 0.66% and 3.74% with a maximum deviation of 1.15% and 3.74% respectively. Similarly, the average deviation between the Moraveji et al. and numerical results is less than 9.27%.

The numerically obtained overall friction factor for conventional parallel flow mini-channel heat sink (case 0) was compared with the widely used correlation of friction factor for fully developed and developing flow proposed by Shah and London [75] and presented in Figure 4.7.

$$f_{app}(L)Re_{ave,0-L} = \sqrt{\left[\frac{3.2}{(L/D_hRe)^{0.57}}\right]^2 + (fRe)_{fd}^2} \quad (4.30)$$

Where $(fRe)_{fd} = 96(1 - 1.3553 \propto +1.9467 \propto^2 - 1.7012 \propto^3 + 0.9564 \propto^4 - 0.2537 \propto^5)$ is applicable only for fully developed laminar flow.

Good agreement is noticed between the numerical and predicted friction factor with an average deviation of 7.28% as shown in the Figure 4.7.

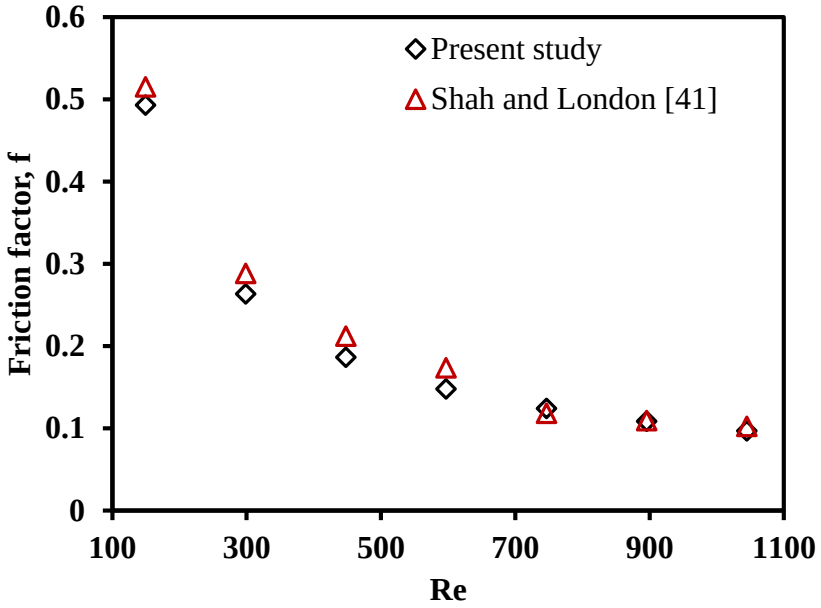

Figure 4.7 Comparison of numerical result of friction factor, f with the Shah and London [41] correlation at different Re.

In case of inter-connected counter flow heat sink, a significant amount of coolant flows transversely, especially at the higher width of the inter-connectors (Case 5) resulting

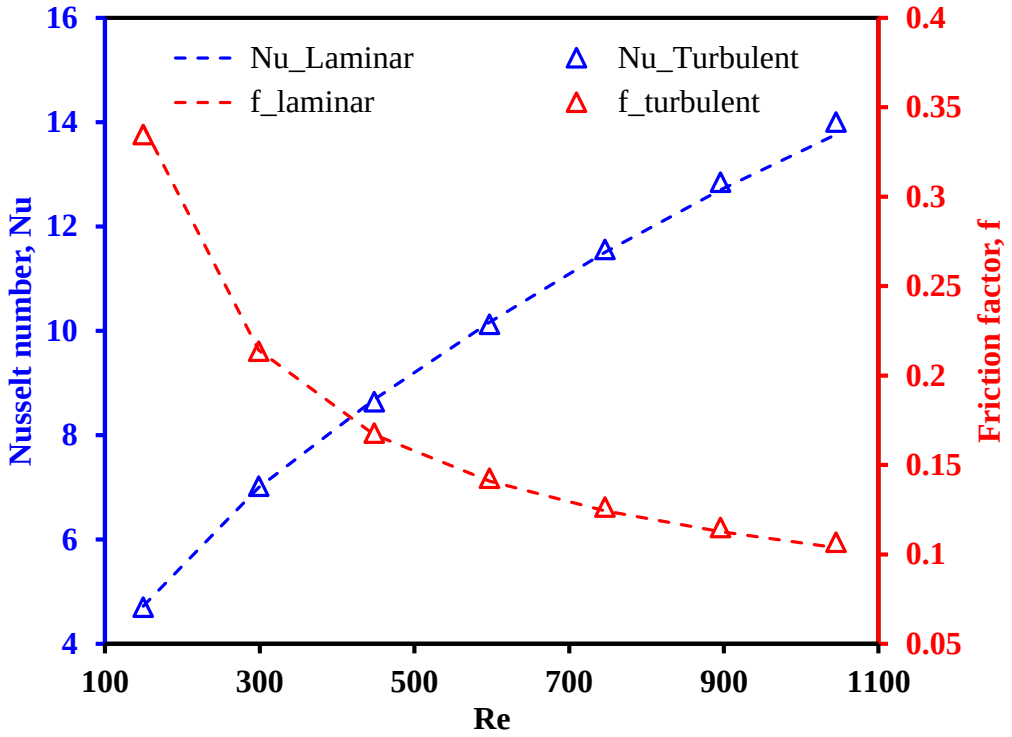

Figure 4.8 Comparison between laminar and turbulent flow model for case 5 in terms of Nusselt number, Nu, and Friction factor, f, at different Re.

in local turbulence in the vicinity of the inter-connectors as a consequence of the flow separation and reattachment even at lower Re [76-77]. Therefore, to ensure the reliability of the laminar flow assumption, a comparison between laminar and turbulent flow simulation was performed. For turbulent flow simulation, SST $k-\omega$ turbulence model was chosen which is a two-equation eddy viscosity turbulence model [78]. Second-order upwind scheme was used for both momentum and energy equations. Detail information about the turbulent flow modeling is attached in Appendix A. From the Figure 4.8, it can be observed that both laminar and turbulent flow model are showing the same trend for Nusselt number and friction factor for all Re range. The average deviation between laminar

and turbulent flow Nusselt number and friction factor are less than 0.72% and 1.42% respectively, this validates the reliability of the laminar flow assumption.

4.8.2 Characteristics of Pressure, Velocity, and Friction Factor

To understand the effect of inter-connector on velocity distribution, and heat transfer characteristics of the parallel and counter flow mini-channel heat sink, understanding of the effect of inter-connector on the pressure field is essential. Figure 4.9 shows the non-dimensional pressure field for parallel and counter flow mini-channel heat sinks in the plane of z=Hs+H/2 and at Re=747. In case of inter-connected parallel flow mini-channel heat sink, since coolant is flowing in the same direction through both channels, therefore there should be no pressure difference across the inter-connector as shown in the Figure 4.9 (a) which nullify the Bernoullis effect and secondary flow as well. However, in case of counter flow mini-channel heat sinks, there is substantial pressure difference across the inter-connector because of opposite flow direction through the adjacent channels. That's results in some secondary flow through the inter-connector which is responsible for the break-up of the thermal and hydraulic boundary layer. Meanwhile, the adverse pressure gradient is evident at the leading edge of the inter-connector especially at the higher width of the inter-connector (case 5) as shown in Figure 4.9 (b). This adverse pressure effect is acceptable as the flow passes over the sharp edge of the inter-connector, separation and reattachment of the flow occur. In the downstream of the flow separation, there is recirculation inside the inter-connector.

Figure 4.10 depicts the non-dimensional pressure along the centerline of channel 1 at Re=746 for both parallel and counter flow mini-channel heat sink and also for all width of the inter-connector (case 1-5). In case of parallel flow, pressure reduction is almost linear

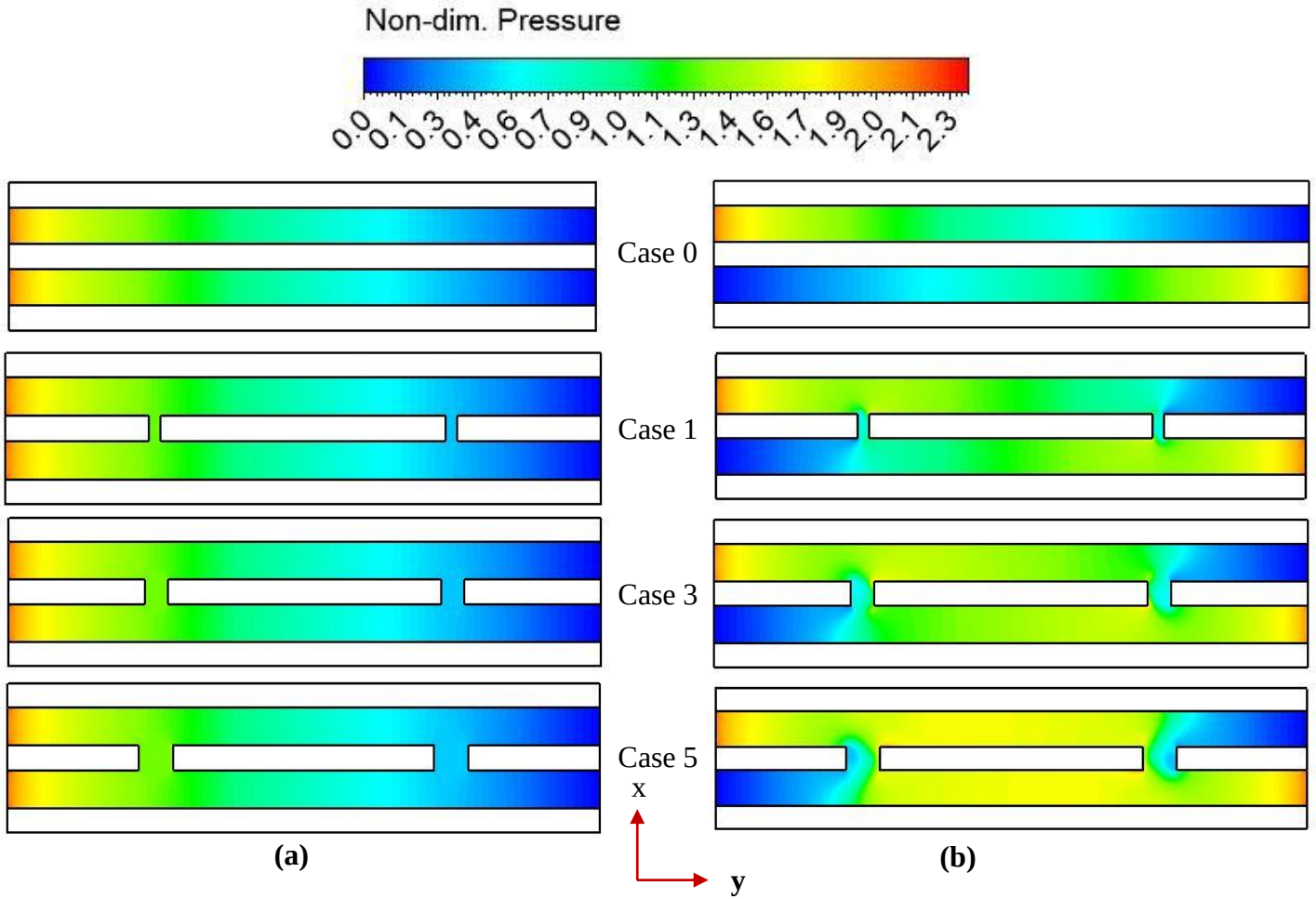

Figure 4.9 Non-dimensional pressure contours in the central x-y middle cross-section of (a) parallel and (b) counter flow mini-channel heat sink at $Re = 746$.

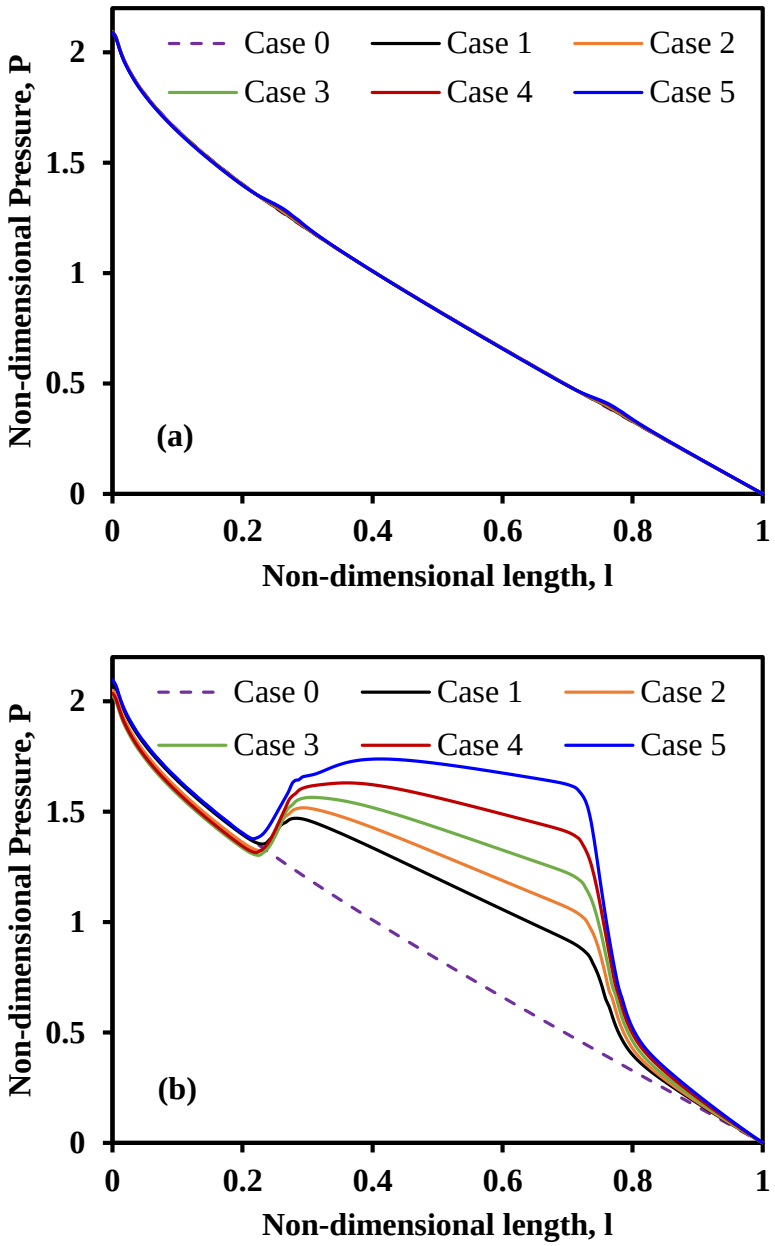

Figure 4.10 Non-dimensional pressure along the center line ($z=H_s+H/2$) of channel 1 for (a) parallel and (b) counter flow mini-channel heat sink at $Re = 746$.

from the inlet to the outlet of the channel as shown in the Figure 4.10 (a) irrespective of the presence of the inter-connector. However, some portion of the incoming coolant flows from channel 1 to channel 2 in counter flow heat sink because of the noticeable pressure difference across the inter connector. After the downstream of the first inter-connector, less

amount of coolant is flowing through the same cross-sectional area of the channel, that leads to adverse pressure gradient in the junction of the inter-connector and the main flow passage as shown in the Figure 4.10 (b). Moreover, the amount of coolant flows through the inter-connector increases for the higher width of the inter-connector (case 1-5). That results in a gradual increment of the adverse pressure gradient in the downstream of the first inter-connector. Afterward, the same amount of coolant that leaves the channel 1 through first inter-connector returns to channel 1 from channel 2 through the second inter-connector which increase the mass flow rate of the coolant in the downstream of the second inter-connector and subsequently reduces the pressure drop as shown in the Figure 4.10 (b).

Non-dimensional velocity distribution and streamlines for both parallel and counter flow heat sinks (with and without inter-connector), along with the flow directions in the plane of $z= H_s+H/2$ at Re= 746 are shown in Figure Figure 4.11 and Figure 4.12 respectively. For parallel flow mini-channel heat sink, negligible pressure difference across the inter-connector creates two stationary recirculation zones inside the inter-connector which results in no secondary flow through the inter-connector regardless of the width of the inter-connector as shown in the Figure 4.11 (a) and Figure 4.12 (a). But from the Figure 4.12 (a), it is clearly evident that the intensity and mixing zone of the two recirculation zone inside the inter-connector increased at the higher width of the inter-connector. However, for counter flow heat sink, four most notable effects are occurring such as the significant amount of cross-flow through the inter-connector, flow separation, recirculation, and reattachment. In case of counter flow heat sink, coolant is flowing in the opposite direction through the adjacent channels, therefore noticeable pressure difference

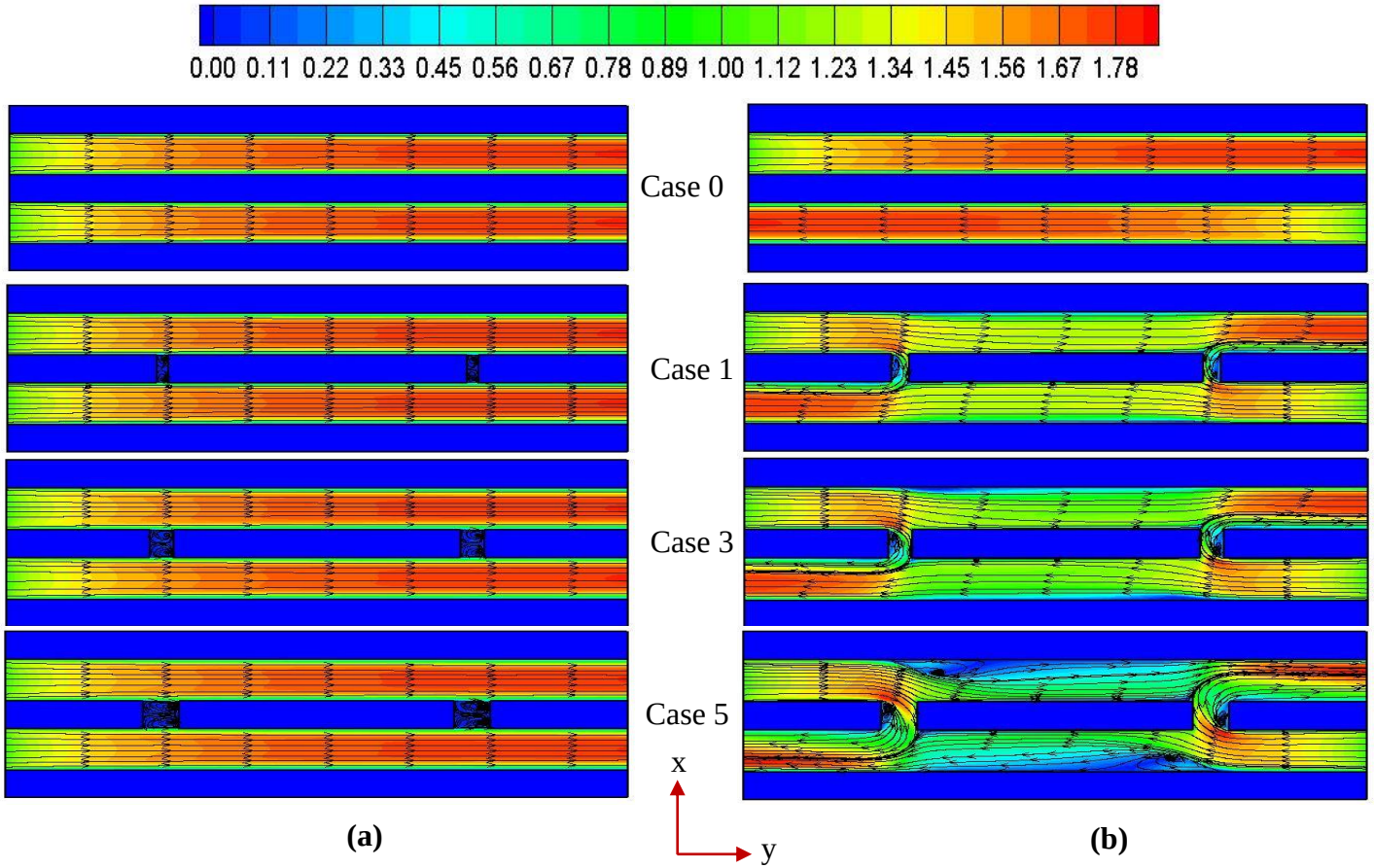

Figure 4.11 Non-dimensional velocity contours in the central x-y middle cross-section of (a) parallel and (b) counter flow mini-channel heat sink at $Re = 746$.

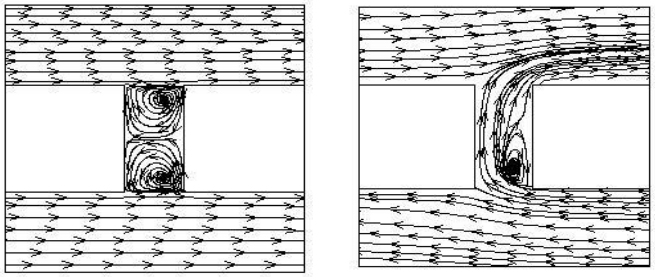

Case 1

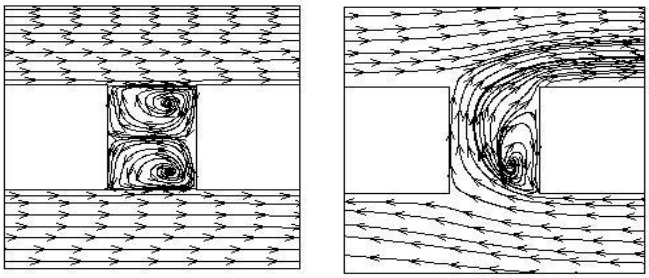

Case 2

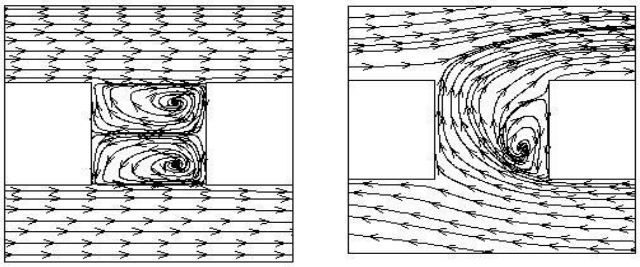

Case 3

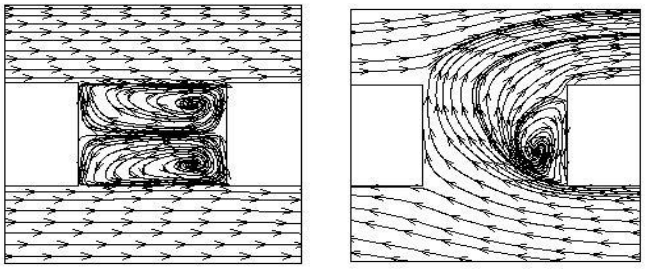

Case 4

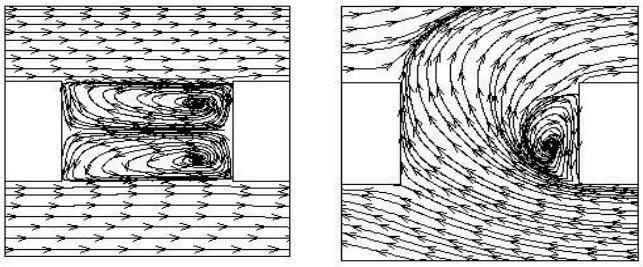

(a) Case 5 **(b)**

Figure 4.12 Streamline inside the inter-connector of (a) parallel and (b) counter flow mini-channel heat sink at $Re = 746$.

across the inter-connector is evident. That pressure difference results in some cross flow of the incoming coolant through the inter-connector from the high-pressure side to the low-pressure side as shown in the Figure 4.11 (b) and Figure 4.12 (b). The secondary flow of the coolant interrupts the hydraulic and thermal boundary layer. But at the same time, flow separation occurs at the sharp leading edge of the inter-connector which leads to a recirculation zone close to the leading edge of the inter-connector, as shown in the Figure 4.12 (b). From the Figure 4.12 (b), it can also be seen that, at the lower width of the inter-connector (case 1 and 2), the intensity of the recirculation zone is less and reattachment of the secondary flow occurs outside of the inter-connector. But at the higher width of the inter-connector (case 3-5), the intensity of the recirculation zone is increasing and also the reattachment point is gradually shifting inward from the trailing edge of the inter-connector. It is worth mentioning that the amount of coolant flows through the inter-connector increases with the width of inter-connector which significantly reduces the coolant velocity in-between two inter-connector. The increased coolant flow initiates another circulation zone in the downstream of the inter-connector due to an additional adverse pressure gradient and a static no-slip boundary condition in the wall of the main channel as shown in the Figure 4.11 (b).

Figure 4.13 illustrates the non-dimensional velocity of the coolant for the parallel and counter flow heat sink along the centerline of the channel 1 at Re=746. From the Figure 4.13 (a), it can be seen that, for parallel flow heat sink, the effects of inter-connector on the

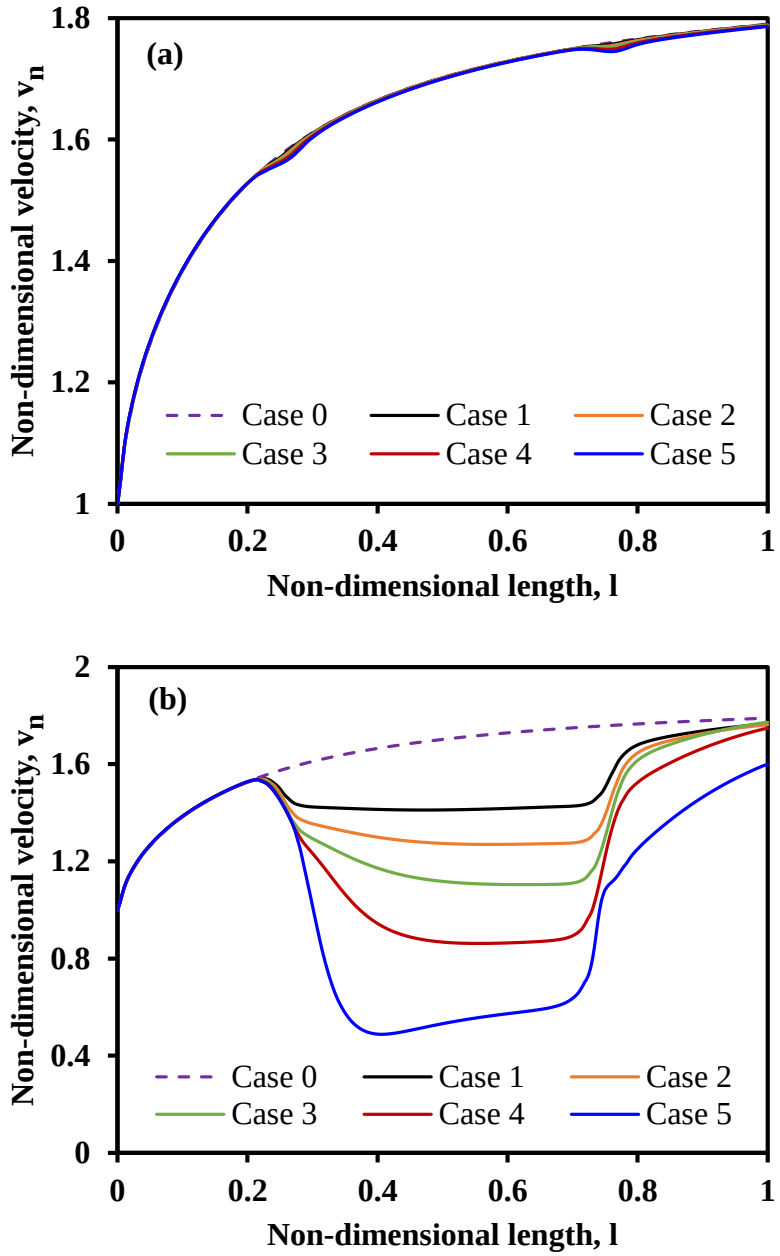

Figure 4.13 Non-dimensional velocity along the center line ($z=H_s+H/2$) of channel 1 for (a) parallel and (b) counter flow mini-channel heat sink at $Re = 746$.

mainstream velocity is very negligible as explained earlier. However, for counter flow mini-channel heat sink, some portion of the incoming coolant is passing through the first inter-connector to channel 2 as cross-flow which reduces the mainstream velocity in the downstream of the inter-connector. Since through the second inter-connector, some coolant

is entering to the channel 1 from channel 2, the velocity of the coolant again increase as shown in the Figure 4.13 (b). Moreover, in case of the highest width of the inter-connector (case 5), very high-velocity gradient is evident between the downstream of the junction of the inter-connector and main channel which results in a second recirculation zone as shown in the Figure 4.11 (b).

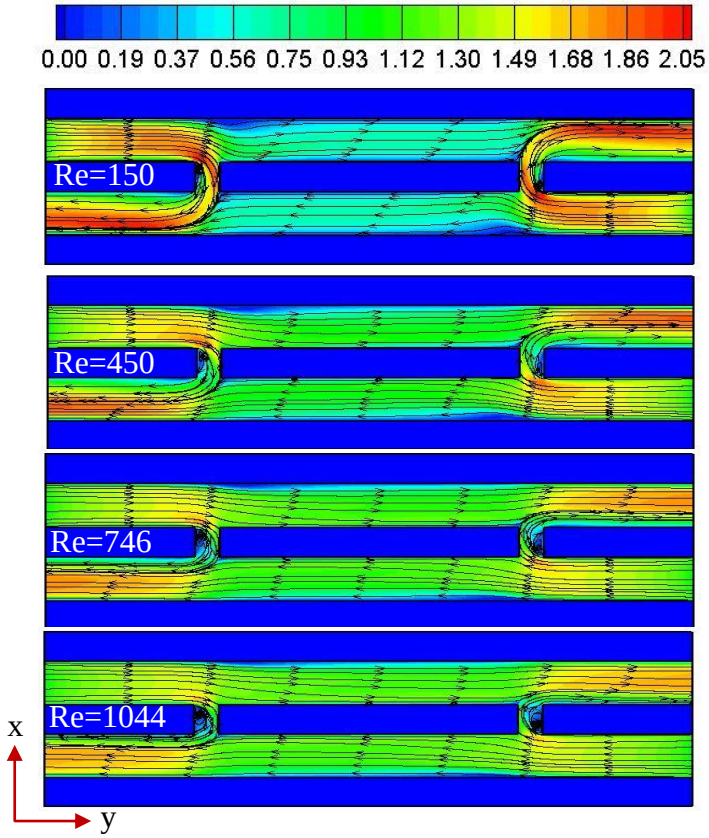

Figure 4.14 Non-dimensional velocity contours in the central x-y middle cross-section of counter flow mini-channel heat sink for case 3.

Figure 4.14 depicts the velocity distribution of the inter-connected counter flow heat sink at different Re for case 3. It is worth mentioning that at low Re, coolant velocity and consequently momentum is also low which results in higher secondary flow through the inter-connector despite less pressure difference across the inter-connector. In addition

to that, less adverse pressure gradient in the junction of inter-connector and main channel creates small recirculation zone inside the inter-connector which is also favorable for transverse flow. Therefore, a significant amount of coolant flows transversely which results in substantial reduction of coolant velocity in the downstream of the connector. However, in case of higher Re, less amount of coolant flows transversely because of bigger recirculation zone inside the inter-connector as a result of more adverse pressure gradient and also because of higher momentum along the flow direction (y-direction) of the incoming coolant as shown in the Figure 4.14.

Figure 4.15 illustrates the variation of friction factor with Re for parallel and counter flow mini-channel heat sinks. From the Figure 4.15, it can be observed that with an increase of Re, friction factor reduces for all cases (case 0-5). This is because of the reduction of boundary layer thickness with Reynolds number which consequently reduces the friction factor. Inter-connector between two parallel flow mini-channel shows negligible effects on the friction factor concerning the conventional mini-channel heat sinks as shown in the Figure 4.15 (a). This can be attributed to almost no cross flow through the inter-connector regardless of the width of the inter-connector. However, for the counter flow heat sinks, a substantial reduction in friction factor is evident at low Reynolds number (<600) as shown in the Figure 4.15 (b). In this cases, three important parameters are mainly affecting the friction factor behavior such as the amount of transverse coolant flow, breakup and redevelopment of the hydrodynamic boundary layer, and also the velocity distribution of the coolant throughout the channels. At low Re, coolant is approaching the fully developed flow before reaching to each inter-connector, so the thickness of the hydrodynamic boundary layer is maximum which provides minimum shear stress and also

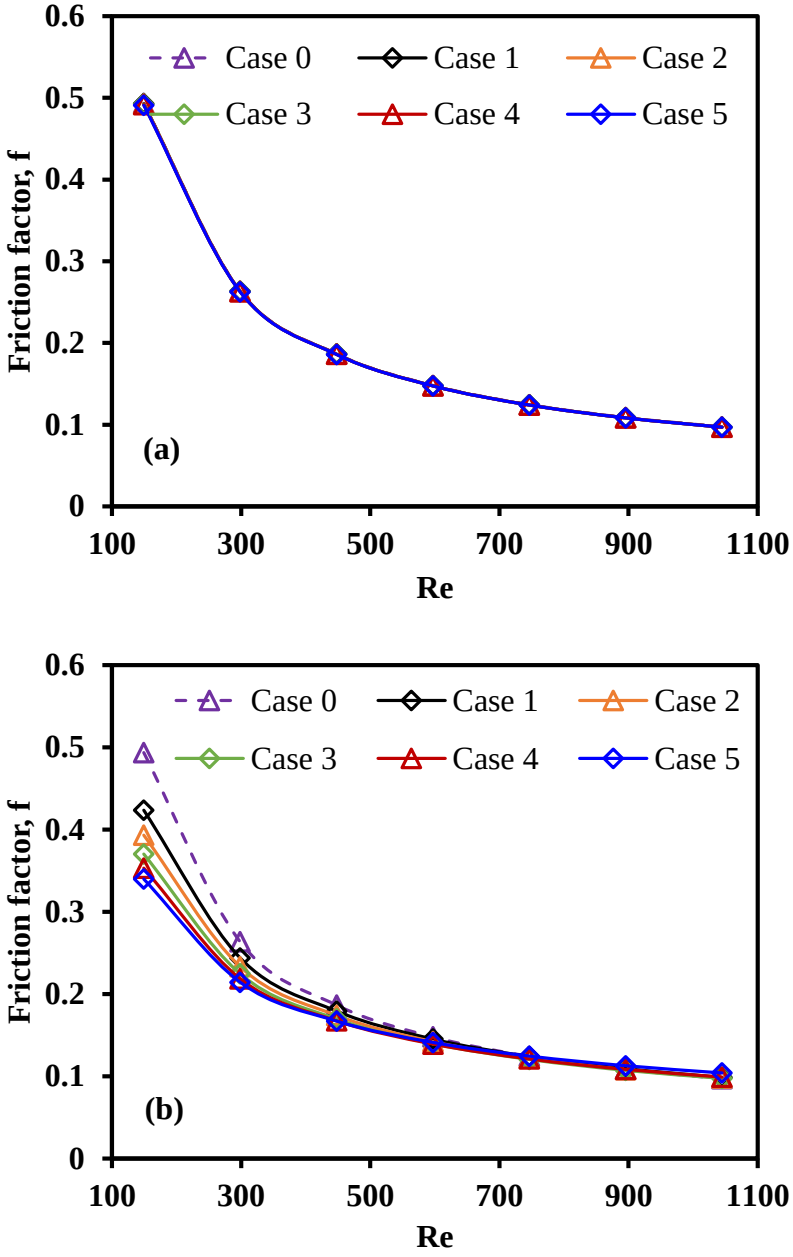

Figure 4.15 Overall friction factor vs. *Re* graph for (a) parallel and (b) counter flow mini-channel heat sink.

minimum possible local friction factor. It is worth mentioning that at low Re, transverse coolant flow through the inter-connector is high. Therefore, a reduced amount of the coolant flow through the main channel reduces the pressure drop requirement in between two inter-connectors. Consequently, the increased amount of cross-flow significantly break

and re-initialize the hydrodynamic boundary layer in the junction of inter-connector and the main channel which increase the shear stress value in the starting region of every individual hydrodynamic boundary layer. As a resultant of the two opposite behavior in the pressure drop requirement, the overall friction factor value of inter-connected heat sink reduced at low Re. On the contrary, at higher Re, the flow is hydrodynamically developing throughout the channel and also for the higher momentum of the coolant along with bigger recirculation zone, less amount of coolant flows transversely. Therefore almost all amount of the incoming coolant travels the full length of the mini-channel heat sink. As a result, the overall friction factor of all the inter-connected heat sink (case 1-5) is very comparable to the conventional channel as shown in the Figure 4.15 (b). From the Figure 4.15 (b), it can also be seen that, at a particular Re, friction factor decreases with the width of inter-connector especially for Re less than 450. This phenomenon was due to a significant reduction of coolant flow at the higher width of the connector in the downstream of the first inter-connector as explained earlier.

Figure 4.16 illustrate the ratio of friction factor of inter-connected mini-channel to the conventional parallel flow mini-channel for all width (case 0-5). As seen in the Figure 4.16 (a), for parallel flow heat sink, the friction factor reduced by maximum 0.5% and 0.26% respectively at Re=150, and 1044 and for the highest width of the connector (case 5). For counter flow heat sink, maximum reduction of friction factor occurs at lowest Re and also for the highest width of the inter-connector. For example, for case 5, a maximum 31.13% reduction in friction factor occurs at Re=150. Afterward for all cases, friction factor ratio increases with the increase of Re to a moderate value with an approximately linear positive slope. But at high Re, friction factor ratio reach almost a constant value

(± **1**%) by lowering the increment slope except for case 4 and 5. Since for case 4 and 5, the width of the inter-connectors are comparable to the width of the main channel, so in

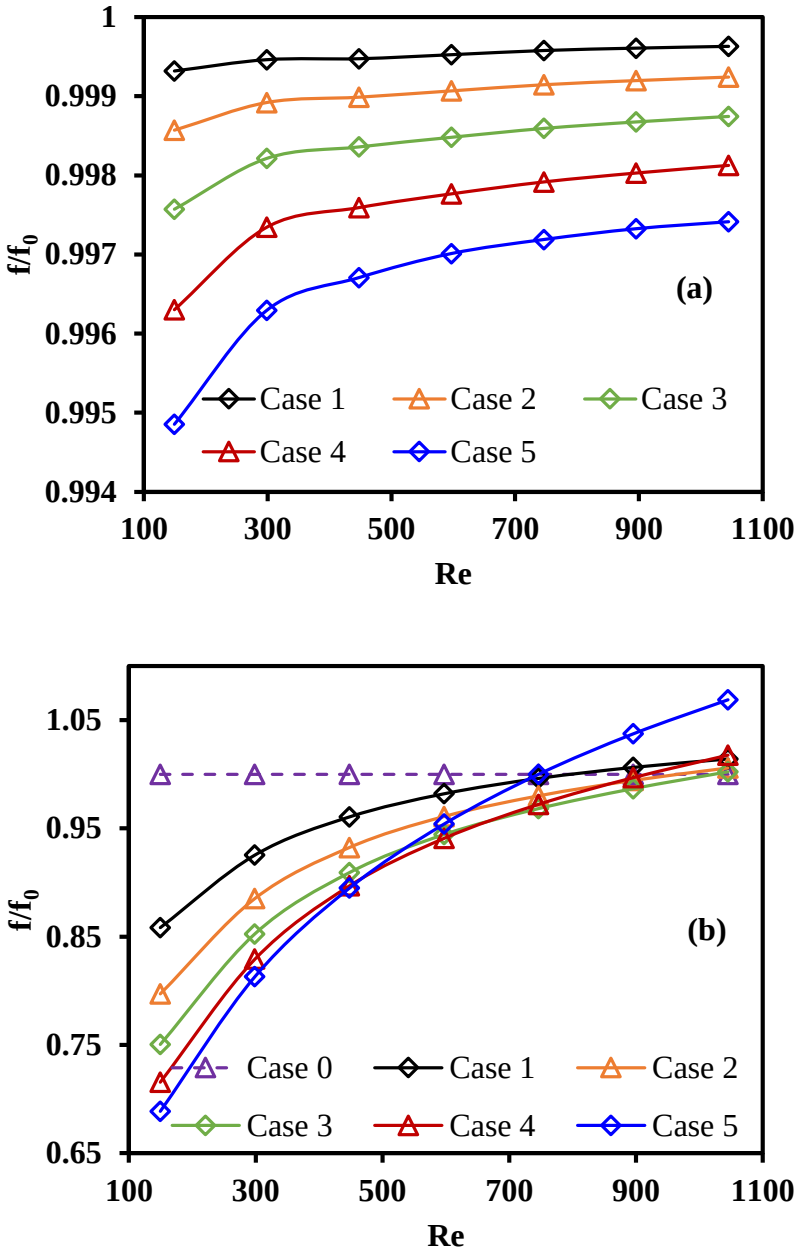

Figure 4.16 Overall friction factor ratio vs. *Re* graph for (a) parallel and (b) counter flow mini-channel heat sink.

these cases extra generated intense recirculation zone in the mini-channel imposes some extra flow resistance which results in higher friction factor as explained previously.

From the Figure 4.16 (b), it can also be observed that for all cases at higher Re (~1044), the value of friction factor is more than 1.

4.8.3 Characteristics of Temperature Distributions

Figure 4.17 presents the temperature distribution at the bottom surface (in the plane of $z=H_s$) of the parallel and counter flow heat sinks at Re=746. Since thermal boundary layer is developing continuously from the inlet of the conventional parallel flow mini-channel heat sink (case 0), these thicker boundary layers impose more thermal resistance resulting in higher surface temperature in the downstream of the mini-channel heat sink as shown in the Figure 4.17 (a). However, in case of the counter flow heat sink (case 0), coolant is entering from two opposite side, thus the surface temperature at the two inlets of the heat sink goes down but in the center region of the heat sink goes up due to thicker thermal boundary layer at this region as illustrates in the Figure 4.17 (b) which results in even higher average surface temperature than parallel flow heat sink. Figure 4.17 (a) shows the effect of the inter-connector on the surface temperature distribution in case of parallel flow heat sink. Negligible interruption of the thermal boundary layer is evident in the Figure 4.17 (a) for all width of the inter-connector (case 1-5) which leads to almost similar surface temperature distribution with respect to the conventional parallel flow heat sink. In addition to that, two stationary recirculation zone increases the surface temperature inside the inter-connector, especially in the second inter-connector, regardless of the width of the inter-connector (case 1-5). However, in case of the inter-connected counter flow heat sink, a sudden interruption of the thermal boundary layer occurs in the junction of the inter-connector and main channel because of the substantial transverse flow of the coolant

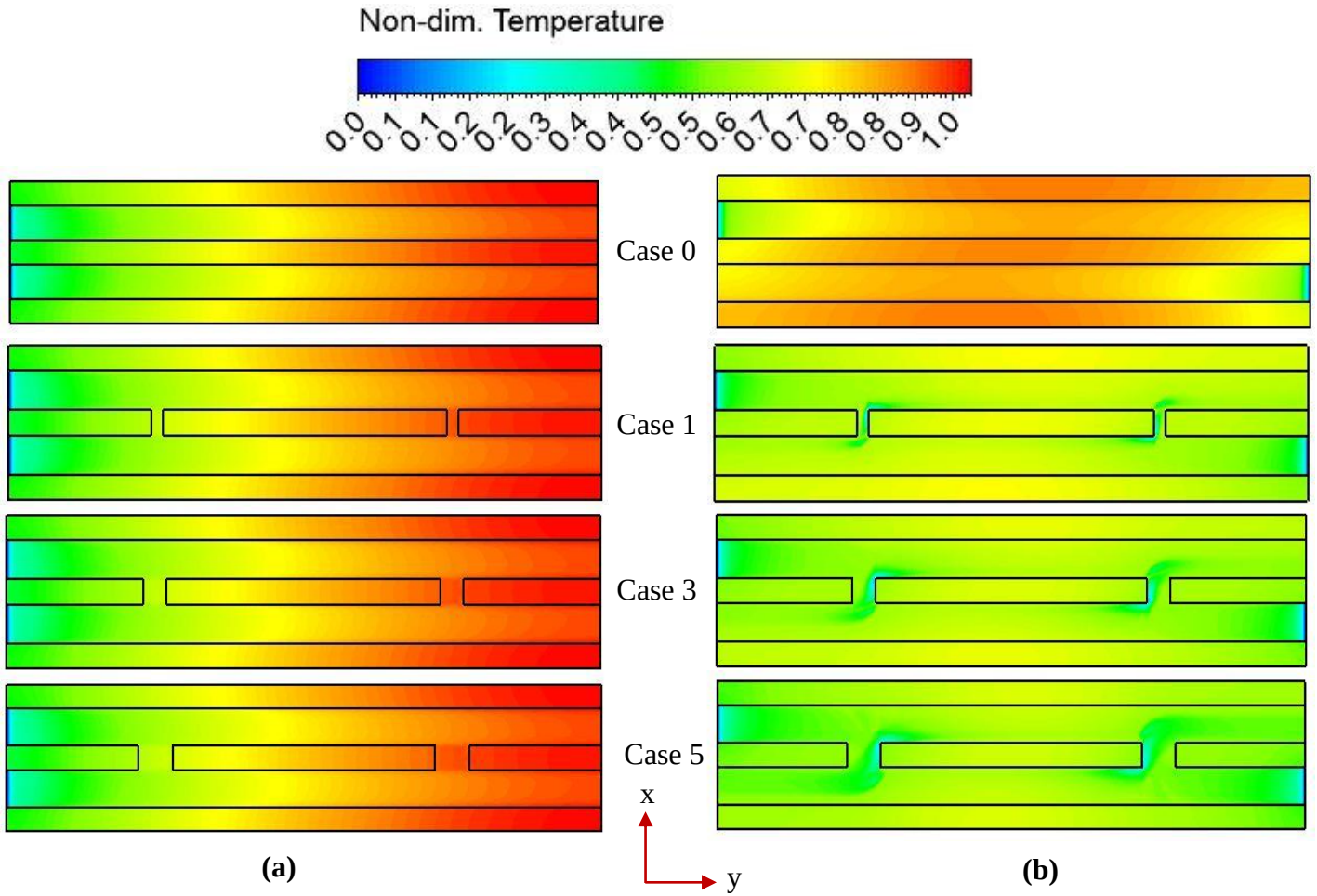

Figure 4.17 Non-dimensional temperature contours in the bottom plane ($z=H_s$) of (a) parallel and (b) counter flow mini-channel heat sink at $Re = 746$.

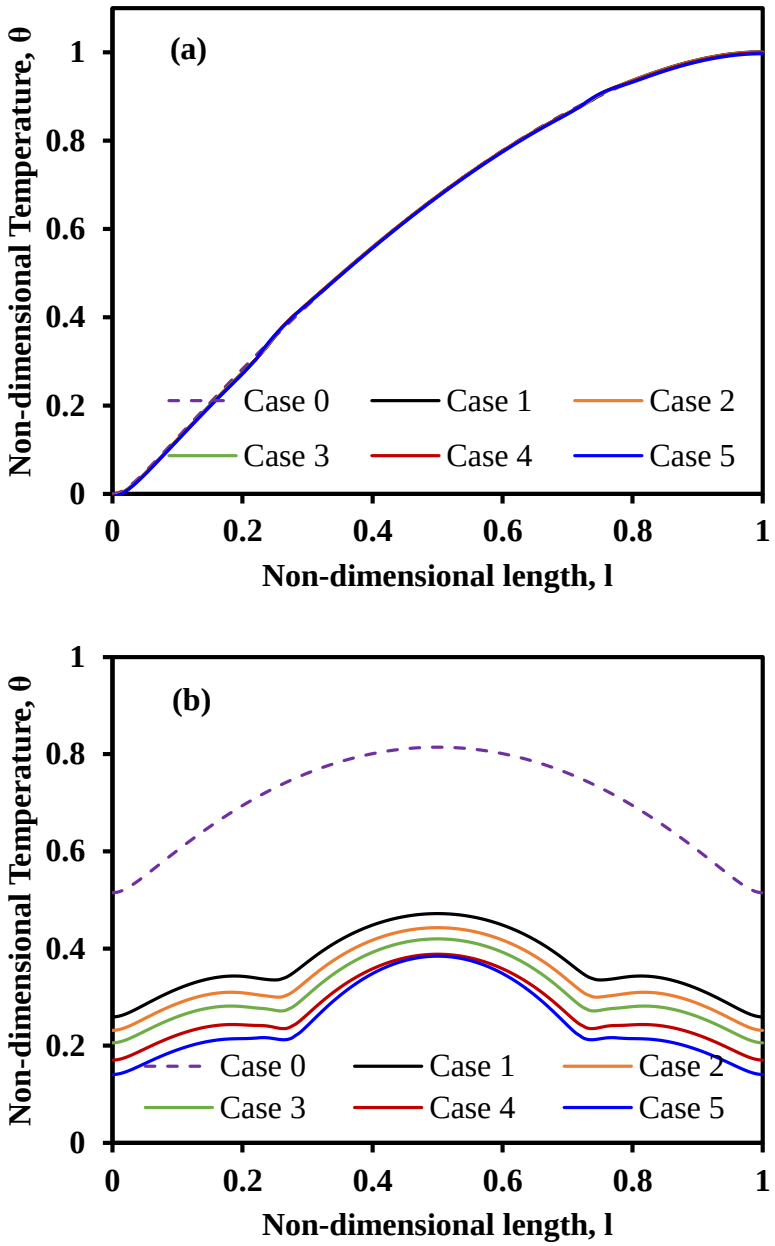

Figure 4.18 Non-dimensional temperature along the center line of base surface (z=0) for (a) parallel and (b) counter flow mini-channel heat sink at $Re = 746$.

as demonstrates in Figure 4.17 (b). Inside the inter-connector, opposite surface temperature distribution is observed on both sides of the mixing layer as shown in the Figure 4.17 (b) for all width of the inter-connector (case 1-5). This indicates that surface temperature goes up in one side of the mixing layer because of the recirculation zone and surface temperature

goes down in the other side of the mixing layer, because of direct impingement of the coolant on the inter-connector wall as shown in the Figure 4.11 (b) and Figure 4.12 (b).

The variation of non-dimensional temperature for the parallel and counter flow heat sink along the centerline of the heat sink base (z=0) at Re=746 is shown in Figure 4.18. From the Figure 4.18 (a), it can be illustrated that for all parallel flow heat sinks (case 0-5), the centerline temperature growth is not linear along with the flow direction, and it reaches to the maximum value a little upstream of the outlet because of the thermal conduction in solid near the end of the heating area. Base surface temperatures of the inter-connected parallel flow heat sinks (case 1-5) show almost same behavior as a conventional parallel flow heat sink because of the negligible cross flow of the coolant between two channels as explained earlier. But for counter flow mini-channel heat sink (case 0-5), the base surface temperature exhibits symmetric behaviour respect to the center point of the heat sink ($l = 0.5$) and also the surface temperature is relatively high at both ends of the heat sink with respect to the parallel flow heat sink beacuse of the reduced coolant flow rate from two inlet as shown in the Figure 4.18 (b). Afterward base temperature increase gradually and a slight negative gradient is evident in the upstream of the first inter-connector (case 1-5). However, the base surface temperature again increases gradually in the downstram of the first inter-connector because of the reduced velocity of the coolant as explained in the Figure 4.13 (b) and reaches a pick value in the middle of the heat sink ($l = 0.5$). Moreover, in the downstream of the center region, the surface temperature again goes down and shows symmetric behavior as the first half length of the heat sink because of the opposite flow direction of the coolant through the adjacent channel. From the Figure 4.18 (b), it can also be seen that surface temperature reduces more for the higher width of

the inter-connector. This can be attributed to the higher interruption of the theraml boundary layer for the higher cross flow of the coolant through the inter-connector at the higher width of the inter-connector as shown in the Figure 4.18 (b).

4.8.4 Heat Transfer Characteristics

Figure 4.19 (a) illustrate the relationship between the average Nusselt number (Nu) and Reynolds number for parallel flow mini-channel heat sink. It is noted that the net heat transfer enhancement can be achieved by two mechanisms: (i) by increasing the effective heat transfer area and (ii) by interruption and redeveloping the thermal boundary layer. Since for the present inter-connected mini-channel heat sink, the surface area is increased by only 1.54% with respect to the conventional heat sink, therefore the heat transfer enhancement achieved via enhanced surface area is negligible which indicates that heat transfer enhancement is primarily achieved by interrupting the thermal boundary layer. Since in case of inter-connected parallel flow mini-channel heat sink, there is almost no secondary flow through the inter-connector resulting two stationary recirculation zones inside the inter-connector. Therefore, the surface temperature goes up which attributes to a slight reduction of Nu with respect to conventional channel as shown in the Figure 4.19 (a). However, in case of counter flow mini-channel heat sink, the significant increment of Nu is evident in the Figure 4.19 (b) because of the substantially higher secondary flow which results in higher interruption and re-development of the thermal boundary layer and also increased mixing of the hot and cold coolant stream as shown in the Figure 4.12 (b) and Figure 4.17 (b). Furthermore, at low Re and the higher width of the inter-connector, the reduction of coolant velocity in between two inter-connectors is more significant than the interruption of the thermal boundary layer because of the thicker boundary layer. That

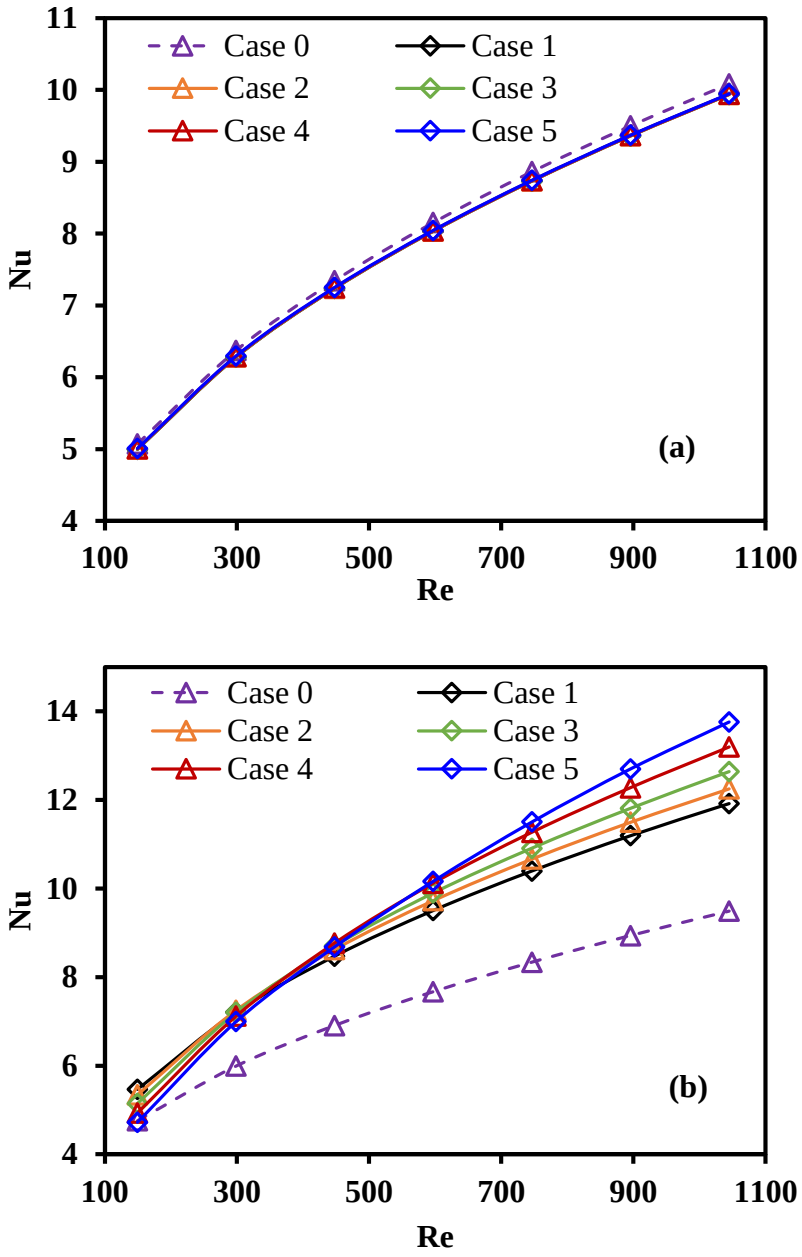

Figure 4.19 Overall Nu vs. Re graph for (a) parallel and (b) counter flow mini-channel heat sink.

results in higher average surface temperature at the higher width of the inter-connector and consequently reduce Nu. On the contrary, at higher Re, although the amount of secondary flow is reduced as shown in the Figure 4.14, but the interruption of the thermal boundary layer is more significant because of the thinner thermal boundary layer. It is worth

mentioning that low secondary flow indicates higher coolant flow in the downstream of the inter-connector which results in less surface temperature. These two phenomenon attributes to the better thermal performance at the higher width of the inter-connector than the lower width of the inter-connector at higher Re as shown in the Figure 4.19 (b).

The variation of Nusselt number ratio (Nu/Nu_0) with Re are presented in Figure 4.20 for both parallel and counter flow mini-channel heat sink. Since for all inter-connected parallel flow heat sink, there are no interruption of the thermal boundary layer irrespective of the Re, thus the ratio of Nu reaches almost a constant value for all width of the inter-connector (case 1-5) and for all Re. From the Figure 4.20 (a), it can also be seen that, at all width of the inter-connector (case 1-5), Nu reduces to a smaller value than the conventional parallel flow heat sink. Moreover, for the higher width of the inter-connector (case 2-5), interfacial contact line between two parallel streams inside the inter-connector increases as shown in the Figure 4.12 (a) which results in relatively higher heat transfer. For counter flow mini-channel heat sink without inter-connector, the average surface temperature is higher than the parallel flow heat sink that results in Nu ratio less than 1 as shown in the Figure 4.20 (b). Since at low Re, the coolant velocity reduced significantly in the downstream of the first inter-connector which result in an unfavorable effect on the heat transfer performance. This phenomenon increases with the increase of the inter-connector width as shown in the Figure 4.20 (b). For example, at Re=149, the Nusselt number increase by ~7.70% for case 1 and reduced by ~6.95% for case 5 with respect to case 0. However, from the Figure 4.20 (b), it can be observed that for all width of the inter-connector (case 3-5), the ratio of the Nu increases with the increase of Re with a gradually decreasing positive slope while for case 1-2, the ratio of Nu reaches to a constant value at

higher Re (>750). Hence for case 3-5, it can be inferred that the ratio of Nu may reach a constant value beyond the highest considered Re in this study. For case 5, a maximum 36.44% increment in Nu is recorded with respect to the conventional heat sink at Re=1044.

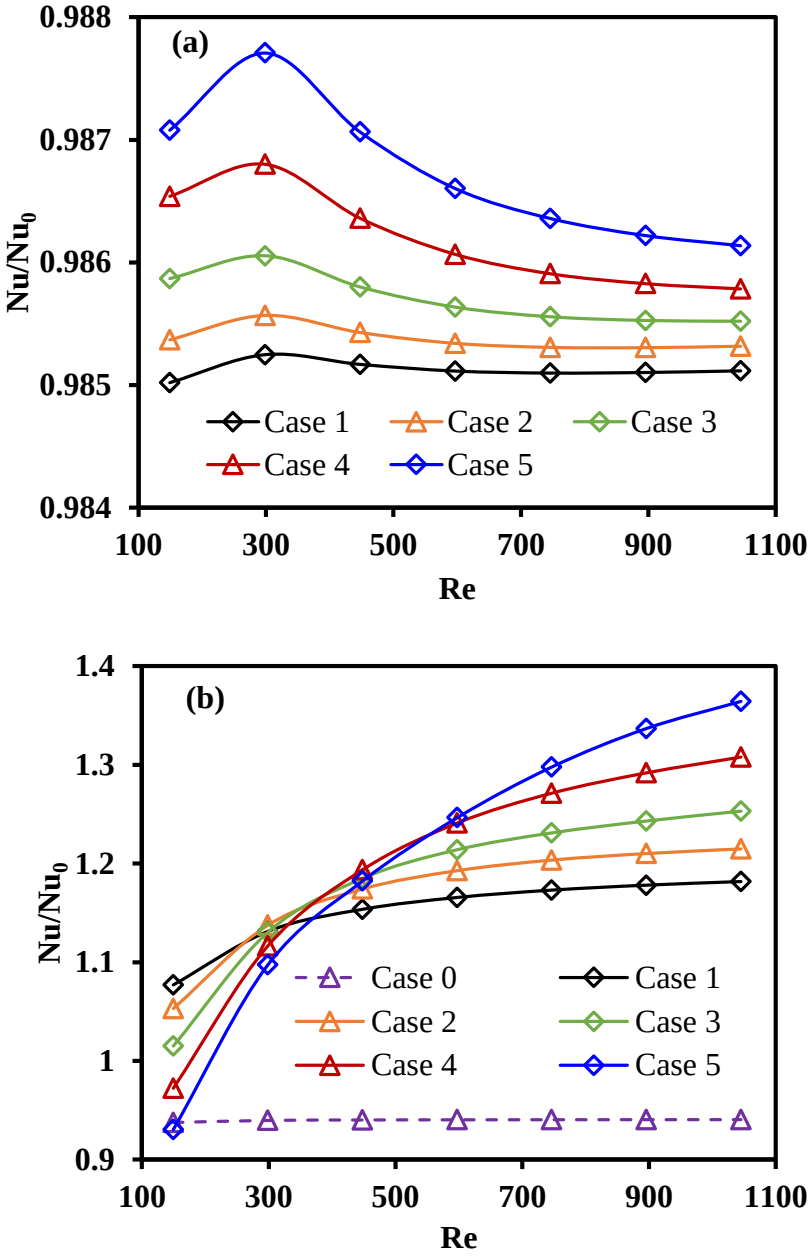

Figure 4.20 Overall *Nu* ratio vs. *Re* graph for (a) parallel and (b) counter flow mini-channel heat sink.

Figure 4.21 illustrate the non-dimensional thermal resistance dependency on Re for both parallel and counter flow mini-channel heat sink. The conductive thermal resistance is greatly dependent on the heat sink dimensions and also on the material properties. On the contrary, the convective and capacitive thermal resistance primarily depends on Re. In case of inter-connected parallel flow mini-channel heat sink, negligible cross flow occurs through the inter-connector which results in minor interruption of the thermal boundary layer and eventually almost same thermal resistance with respect to the conventional heat sink as shown in the Figure 4.21 (a). From the Figure 4.21 (b), it can be observed that for conventional counter flow mini-channel heat sink (case 0), thermal resistance is higher than 1. This can be attributed to the higher average surface temperature than the conventional parallel flow mini-channel as discussed earlier. Since at low Re and the higher width of the inter-connector, the velocity of the coolant is less in the downstream of the first inter-connector, thus higher surface temperature and consequently higher thermal resistance are

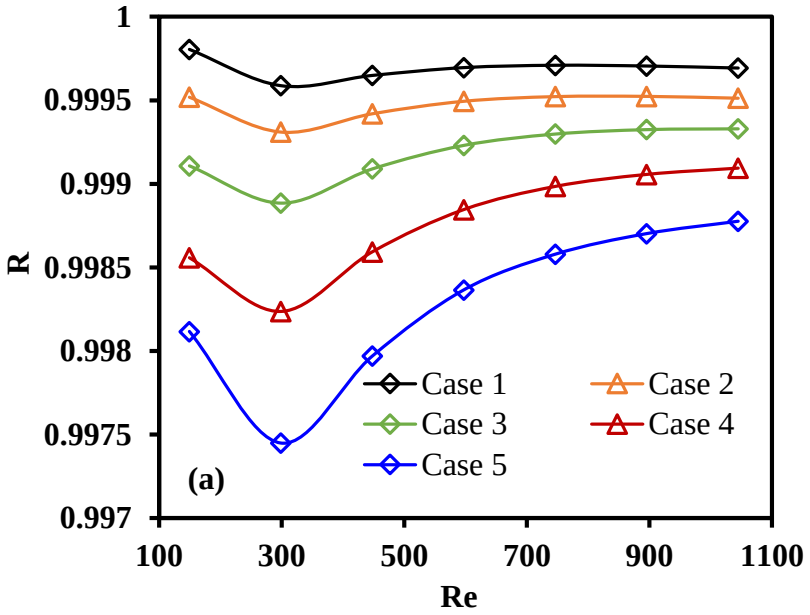

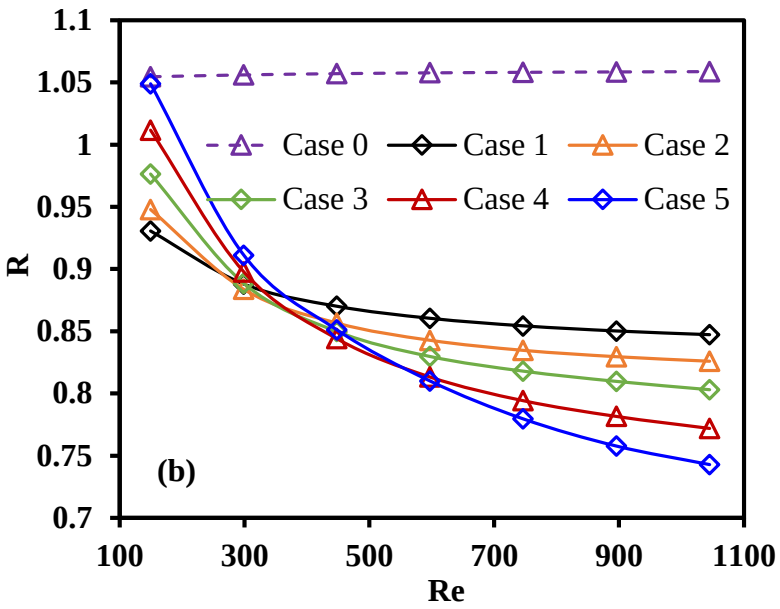

Figure 4.21 Non-dimensional thermal resistance vs. *Re* graph for (a) parallel and (b) counter flow mini-channel heat sink.

evident in the Figure 4.21 (b). For example, At Re=150, the value of non-dimensional thermal resistance for case 5 is 1.05. However, at higher Re, the interruption of the thermal boundary layer increases with the higher width of the inter-connector resulting lower surface temperature of the heat sink and also lower thermal resistance. For example, at Re=1044 and for case 5, the non-dimensional thermal resistance value reduced to 0.74.

4.8.5 Comparison of Performance Evaluation Criteria (PEC)

Figure 4.22 show the performance evaluation criteria for all parallel and counter flow mini-channel heat sink. As seen in the Figure 4.22 (a), all inter-connected parallel flow mini-channel heat sink (case 1-5) share almost the same tendency. As discussed earlier, in case of inter-connected parallel flow heat sink, the ratio of Nu reaches almost a constant value for all width of the inter-connector (case 1-5). That results in a constant value of PEC within whole Re range, and for case 5, the maximum recorded value of the

PEC is ~0.99. On the contrary, since for all cases of inter-connected counter flow heat sink (case 1-5), the ratio of Nu increases with a gradually reducing positive slope, therefore all the PEC curves follow the same trend. The results also revealed that the value of PEC is less than 1 for conventional counter flow heat sink regardless of the Re value. Since at low Re, the value of Nu and the Nu ratio are changing in descending order from small to higher width of the inter-connector width (case 1-5) as shown in the Figure 4.19 (b) and Figure 4.20 (b), while the friction factor values are changing in ascending order from case 5 to case 1 as shown in the Figure 4.15 (b) and Figure 4.16 (b), which results in higher PEC value for case 5 and less PEC value for case 1. Furthermore, with an increase in Re and also in the width of the inter-connector (Case 1-5), PEC for counter flow heat sinks increase because of significantly higher Nu increment and also a negligible increment of the friction factor with respect to the conventional parallel flow heat sink as shown in the Figure 4.20 (b) and Figure 4.16 (b). From the Figure 4.22 (b), it can be seen that the maximum value of the PEC are 1.18, 1.21, 1.25, 1.30, and 1.33 for case 1 to 5 respectively.

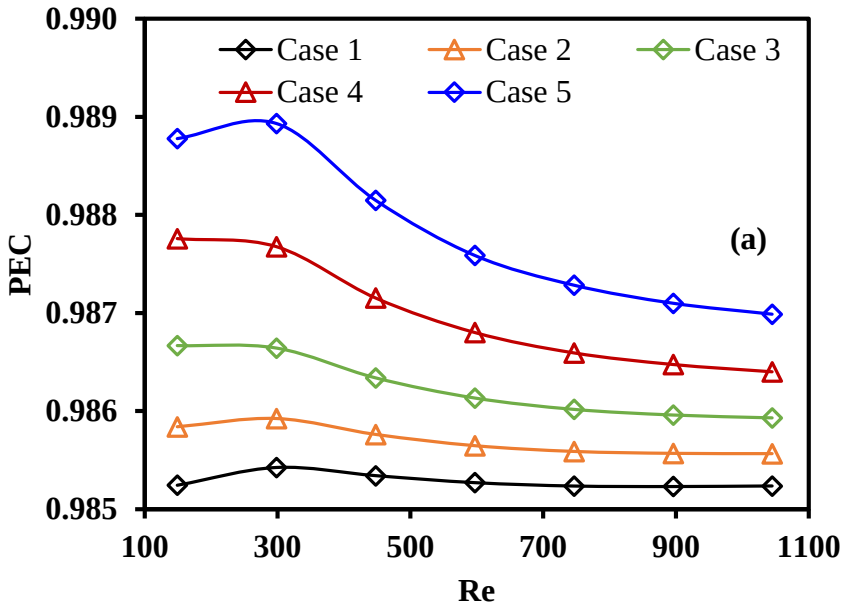

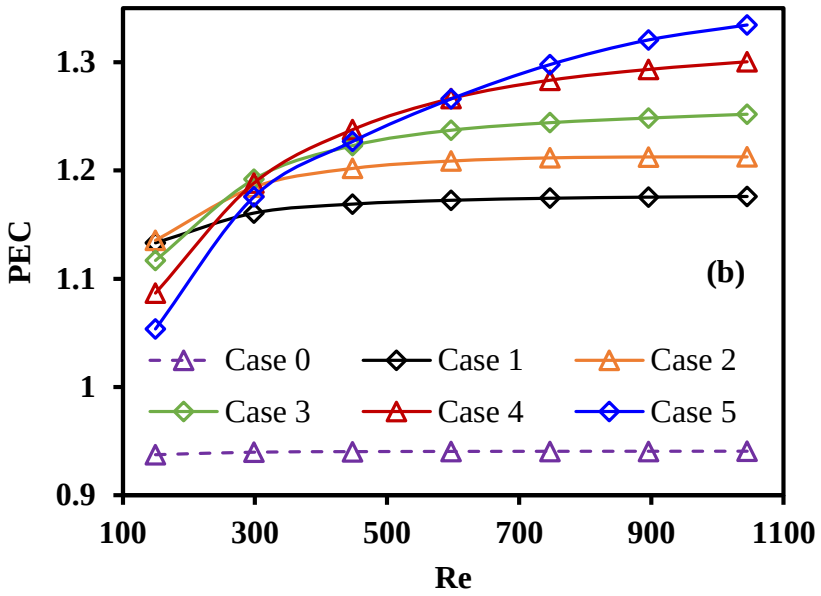

Figure 4.22 PEC vs. *Re* graph for (a) parallel and (b) counter flow mini-channel heat sink.

4.9 Summary

The thermo-hydraulic characteristics of the inter-connected parallel and counter flow mini-channel heat sink in the laminar flow regime (Re=150-1044) under constant heat flux have been investigated by three-dimensional conjugate heat transfer analysis. To quantify the effect of the width of the inter-connector on the fluid flow and heat transfer behavior of both parallel and counter flow heat sink, five different width of the inter-connector (case 1-5) were considered and for every inter-connector width, overall performance were compared based on friction factor, Nusselt number, non-dimensional pumping power, thermal resistance, and performance evaluation criteria (PEC). Based on the numerical investigation following conclusions can be summarized:

1. The inter-connector has a negligible effect on the thermal and hydraulic performance for parallel flow mini-channel heat sink because of the small

pressure difference across the inter-connector which results in almost “no secondary flow” through the inter-connector.

2. In case of counter flow mini-channel heat sink, higher disruption of thermal and hydraulic boundary layer occurs because of higher secondary flow. At the same time, for low flow rate, coolant velocity reduces significantly in-between two inter-connectors which results in higher surface temperature along with less pressure drop.
3. The width of the inter-connector is an important geometric parameter to determine the significance of the cross flow on the Nusselt number for both parallel and counter flow mini-channel heat sink. The maximum increment of Nu for inter-connected counter flow heat sink (case 5) is 36.43% at Re=1044 while Nu reduced by 6.95% at Re=150 with respect to the conventional channel.
4. The pressure drop of the working fluid decreased significantly in inter-connected counter flow mini-channel heat sink especially at low Re; this reduction is more profound at the higher width of the inter-connector. For case 5, a maximum 31.83% reduction of friction factor is recorded at Re=150. The pressure loss penalty is slightly increased at higher Re whereas, in inter-connected parallel flow heat sink, friction factor is almost same as a conventional channel.
5. The maximum value of PEC for parallel flow mini-channel heat sink is ~0.99 for case 5 whereas in case of counter flow heat sink with inter-connector, the value of PEC reached up to 1.33 for the same case and it shows an increasing trend with Re.

CHAPTER 5 EFFECTS OF SECONDARY CHANNELS LOCATION AND WIDTH ON THE OVERALL PERFORMANCE OF COUNTER FLOW MINI-CHANNEL HEAT SINKS

5.1 Introduction

Negligible effect of inter-connector on the thermal-hydraulic performance of the parallel flow mini-channel heat sinks has been idenified in the previous chapter because of almost "no secondary flow" through the inter-connector. However, in case of counter flow mini-channel heat sinks, inter-connector has significant effect on the overall performance. In CHAPTER 4, the author studied the effect of the inter-connectors width for a specified inter-connector location and concluded that for the specified inter-connectors location, maximization of both secondary flow and heat transfer could be achieved by employing different inter-connectors widths at different Reynolds numbers. Moreover, secondary flow not only depends on inter-connectors width, but also greatly depends on the inter-connectors location. Therefore, in the present chapter, the combined effect of the inter-connectors location and width on the overall performance of the counter flow mini-channel heat sinks have been investigated numerically. Three different inter-connectors locations and for each location, three different inter-connectors widths are considered. A comparative 3D conjugate heat transfer analysis has been performed using finite volume based CFD software ANSYS FLUENT for all inter-connected counter flow mini-channel heat sinks with respective to the conventional counter flow mini-channel heat sinks for Re extending from 150 to 1044.

5.2 Geometric Dimensions of the Inter-Connected Counter Flow Mini-Channel Heat Sinks

Figure 5.1 outlines the isometric and front view of the straight fin counter flow mini-channel heat sinks. The heat sink has a total length (L) of 26 mm and width (W_t) of 6 mm. The heat sink consists of two mini-channels which are separated by a solid wall with a constant thickness (W_d) of 1 mm. Each channel has a constant height (H) of 0.5 mm and width (W) of 1.5 mm respectively which results in a hydraulic diameter of 750 μm. The height of the bottom subtrate (H_s) is 0.5 mm and the thickness of the both side walls are 1 mm. The top view of the inter-connected counter flow mini-channel heat sinks along with the main and secondary flow direction is shown in the Figure 5.1. Two inter-connectors devide the whole domain into three seperate zones as shown in the Figure 5.1. Two variables were chosen as the design parameter such as the inter-connectors location (L_i) and width (W_i) as shown in Table 5.1. L_i is denoted as the case specific inter-connectors

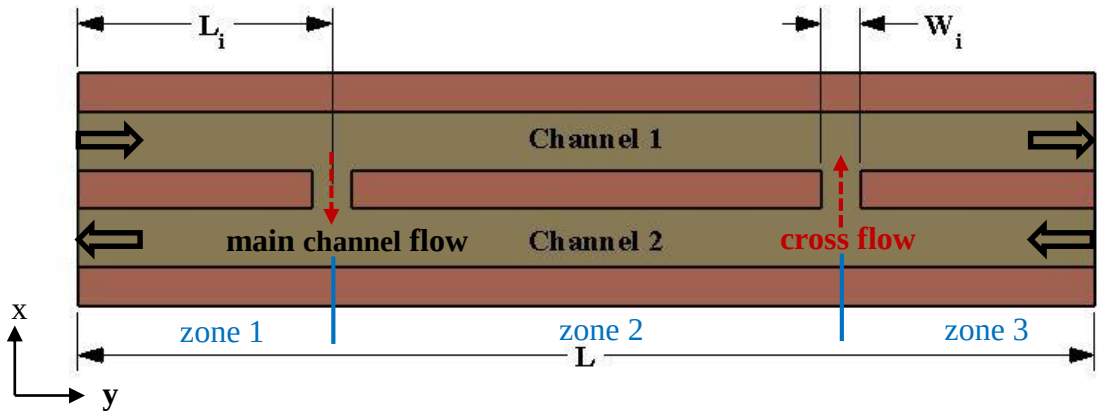

Figure 5.1 Top view of the inter-connected counter flow mini-channels

position from the inlet/outlet of the heat sink, whereas W_i is denoted as the case specific inter-connectors width as shown in Fig. 2. For all cases, both inter-connectors are located at the same distance from the inlet and outlet of the heat sink, and also have the same depth

as the mini-channels. Water was chosen as the coolant, and copper was selected as the substrate material.

Table 5.1 Case specific inter-connector dimensions

Case number, i	L_i (mm)	L_i/L	W_i (mm)	W_i/W
1			1	2/3
2	4	2/13	1.25	5/6
3			1.5	1
4			1	2/3
5	6.5	1/2	1.25	5/6
6			1.5	1
7			1	2/3
8	9	9/26	1.25	5/6
9			1.5	1

5.3 Numerical Simulation

Same numerical simulation procedure as explained in sections 4.3, 4.4, 4.6, and 4.7 in the previous CHAPTER 4 has been followed in this section.

5.4 Data Reduction

In this section, same data reduction procedure as explained in section 4.5 in the previous CHAPTER 4 has been followed except base case (case 0). In this chapter, conventional counter flow mini-channel heat sink is considered as base case (case 0). Therefore, for Nusselt number ratio, (Nu/Nu_0) and friction factor ratio (f/f_0) calculation, results of conventional counter flow mini-channel heat sink have been used as base.

5.5 Results and Discussion

5.5.1 Characteristics of Cross Flow

In case of inter-connected counter flow mini-channel heat sinks, secondary flow through the inter-connectors controls the overall flow friction and heat transfer

performance of the heat sink. Therefore, to get a deep understanding of the secondary flow dependency on the inter-connectors width and location as a function of *Re*, % of secondary flow through the both inter-connectors was studied in detail and was defined as the ratio of the cumulative secondary flow rate through the both inter-connectors $(\dot{m}_{secondary})$ to the total inlet coolant flow rate $(\dot{m}_i)$ as shown below:

$$\%\ of\ secondary\ flow = \frac{\dot{m}_{secondary}}{\dot{m}_i} \times 100\% \tag{5.1}$$

Figure 5.2 depicts the % of secondary flow for all considered inter-connected counter flow mini-channel heat sinks (case 1-9) as a function of *Re*. From the Figure 5.2, it can be seen that for all cases, the % of secondary-flow is gradually reducing from the lower to the higher Re regardless of the location and width of the inter-connectors. Less flow inertia of the coolant at low *Re* results in higher secondary flow despite less pressure difference across the inter-connectors. However, higher flow inertia of the incoming coolant results in less secondary flow at higher *Re* through the inter-connectors for all geometric configurations. From the Figure 5.2, it can be clearly observed that maximum secondary flow occurs in case of the shortest length of zone 1 and 3. For example, a maximum 85.72% of incoming coolant flows transversely in case of 3 while for case 9, a maximum 72.77% of the incoming coolant flows transversely. This can be attributed to the significantly higher pressure difference across the inter-connectors in case of the shortest length of zone 1 and 3 which eventually results in higher secondary flow. Furthermore, at any particular Re, a higher width of the inter-connectors results in higher secondary flow regardless of the inter-connectors location as evident in the Figure 5.2.

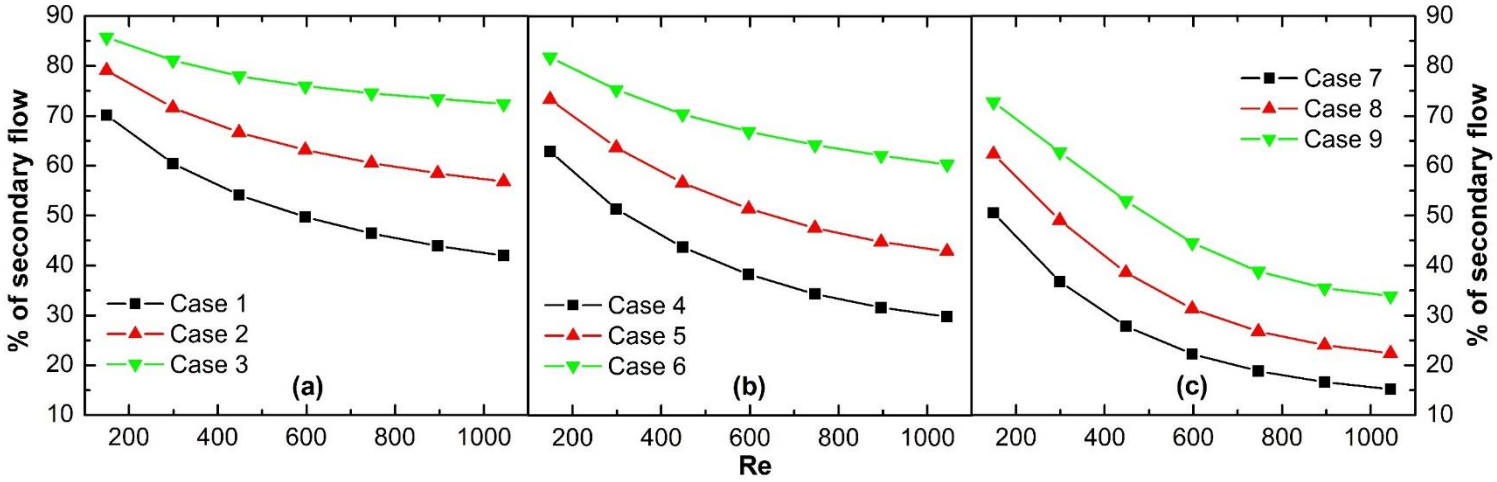

Figure 5.2 % of secondary flow.

5.5.2 Characteristics of Pressure Distribution:

The amount of secondary flow is primarily triggered by pressure and velocity distribution, therefore, the pressure, and velocity fields were studied thoroughly. In order to visualize the effect of inter-connectors location on the pressure profile, comparative analysis between case 2, 5, and 8 along with conventional channel (case 0) have been performed by referring to the pressure contour on the mid x-y plane of the both channels (z=0.75mm) at Re=597. Since in case of counter flow mini-channel heat sink, coolant flows in the opposite direction through the adjacent channels, pressure is gradually reducing along the streamwise direction of both channels as shown in Figure 5.3 (a). This pressure difference between the adjacent channels generates the secondary flow through the inter-connectors in case of inter-connected counter flow mini-channel heat sinks as a resultant of the Bernoullis effects. At the shortest length of zone 1, highest pressure differences across the inter-connectors are evident in the Figure 5.3 (b), which results in a substantial reduction of secondary flow and pressure drop across zone 1. Moreover, almost uniform pressure distribution is evident in zone 2 because of very minimal coolant flow through this zone. Afterward, a sudden reduction in pressure is evident in zone 3 as a resultant of increased coolant amount. Pressure difference across the inter-connectors reduces as the length of zone 1 increases as shown in the Figure 5.3 (c) and (d) which eventually reduces the amount of secondary flow as explained earlier. Hence the pressure drop requirement across zone 2 increases gradually to flow an increased amount of coolant through zone 2. It is worth mentioning that a more gradual reduction of pressure in the junction of zone 2 and 3 occurs while the length of zone 2 decreases and zone 3 increases as evident in the Figure 5.3 (c) and (d). Moreover, a highly intense adverse pressure gradient is evident in

Figure 5.3 (b) inside the inter-connectors. However, the intensity of the adverse pressure gradient reduces as the zone 1 length increases. This adverse pressure gradient can be attributed to the flow over the sharp edge of the inter-connectors. As the amount of secondary flow reduces gradually from case 2 to 8, the reattachment of the coolant is gradually shifting inward as shown in the Figure 5.3 (b), (c), and (d).

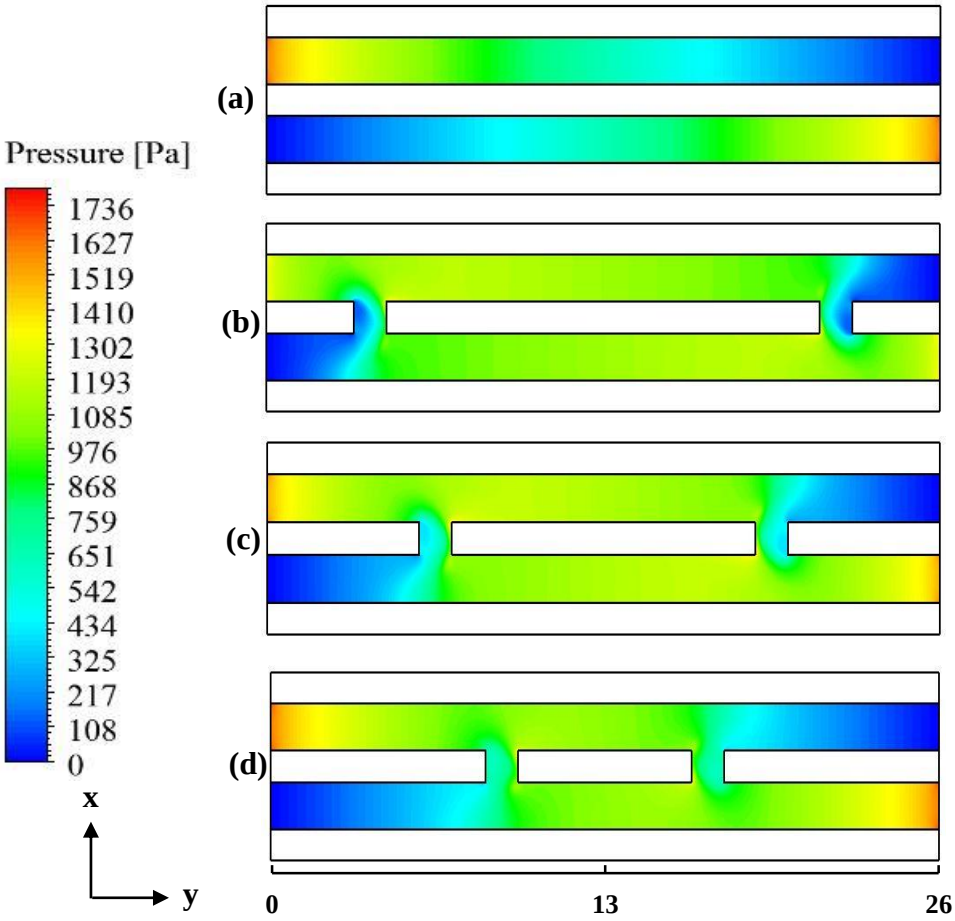

Figure 5.3 Pressure profile in center plane of the mini-channel heat sinks at $Re = 597$.

Figure 5.4 depicts the pressure distribution along the centerline of channel 1 at $Re = 597$ for all considered cases (case 0-9). In case of conventional counter flow mini-

channel heat sink (case 0), pressure reduces almost linearly along the streamwise directions as evident in the Figure 5.4. From the Figure 5.4 (a), it can be observed that for case 1-3, the magnitude of the pressure is significantly less than the case 0 in zone 1 while sudden increment in pressure is evident in the intersection region of zone 1 and 2 resulting adverse pressure gradient. Moreover, higher width of the inter-connectors allows a higher amount of secondary flow which results in less pressure magnitude (case 1 to 3) in zone 1. Afterward, a reduced amount of coolant flows through zone 2 which reduces the pressure drop requirement across this zone. Interestingly minimum pressure drop across zone 2 is evident for case 3 because of minimum coolant flow through this zone as explained earlier. On the contrary, coolant flows transversely from the second to the first channel through the second inter-connector, , therefore the coolant flow rate increases in zone 3 resulting in sudden pressure drop. Almost the same pressure distribution is evident for all other cases (case 4-9) as shown in the Figure 5.4 (b) and (c) regardless of the inter-connectors location except the pressure profile in zone 1. For cases 4-6, the pressure magnitude and pressure drop are higher across zone 1 compared to cases 1-3. This can be attributed to the increased length of zone 1 which eventually reduces the secondary flow as resultant of reduced pressure drop across the inter-connectors. Further increment of zone 1 length nullifies the effect of secondary flow on pressure drop requirement because of very negligible secondary flow as shown in the Figure 5.4.

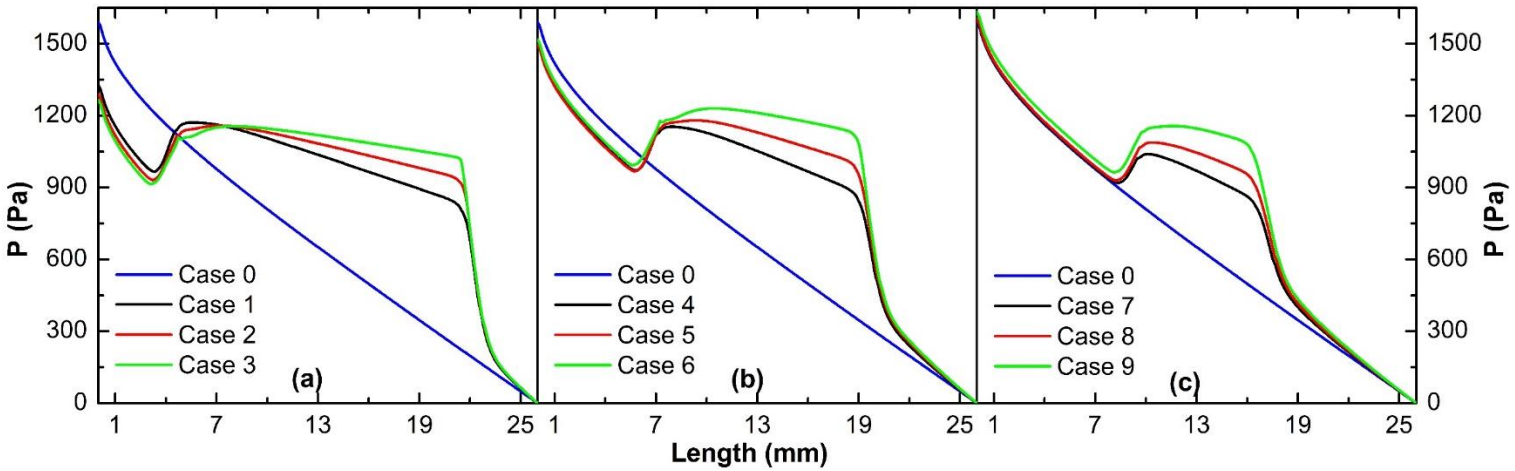

Figure 5.4 Local pressure distribution along the flow direction of channel 1 at $Re = 597$.

5.5.3 Characteristics of Velocity Distribution

Velocity distribution and streamlines for cases 0, 2, 5 and 8 along with the flow directions on the mid x-y plane (z=0.75mm) has been illustrated in Figure 5.5 at $Re = 597$. The figure shows that for case 0, velocity profile is gradually developing along the streamwise directions in both channels. From the Figure 5.5 (b), it can be observed that for the shortest length of zone 1, most of the coolant is flowing transversely through the inter-connectors because of the higher pressure difference across the inter-connectors as explained in the previous sections. Therefore the velocity magnitude in zone 2 reduced significantly which eventually results in one intense recirculation zone in the upstream of both inter-connectors as illustrated in the Figure 5.5 (b). Similar behaviors in velocity distribution are evident for case 5 and 8 except the reduction in secondary flow and intensity of the recirculation zones. These behaviors can be attributed to the gradual reduction of the pressure difference across the inter-connectors with the gradual increment of the length of zone 1 and 3 as shown in Figure 5.4 (b) and (c). Additionally, due to the sharp intersection of the main flow channels and inter-connectors, three most noticeable effects are occurring for all cases (case 2-8) such as flow separation, recirculation, and reattachment. From the Figure 5.5 (b), it can be observed that flow separation occurs at the leading edge of the inter-connectors followed by a small recirculation zone while reattachment of the coolant occurs outside of the inter-connectors. On the contrary, for case 5 and 8, the recirculation intensity increases gradually (inside the inter-connectors), and the reattachment of the secondary flow is gradually shifting inward as shown in the Figure 5.5 (c) and (d).

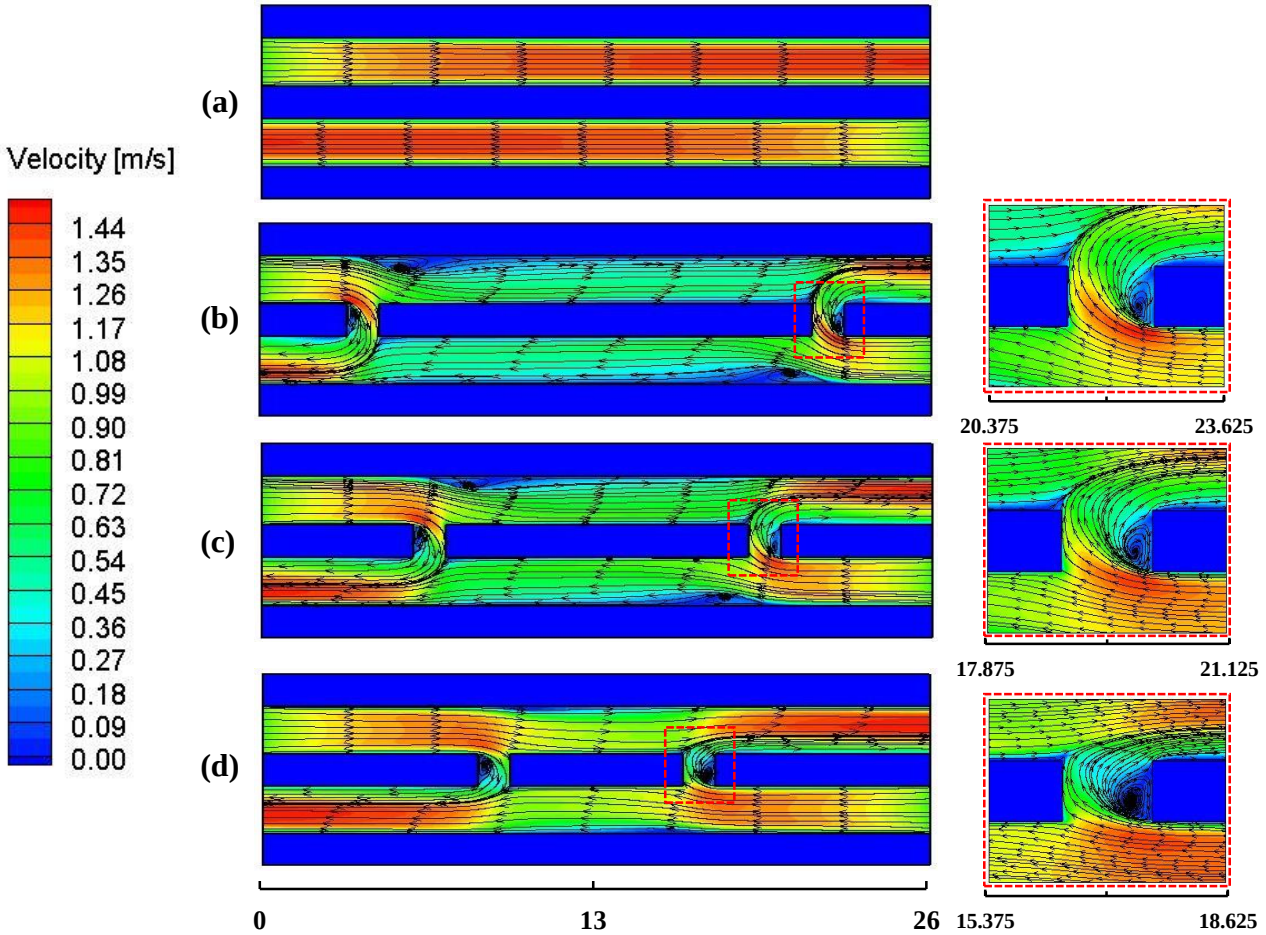

Figure 5.5 Velocity contours and streamlines in center-plane of the CMCHS at $Re = 597$.

Figure 5.6 depicts the velocity magnitude of the coolant for all considered cases (case 0-9) along the centerline of the channel 1 (z=0.75 mm) at $Re = 597$. For all inter-connected counter flow mini-channel heat sinks, the velocity magnitudes in zone 1 increase in a similar fashion as the conventional channel (case 0). However, in zone 2, a significant reduction in velocity magnitude is evident followed by an abrupt change in velocity in the junction of zone 1 and zone 2 as a resultant of secondary flow. Moreover, in case of the shortest length of zone 1 (case 1-3), the maximum reduction in velocity magnitude is evident in the Figure 5.6 compared to the intermediate and highest length of zone 1 (case 4-9). Interestingly for case 1-6, velocity magnitude is gradually increasing from the upstream to the downstream of the zone 2 while for case 7-9, velocity magnitude is gradually reducing. This can be attributed to the intense recirculation zone in the downstream of the first inter-connector as shown in Figure 5.5 (a) and (b). On the contrary, for case 7-9, less secondary flow eliminates the recirculation of the coolant in the downstream of the first inter-connector which eventually results in the higher coolant flow through zone 2. Moreover, the maximum reduction in velocity magnitude in zone 2 is evident for the higher width of the inter-connectors regardless of the inter-connectors location. It is worth mentioning that in case of the higher width of the inter-connectors, more coolant flows transversely which intensify the recirculation zone in the upstream of the inter-connectors. Afterward, the secondary flow of the coolant through the second inter-connector from channel 2 to channel 1 causes a sudden increment in velocity magnitudes in zone 3. The velocity magnitude in zone 3 is mainly governed by the reattachment characteristics of the secondary flows. At the higher width of the inter-connectors, reattachment of the coolant occurs over the outer channel wall while reattachment points

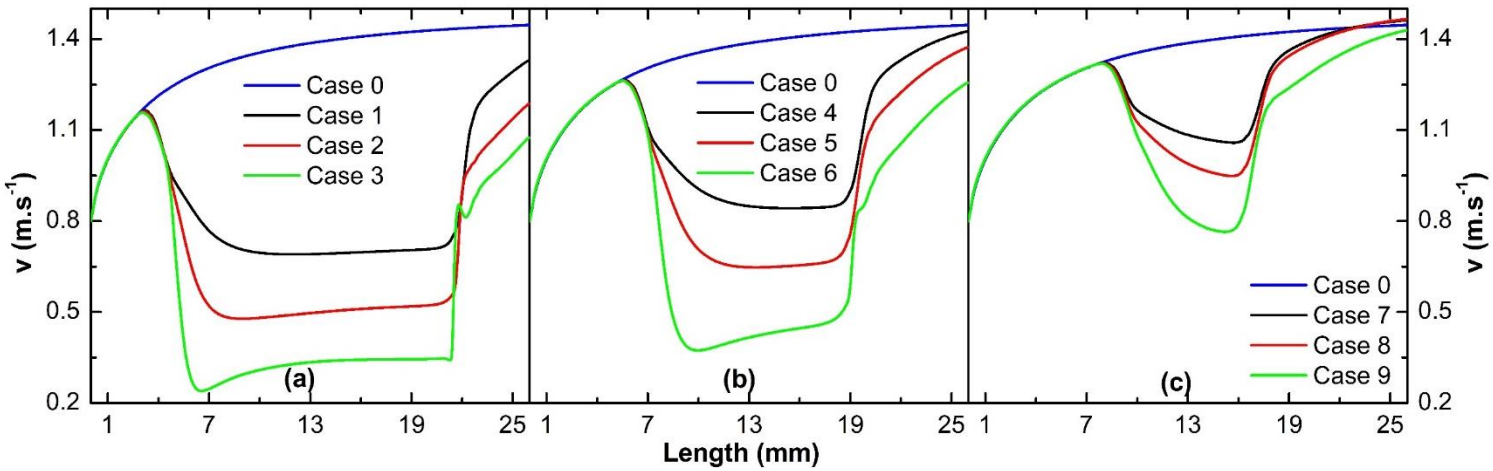

Figure 5.6 Local velocity distribution along the flow direction of channel 1at $Re = 597$.

shift gradually inward at the lower width of the inter-connectors. Therefore, at lower width of the inter-connectors, centerline velocity in zone 3 is higher with respect to the higher width of the inter-connectors for all considered cases as evident in the Figure 5.6.

5.5.4 Characteristics of Friction Factor

The variation of friction factor, f and friction factor ratio, f/f_0 as a function of Re is illustrated in Figure 5.7 and Figure 5.8 for all considered cases (case 0-9). For cases 1-9, f is mainly triggered by three key parameters such as secondary flow amount, breaking and re-initialization of the hydraulic boundary layer at the junction of the inter-connectors and main flow channels, and also the intensity of the generated recirculation zones. At low Re, a substantial amount of secondary flow reduces the coolant flow rate in zone 2 resulting in a substantial reduction in pressure drop requirement across this zone and consequently reduces the overall pressure drop requirement. Since the percentage of secondary flow reduces as the length of zone 1 and 3 increases, the pressure drop across the zone 2 increases. Therefore, the magnitude of the overall f increases compared to the short length of zone 1 and 3. Moreover, the maximum f reduction is evident for the higher inter-connectors width (case 3, 6, 9) at any particular inter-connector location. This is because of the less coolant flow through zone 2 as a resultant of higher secondary flow as explained in the previous section. For example, for case 1, 4, and 7, a maximum ~40.26%, ~24.95%, and ~11.28% reduction in f occurs at $Re = 150$ compared to case 0 whereas for case 3, 6, and 9, a maximum ~48.37%, ~31.13%, and ~15.00% reduction in f occurs at the same Re. However, at higher Re and lower width of the inter-connectors, for all inter-connected counter flow mini-channel heat sinks (case 1-9), the f value become comparable to the case 0 as shown in the Figure 5.7. This can be attributed to the reduced secondary flow at

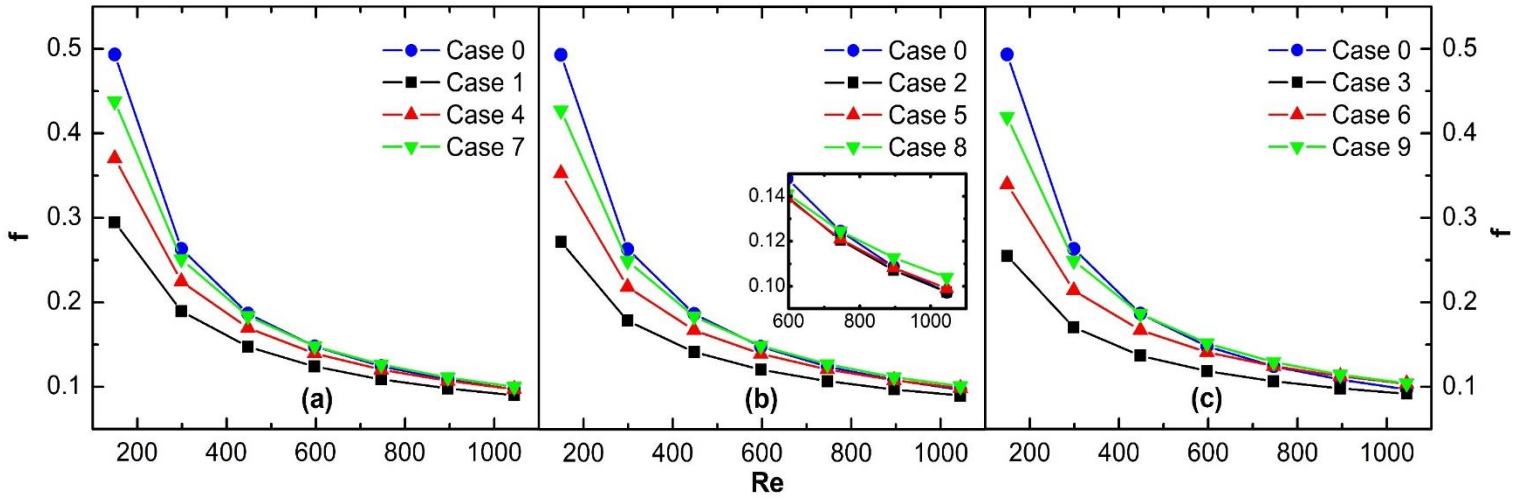

Figure 5.7 Overall f versus Re.

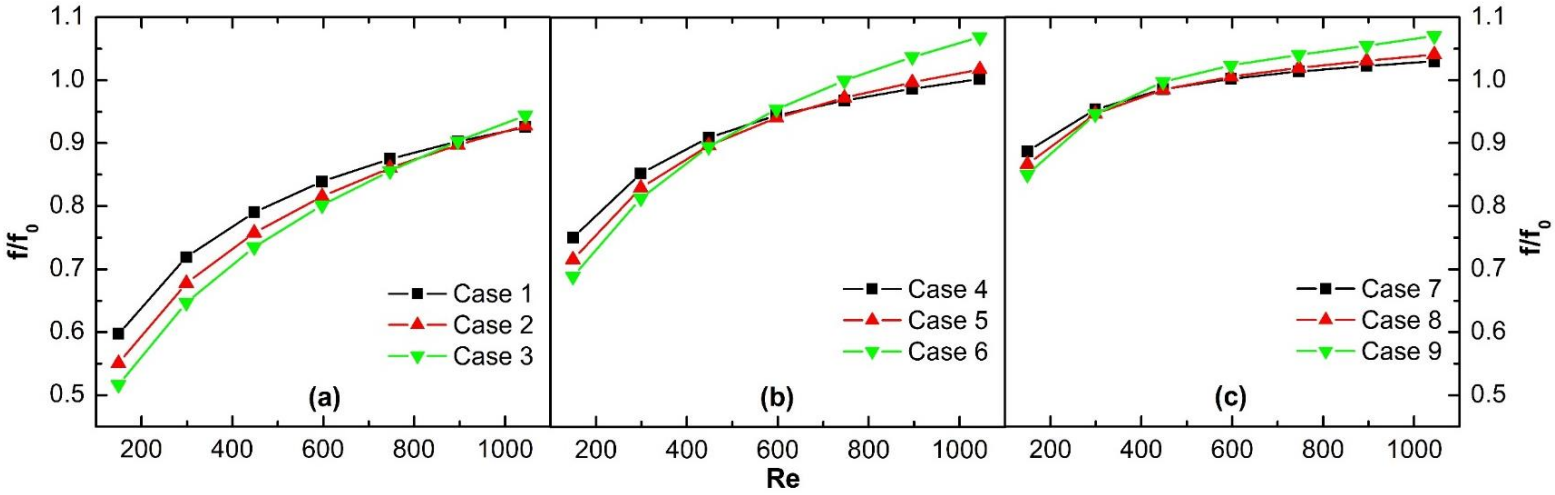

Figure 5.8 Overall f/f_o versus Re.

higher Re as evident in the Figure 5.2. For example, for case 1, f reduced by only ~7.48% at $Re = 1044$ whereas for case 4, and 7, f increased by ~0.22% and ~3% respectively compared to case 0. However, for higher width of the inter-connectors especially for cases 5, 6, 8, and 9 and at higher Re, higher secondary flow results in an extra intense recirculation zone in the downstream of the inter-connectors in the main channel flow path. Therefore, f increases significantly compared to case 0. For example, for case 5, 6, 8, and 9, f enhanced by ~1.77%, 6.88%, 4.10%, and 7.0% respectively compared to case 0. Additionally, regardless of inter-connectors location and width, f/f_o increases gradually with a positive reducing slope as depicted in the Figure 5.8.

5.5.5 Characteristics of Temperature Distributions

Temperature contours for cases 0, 2, 5 and 8 on bottom-plane of the channel (x-y plane) at z=0.50 mm has been illustrated in Figure 5.9 at $Re = 597$. For case 0, thermal boundary layer is growing gradually along the opposite flow direction in the adjacent channels, therefore, highest thermal resistance imposes in the middle of the heat sink resulting in higher temperature in this region as evident in the Figure 5.9 (a). However, in case of inter-connected counter flow mini-channel heat sinks, surface temperature distribution is mainly triggered by two parameters such as (i) boundary layer disruption and redevelopment, and (ii) coolant flow rate through zone 2. For the shortest length of zone 1 and 3 (case 2), higher secondary flow results in higher disruption and re-initialization of thermal boundary layers. However higher secondary flow reduces the coolant flow rate in zone 2, which affects the thermal profile adversely and results in higher surface temperature in zone 2 as shown in the Figure 5.9 (b). On the contrary, for case 5,

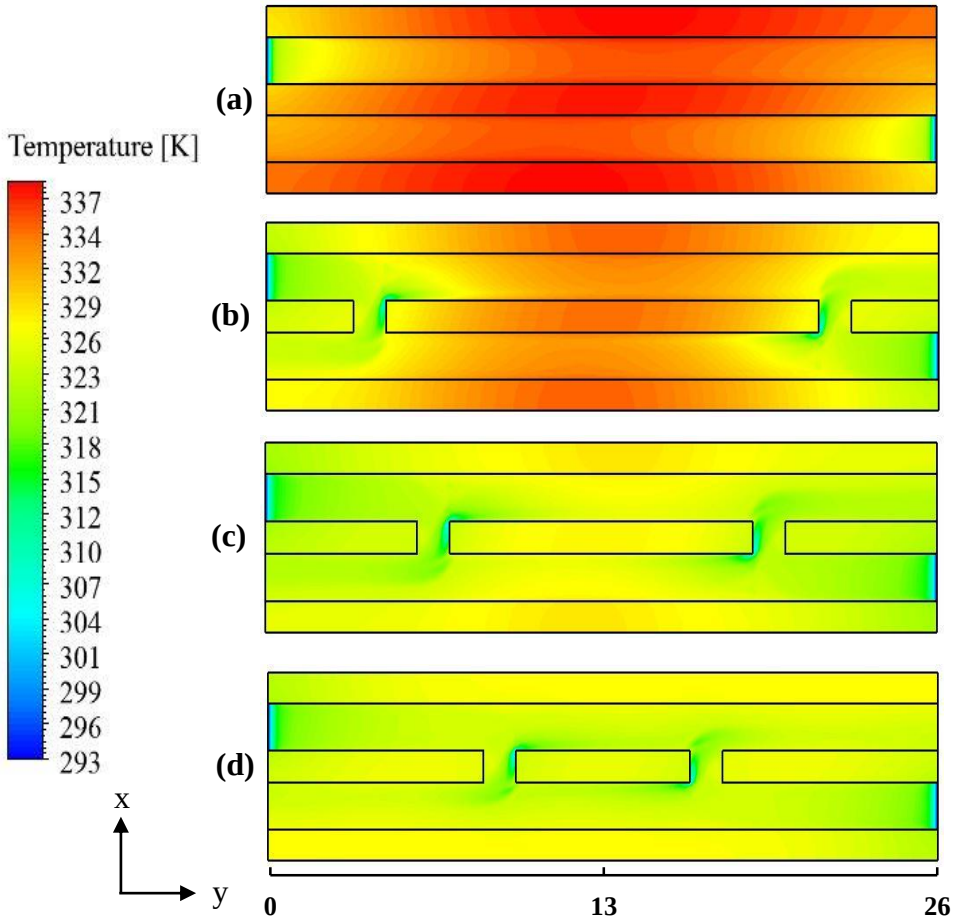

Figure 5.9 Temperature profile of bottom surface (z=H_s) of the mini-channel heat sinks at $Re = 597$.

less amount of secondary flow comapred to case 2 resulting in a moderate amount of coolant flows through the zone 2. As a resultant of these two favorable effects, a significant reduction in surface temperature is evident in the Figure 5.9 (c). However, in case of the highest length of zone 1 and zone 3 (case 8), the amount of secondary flow reduced significantly because of less pressure difference across the inter-connectors. Therefore, the breaking of the thermal boundary layer reduces which affects the heat dissipation adversely while the flow through zone 2 increases which is favorable for heat transfer. As a resultant

of these two opposite effects, slight increment in overall surface temperature is evident for case 8 compared to case 5 as shown in the Figure 5.9 (d).

Figure 5.10 illustrate the centerline temperature of the inter-connected counter flow mini-channel heat sink base (z=0) at $Re = 597$ for all considered cases (case 1-9) along with the conventional counter flow mini-channel heat sink (case 0). For all inter-connected counter flow mini-channel heat sinks, temperature reduces significantly especially in zone 1 and 3 because of the disruption and re-development of the thermal boundary layer. From the Figure 5.10 (a), it can be observed that for cases 1-3, surface temperature is gradually increasing from the inlet to the first inter-connector while in the downstream of the inter-connector, a higher positive temperature gradient occurs and afterward, surface temperature reaches its pick value. Since most of the incoming coolant flows transversely which reduces the coolant flow rate in zone 2 and also creates an intense recirculation zone in the downstream of the inter-connectors, significant increment in surface temperature is evident in zone 2. However, higher inter-connectors width results in higher secondary flow which eventually reduce the coolant velocity in zone 2 and increase the heat sink temperature as evident in the Figure 5.10 (a). On the contrary, for case 4-6, a moderate amount of secondary flow and less intense recirculation zone in the downstream of the inter-connectors enhance the coolant flow rate through zone 2 which results in a slight negative temperature gradient in the upstream of the first inter-connector and also less overall surface temperature compared to case 1-3. From the Figure 5.10 (b), it can be observed that higher inter-connectors width provides minimum overall temperature (case 6). This is because of the higher disruption of the thermal boundary layer as a resultant of the moderate amount of secondary flow. Moreover, for cases 7-9, a significantly higher

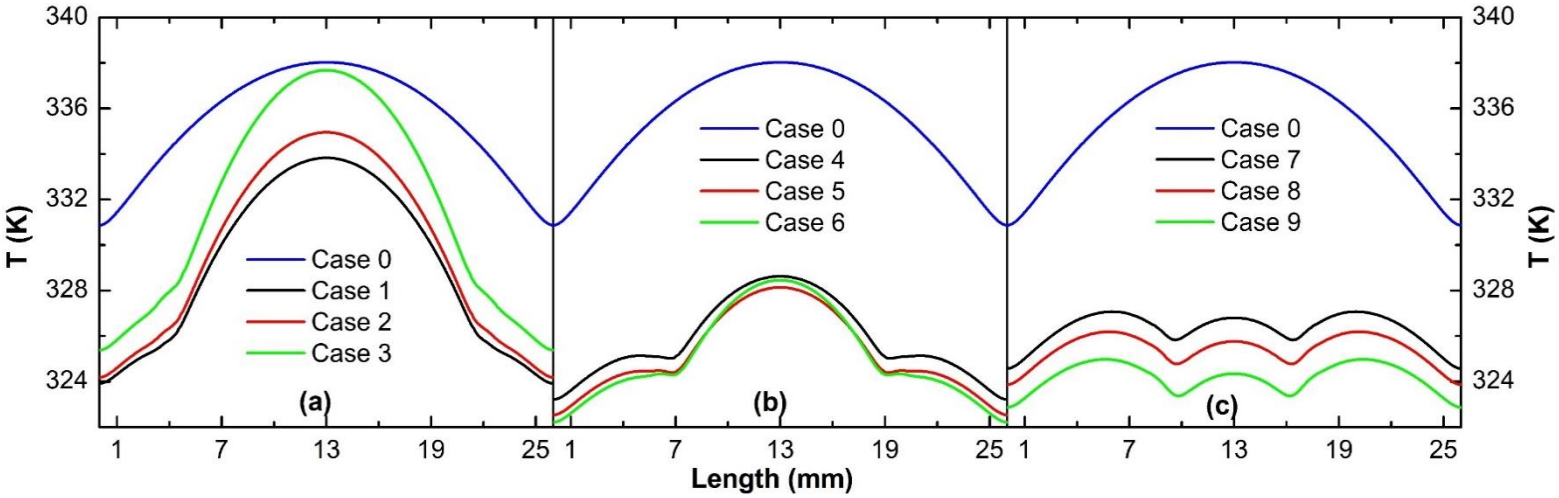

Figure 5.10 Local temperature distribution along the center line of the mini-channel base at $Re = 597$.

negative temperature gradient is evident in the Figure 5.10 (c) in the upstream of the first inter-connector because of significantly reduced secodary flow and almost no recirculation of the coolant in the downstream of the inter-connectors. Additionally, as s resultant of the higher secondary flow and higher disruption of the thermal boundary layer, minimum overall surface temperature has been observed for case 9. From the Figure 5.10, it can also be seen that case 7-9 provide most uniform temperature distribution compared to the all other cases.

5.5.6 Heat Transfer Characteristics

Figure 5.11 and Figure 5.12 depict the variation of Nusselt number, (Nu) and Nusselt number ratio, (Nu/Nu_o) as a function of Re for all cases (case 0-9). It is worth mentioning that a higher percentage of secondary flow occurs in case of the smallest length of zone 1 and zone 3 (case 1-3) and especially at lower Re as explained earlier. Therefore, at low Re, coolant flow reduced significantly in the downstream of the inter-connectors. Additionally, a thicker thermal boundary layer reduces the disruption of the boundary layer by the transverse flow at low Re which results in lower Nu as shown in the Figure 5.11 (a). This phenomenon increases with the increment of the inter-connectors width. For example, at $Re = 150$, Nu reduced by ~7.34% for case 1 while for case 3, Nu reduced by ~20% compared to case 0 as shown in the Figure 5.12 (a). However, at higher Re and lower inter-connectors width, the breakup of the thinner thermal boundary layer is significantly higher despite of the reduced amount of secondary flow. Furthermore, at higher inter-connectors width, the reduction of coolant velocity in the zone 2 is more significant compared to the effect of the boundary layer breakup resulting higher surface temperature and lower Nu compared to smaller inter-connectors width as shown in the Figure 5.11 (a).

For example, at $Re = 1044$, Nu increased by ~24% and ~17% for case 1 and 3 respectively. On the contrary, for an intermediate length of zone 1 and 3 (case 4-6), two opposite thermal behaviors are evident in the Figure 5.11 (b) across a range of transitional Re range ($350 < Re < 600$). At lower Re (< 350), thermal performance changes in a descending order from the lower to the higher inter-connectors width (case 4-6), while at higher Re (> 600), thermal performance changes in an ascending order from the lower to the higher inter-connectors width. These behaviors can be explained by the combined effect of the boundary layer disruption and the reduction of coolant velocity in zone 2. At low Re and higher inter-connectors width, high secondary flow and less disruption of the thicker thermal boundary layer resulting in smaller Nu. However, at higher Re, higher disruption of the thinner boundary layer is evident at higher inter-connectors width which provides higher Nu despite of less secondary transverse. For example, at $Re = 150$, a maximum ~8% increment in Nu is recorded for lowest inter-connectors width (case 4), while at $Re = 1044$, a maximum ~45% increment in Nu is noted for highest inter-connectors width (case 6). A similar trend in heat transfer behavior is evident for the highest length of zone 1 and 3 (case 7-9) except the higher Nu value at lower Re and also the lower transitional Re range ($190 < Re < 260$) as evident in the Figure 5.11 (c). Moreover, from the Figure 5.11 (c) and Figure 5.12 (c), it can also be observed that at low Re (< 300), the inter-connectors width has a minor effect on Nu because of the less secondary flow and moderate coolant velocity in zone 2 as explained in Figure 5.5 and Figure 5.6. For example, at $Re = 150$, ~17%, 15%, and 13% increment in Nu is evident for case 7, 8, 9 respectively. On the contrary, at higher Re, maximum width of the inter-connectors provides better thermal performance through the optimum breaking of the thermal boundary layer and maintaining

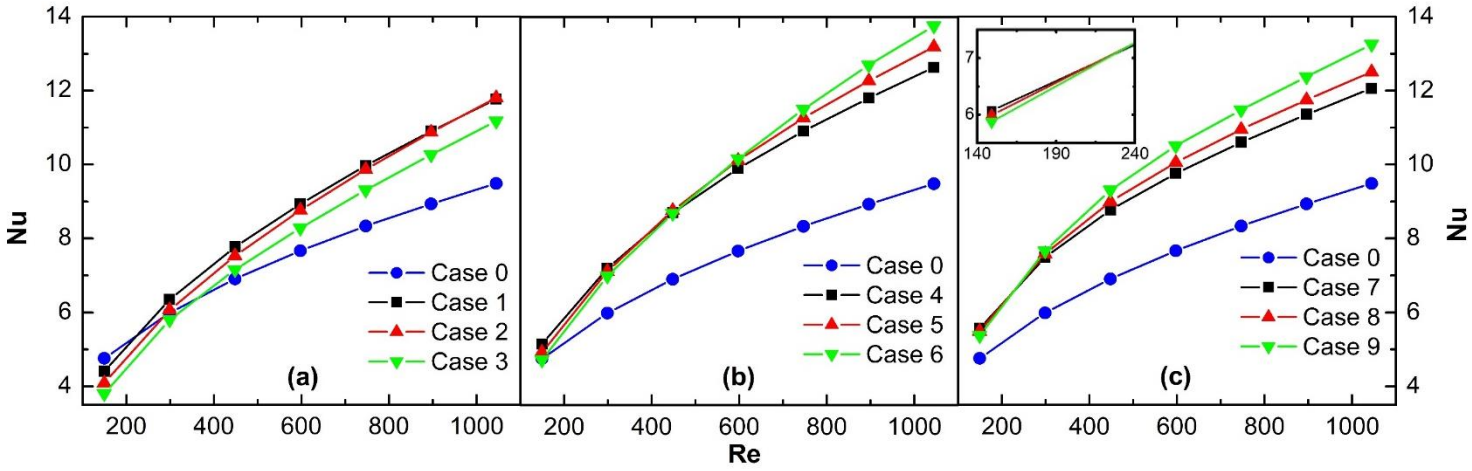

Figure 5.11 Overall Nu versus Re.

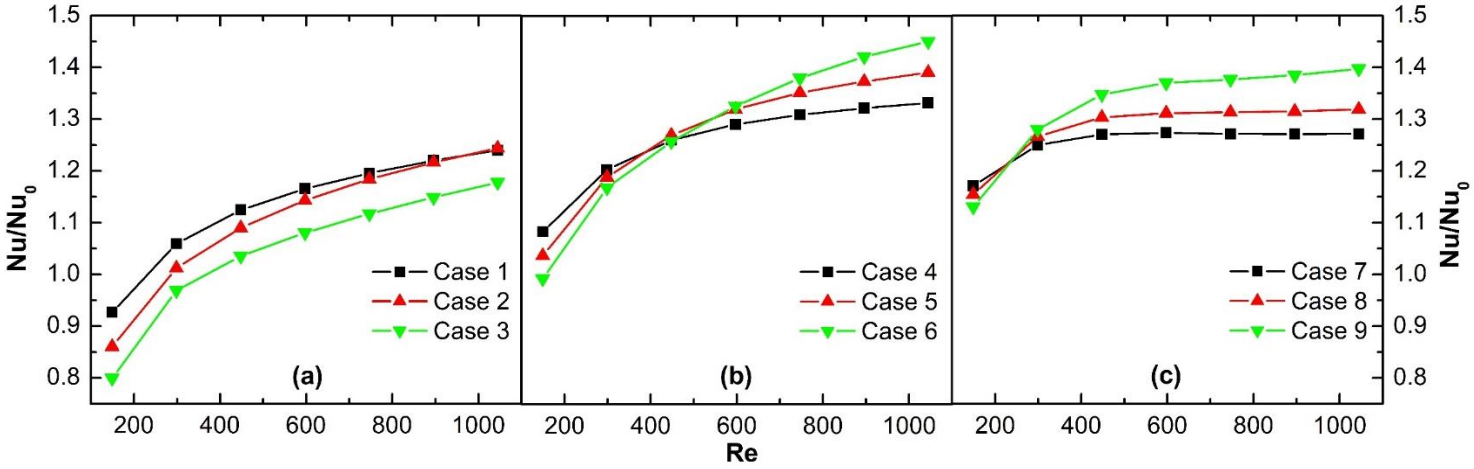

Figure 5.12 Overall Nu/Nu_o versus Re.

moderate coolant flow through zone 2. For example, a maximum ~39.50% increment in Nu is evident for case 9 at $Re = 1044$. Interestingly, from the Figure 5.12 (c), It can be seen that the for case 7 and 8, Nu/Nu_o reach to a case-specific constant value (±1.2%) for a wide range of Re value ($448 \leq Re \leq 1044$).

5.5.7 Characteristics of Thermal Resistance and Pumping power

To characterize the overall thermal-hydraulic performance of the inter-connected counter flow mini-channel heat sinks (case 1-9) compared to the case 0, overall thermal resistance (R_{th}) as a function of pumping power (P_p) are plotted in Figure 5.13. Since conductive thermal resistance, R_{cond} is mainly dependent on the geometrical dimension of the heat sink, R_{th} is mostly controlled by R_{conv} and R_{cap} which are primarily depends on P_p. From the Figure 5.13, it can be observed that for inter-connected counter flow mini-channel heat sinks, R_{th} reduces significantly at any particular P_p especially at higher P_p regardless of the inter-connectors location and width indicates a reduction of R_{comv} and R_{cap}. Since for cases 1-3 and at low Re, ~70-85% of the incoming coolant flows transversely through the inter-connectors, therefore P_p reduced significantly compared to case 0. On the contrary, surface temperature increases in zone 2 which results in higher R_{th} and this phenomenon increases with the inter-connectors width as evident in the Figure 5.13 (a). For example, at $Re = 150$ and for case 3, P_p reduced by ~48% while R_{th} increased by ~19% compared to case 0. However, both the R_{th} and required P_p reduced substantially at higher Re because of the less secondary flow and also thinner boundary layer as shown in the Figure 5.13 (a). Moreover, for the intermediate length of zone 2 (case 4-6), at low Re, smaller inter-connectors width provides minimum R_{th} whereas at higher

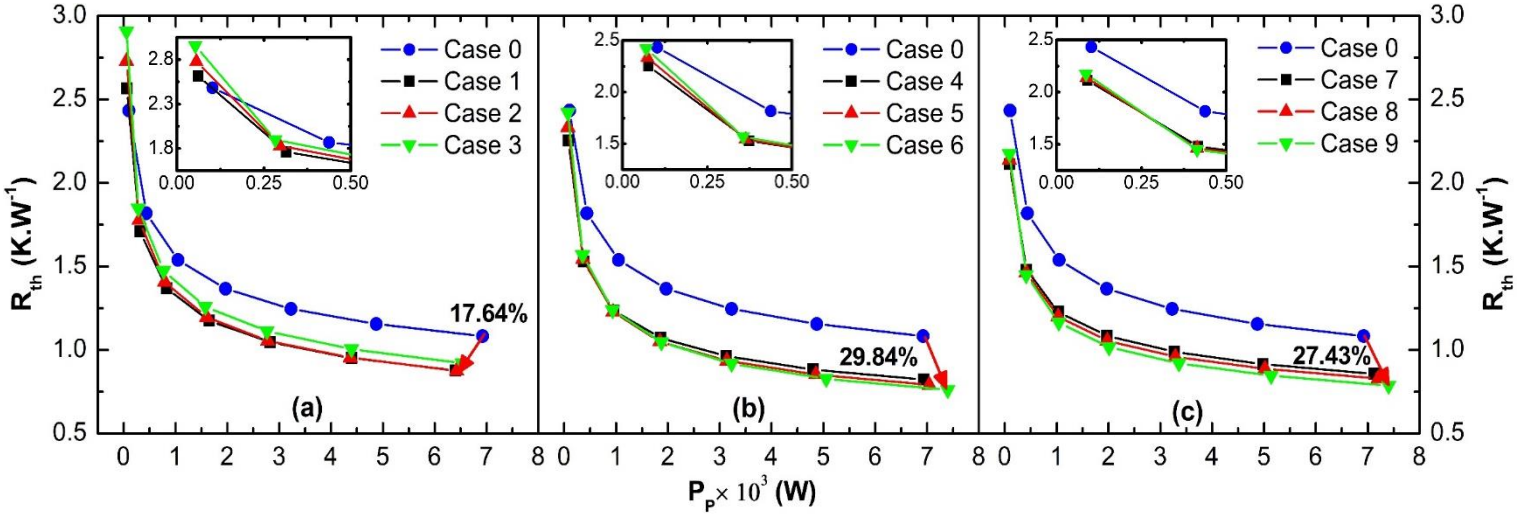

Figure 5.13 Thermal resistance versus pumping power.

Re, higher inter-connectors width provides lower R_{th} with a penalty of relatively higher P_p. It is worth mentioning that for case 4-6, a moderate amount of secondary flow helps to maintain a balance between boundary layer disruption and surface temperature distribution in zone 2 resulting minimum R_{th} at higher Re with a cost of minimal increment of the P_p (~7%) as seen in the Figure 5.13 (b). Similar R_{th} and P_p behaviors have been evident for case 7-9 except higher R_{th} and P_p requirement compared to case 4-6 because of minimal secondary flow as shown in the Figure 5.13 (c).

5.5.8 Characteristics of Entropy Generation Rate

Figure 5.14 depicts the variation of entropy generation rate (S) as a function of Re for all considered cases (case 0-9). Since the magnitude of the thermal entropy generation rate (S_{th}) is significantly higher than the frictional entropy generation rate (S_{fr}), the overall entropy generation rate (S) is mainly determined by the S_{th}. In order to get a deep insight of the variation of S with Re and also the dependency of S_{th} on Nu, the equation of S_{th} can be rewrite as following form:

$$S_{th} = Q\left(\frac{1}{T_{in}} - \frac{1}{T_{in}+QD_h(C_1+C_2)}\right) \tag{5.2}$$

Where, $C_1 = \frac{1}{A_{int}NuK_f}$ and $C_2 = \frac{1}{Re\mu_f A_c C_{p,f}}$

From the above equations, it can be seen that S_{th} decreases as Nu and Re increases. Additionally, Nu increases gradually as Re increase. Therefore, for all considered cases, S_{th} i.e, S gradually decreases with the increment of Re. From the Figure 5.14, it can be seen that cases 1-3 show higher entropy generation rate compared to cases 4-9. It is worth mentioning that for the shortest length of zone 1 and 3 (case 1-3) and at low Re, Nu reduces

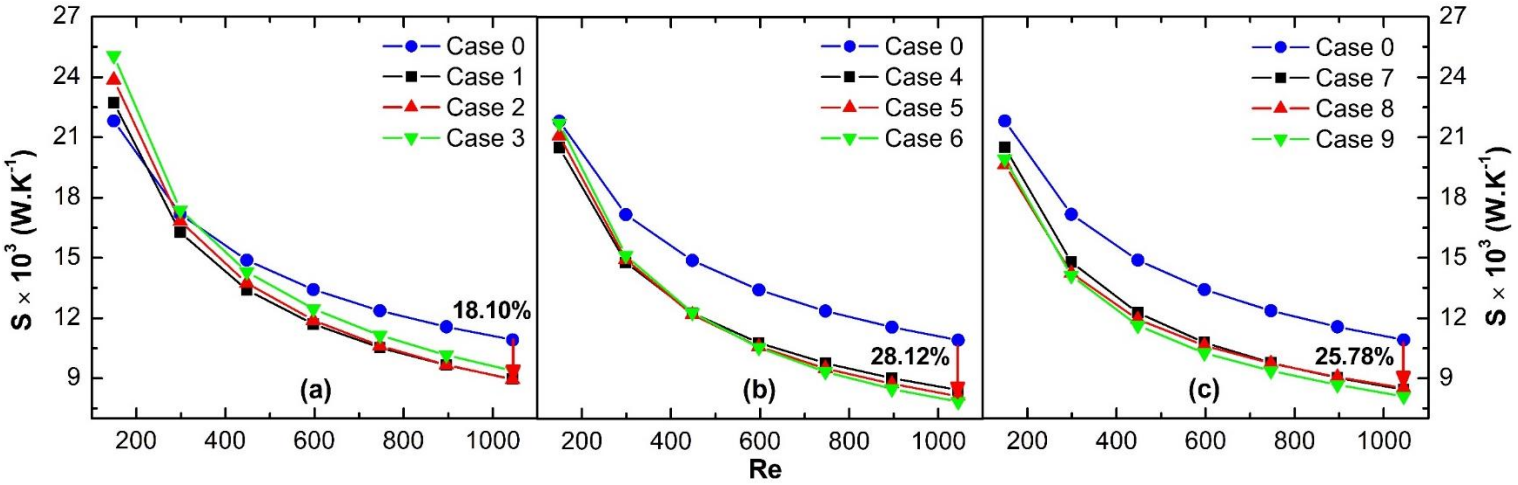

Figure 5.14 Entropy generation rate versus Re.

significantly compared to case 0 as explained in Figure 5.11and Figure 5.12 which eventually leads to the increment of S as shown in the Figure 5.14 (a). Additionally, the reduction of the Nu and increment of S becomes prominent with the increment of the inter-connectors width. For example, at $Re = 150$, S increased by ~4.14% for case 1 while for case 3, S increased by ~14.82% compared to case 0. On the contrary, at higher Re, enhanced Nu results in a significant reduction of S compared to case 0 as shown in the Figure 5.14 (a) and a maximum ~18.10% reduction of S is evident for case 2 at Re=1044. Since for cases 4-6, the ratio of Nu changes in an ascending order from the higher to the lower inter-connectors width at low Re, the magnitude of S changes in the descending order from the higher to the lower inter-connectors width as shown in the Figure 5.14 (b). At higher Re, the significant increment of Nu leads to a substantial reduction of S and this phenomenon increases as inter-connectors width increase. For example, at $Re = 1044$, a maximum ~28.12% reduction of S is evident for case 6. However, for the highest length of zone 1 and 3 (case 7-9), highest inter-connectors width provides less S as evident in the Figure 5.14 (c) for all considered Re except $Re = 150$. At $Re = 1044$, S is reduced by ~25.78% for case 9 while at $Re = 150$, a maximum ~10% reduction in S is evident for case 8.

5.5.9 Performance Evaluation Criteria (PEC)

PEC for all inter-connected counter flow mini-channel heat sinks (case 1-9) is presented in Figure 5.15 as a function of Re. From the Figure 5.8 and Figure 5.12, it can be seen that the ratio of f and Nu increases gradually with a decreasing positive slope. Therefore, PEC values follow the same trend especially for case 1-6. In case of the shortest length of zone 1 and 3 (case 1-3) and at low Re, Nu reduces compared to case 0 regardless

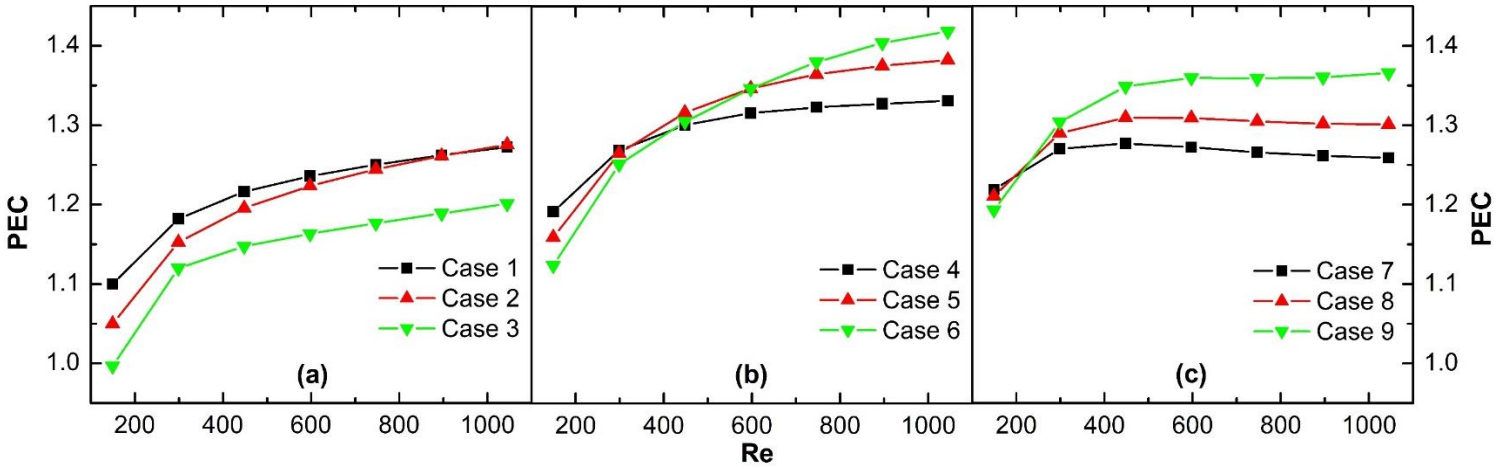

Figure 5.15 PEC vs. Re.

of the inter-connectors width as evident in Figure 5.12 (a), but at the same time, f reduced dramatically as explained in Figure 5.8 (a) resulting in PEC value greater than 1. Moreover, the smallest inter-connectors width (case 1) provides better heat transfer performance among case 1-3 for all Re range results in higher PEC value compared to case 2 and 3 as shown in the Figure 5.15 (a). For example, case 1 provides PEC value of 1.10 and 1.27 respectively at $Re = 150$, and 1044. In case of the intermediate and highest length of zone 1 and 3 (case 4-9), the ratio of Nu and f changes in descending order from the smaller to the higher inter-connectors width before transitional Re range whereas the ratio of Nu and f changes in ascending order from the smaller to the higher inter-connectors width after transitional Re as shown in the Figure 5.12 and Figure 5.8. Therefore, for cases 4-9 and at lower Re, lower inter-connectors width provides better PEC value while at high Re, higher inter-connectors width provides better PEC value. For example, at $Re = 150$, maximum PEC value of ~1.19 and ~1.22 are achieved for case 4 and 7, while at $Re = 1044$, maximum PEC value are reached to ~1.42 and ~1.37 for case 6 and 9. Furthermore, for case 7-9, the ratio of Nu reaches to a constant value while the ratio of f increases gradually as explained earlier, which leads to a slight reduction in PEC at higher Re as shown in the Figure 5.15 (c).

5.6 Summary

The effects of inter-connectors location and width on the overall performance of counter flow mini-channel heat sink were examined numerically and compared with the overall performance of the conventional counter flow mini-channel heat sink under laminar flow regime ($Re = 150 - 1044$). Two inter-connectors were placed along the flow direction to generate secondary flow between the two adjacent channels. Three different

locations and for each location, three different inter-connectors widths (case 1-9) were chosen for the numerical modeling. The following conclusions can be drawn based on the numerical analysis:

1. The amount of secondary flow reduced gradually with the Re regardless of the inter-connectors location and width. Moreover, the amount of the secondary flow changed in descending order from the smaller to the higher length of zone 1 and zone 3, and in ascending order from the lower to the higher width of the inter-connectors.

2. For all inter-connected counter flow mini-channel heat sinks, friction factors (f) reduced significantly at lower Re compared to the conventional counter flow mini-channel heat sink (case 0) because of higher secondary flow, whereas at higher Re, f became very comparable to case 0. This phenomenon increases with the inter-connectors width and decreases with the reduction of the length of zone 1 and 3. Maximum ~48.37% reduction in f was recorded for case 3 at $Re = 150$ compared to case 0 while a maximum ~7.0% enhancement in f was recorded for case 9 and at $Re = 1044$.

3. The inter-connected counter flow mini-channel heat sinks showed improved overall thermal performance compared to the conventional counter flow mini-channel heat sink, especially at higher Re. However, in cases of the smaller and intermediate length of zone 1 and 3 (case 1-6) and at low Re, the inter-connectors affect the Nu adversely. At $Re = 1044$, maximum ~45.0%

enhancement in Nu is detected for case 6 whereas for case 3 and at $Re = 150$, Nu reduced by ~20% compared to case 0.

4. Inter-connectors location and width have a substantial effect on the thermal performance of the counter flow mini-channel heat sinks. For the smallest length of zone 1 and 3 (case 1-3), the lowest inter-connectors width provides better thermal performance. On the contrary, for the intermediate and highest length of zone 1 and 3 (case 4-9) and at low Re, the lowest inter-connectors width gives better heat transfer performance while at higher Re, the highest inter-connectors width depicts better heat transfer performance.

5. For all inter-connected counter flow mini-channel heat sinks, a significant reduction in thermal resistance was recorded for any particular pumping power except for case 1-3 and $Re = 150$. A maximum ~48% reduction in pumping power was recorded for case 3 compared to case 0 while a maximum ~29.48% reduction in thermal resistance was evident for case 6.

6. At low Re, PEC value changed in descending order from the lower to the higher width of the inter-connectors regardless of the inter-connectors location. However, at higher Re, higher PEC value was achieved for the higher width of the inter-connectors. At $Re = 150$, a maximum PEC value of ~1.22 was recorded for case 7, and at $Re = 1044$, a maximum PEC value of ~1.42 was recorded for case 6.

CHAPTER 6 EXPERIMENTAL STUDY OF THERMAL-HYDRAULIC PERFORMANCE OF PARALLEL AND COUNTER FLOW MINI-CHANNEL HEAT SINKS EQUIPPED WITH SECONDARY CHANNELS

6.1 Inroduction

Numerical study showed that, highest inter-connectors width (1.50 mm) and highest inter-connectors distance from the inlet and outlet of the heat sink (9 mm) provided best thermal-hydraulic performance at low Re ($Re \leq 750$) among all other consided mini-channel heat sinks while highest inter-connectors width (1.50 mm) and intermediate inter-connectors distance from the inlet and outlet of the heat sink (6 mm) provided best thermal-hydraulic performance at higher Re ($Re \geq 750$). Moreover, in practical application, mini-channel heat sinks is being used for low Re because of high pumping power penalty at higher Re. Therfore, highest inter-connectors width (1.50 mm) and highest inter-connectors distance from the inlet and outlet of the heat sink (9 mm) was chosen as the inter-connectors dimensions for experimental analysis. A inter-connected mini-channel heat sink has been fabricated based on the above stated inter-connectors dimensions. Additionaly, a corresponding conventional mini-channel heat sink has also been fabricated as the base case in contrast to the newly inter-connected mini-channel heat sink. An experimental set-up has been designed and built to experimentally quantify the effect of inter-connectors on the thermal-hydualic performance of the parallel and counter flow mini-channel heat sinks for a Re range of 110-480. In the present chapter, the detail of test

section fabrication, test section assembly, coolant flow loop, and the experimental procedure of the test facilities are discussed. In this chapter, experimental results are also compared with the corresponding numerical predictions.

6.2 Design of Mini-Channel Heat Sink and Fabrication

6.2.1 Conventional Mini-Channel Heat Sink

For the experimental work, first, a conventional straight fin mini-channel heat sink has been designed and fabricated from oxygen free copper block by using CNC micro-milling machine. Figure 6.1 shows the schematic of the conventional mini-channel heat sinks.

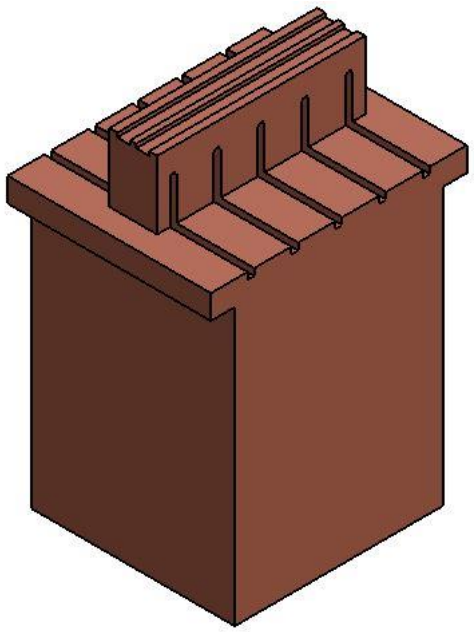

Figure 6.1 Schematic of the conventional mini-channel heat sink.

The mini-channel heat sink has two segments such as (1) top mini-channel segment and (2) bottom base segment as evident in Figure 6.1. Below is the detail description of both segments:

(1) Top Mini-channel Segment

Top mini-channel segment has a footprint of $26mm \times 6mm$ $(L_t \times W_t)$ and consists of two channels separated by a sold cooper wall, as shown in Figure 6.2. Each mini-channel has a depth (H) of $0.50\ mm$, width (W) of $1.50\ mm$, and a length (L) of $26\ mm$ which provide a hydraulic diameter of $750\ \mu m$. Both side walls and middle wall has a constant thickness of $1\ mm$. In order to measure the local surface temperature distributions of both channels, five holes for five thermocouples for each channel (total 10 thermocouples hole) along stream wise position of $2, 7.50, 13, 18.50, and\ 24\ mm$ from channels inlet were drilled. All thermocouple holes were drilled at 2.1 mm below from the bottom surface of the mini-channels. In-total ten K-type thermocouples were inserted into the holes to measure the wall temperature. Detail drawing of the mini-channel heat sink has been provided in Appendix B.

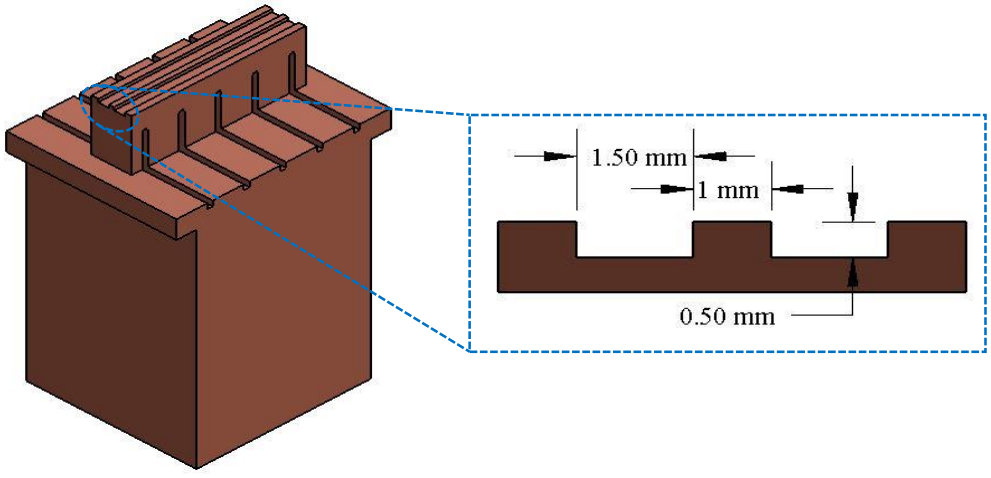

Figure 6.2 Geometrical dimensions of the mini-channel heat sink.

(2) Bottom Base Segment

Bottom base segment has a footprint of $26mm \times 6mm \times 15mm$, while the extended geometry has a footprint of $32\ mm \times 12\ mm \times 20mm$. Bottom base segment

has also five slots of 0.85 mm depth on each side to accommodate ten thermocouples wire. Moreover, four symmetric holes of 6.35 mm diameter and 28.50 mm length were drilled from the bottom surface of the heat sink substrate to insert four cartridge heaters. Detail drawing of the bottom base segment has been provided in Appendix B.

6.2.2 Inter-Connected Mini-Channel Heat Sink

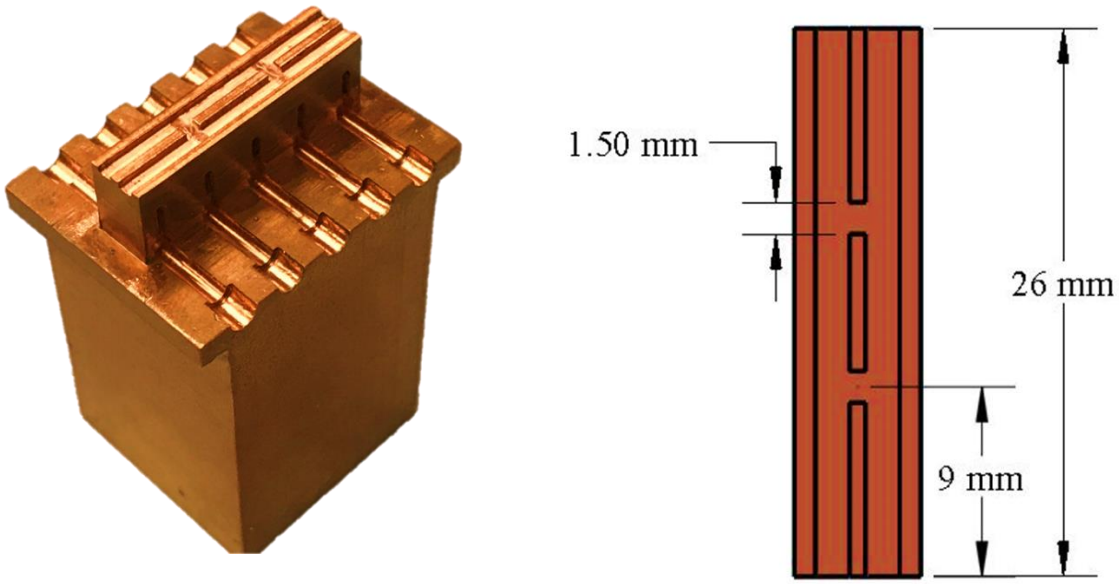

Figure 6.3 (a) Inter-connected mini-channel heat sink, (b) top view of the inter-connected mini-channel heat sink.

Inter-connected mini-channel heat sink has identical dimensions for both top mini-channel and base segments as the conventional mini-channel heat sink except inter-connectors. Figure 6.3 shows the fabricated inter-connected mini-channel heat sink. To enable secondary flow between two adjacent channels, two inter-connectors were fabricated at a distance of 9 mm from the both end of the heat sink as shown in Figure

6.3(b). Additionally, both inter-connectors have same width and height ($1.50\,mm \times 0.50\,mm$) as the mini-channels.

6.3 Experimental Setup

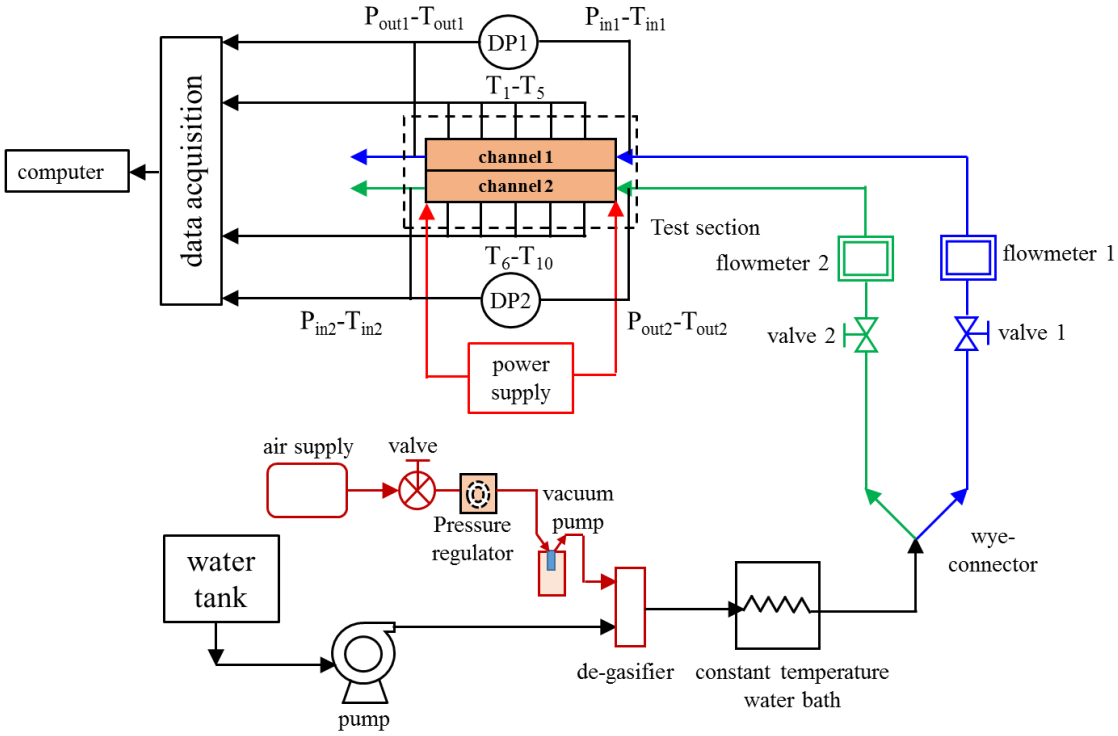

Figure 6.4 Experimental setup for parallel flow mini-channel heat sink.

Designing a mini-channel cooling system requires a comprehensive systematic methodology with a high degree of accuracy due to several influential parameters on its performance. Therefore, in the present study, an integrated open loop system was designed and built with a high degree of flexibility to perform experiments of parallel and counter flow mini-channel heat sinks at different operating conditions. The experimental setup provides the opportunity to vary the flow direction, coolant flow rate, coolant inlet temperature, and input heat flux. Figure 6.4 and Figure 6.5 show a schematic diagram of

the experimental setup for the parallel and counter flow mini-channel heat sink. The system consists of five main components: a flow loop, a degasification system, a test section, a power supply system, and a data acquisition system. Below is a brief description of the main parts of the experimental system.

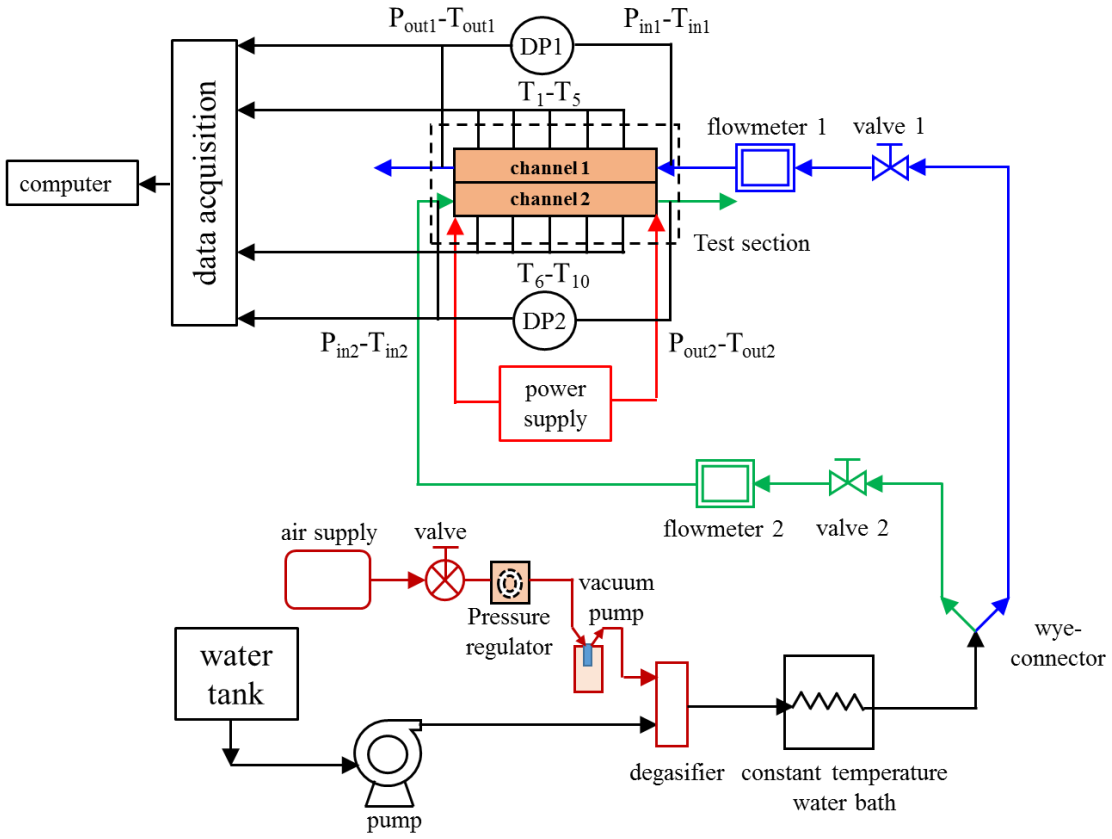

Figure 6.5 Experimental setup for counter flow mini-channel heat sink

6.3.1 Flow Loop

Figure 6.6 and Figure 6.7 shows the schematic diagram of the flow loop of the experimental facilities for the parallel and counter flow mini-channel heat sinks respecytively. A gear pump (Ismatec Reglo-z Digital) was used to supply a constant flow rate through the flow loop from the reservoir. Afterward, the coolant passes through 40μm filter followed by a degasifier to remove all dissolved gases. A 0.50 ton chiller was used to

maintain the coolant temperature. A wye-connector was used to divide the main flow stream into two separate streams for both inlets of the mini-channel heat sink. A precision flow adjustment valve and a digital flow meter (Mc Millan-111) were mounted before both inlets to ensure the same flow rate through both channels. Then the water passed through the test module. One K-type thermocouple was placed in each inlet manifold to measure the inlet temperature of the coolant. Similarly, one K-type thermocouple was placed in each outlet manifold to measure the outlet temperature of the coolant. Four high precision pressure transducers (PX319-050AI) have installed in the inlet and outlet manifolds to

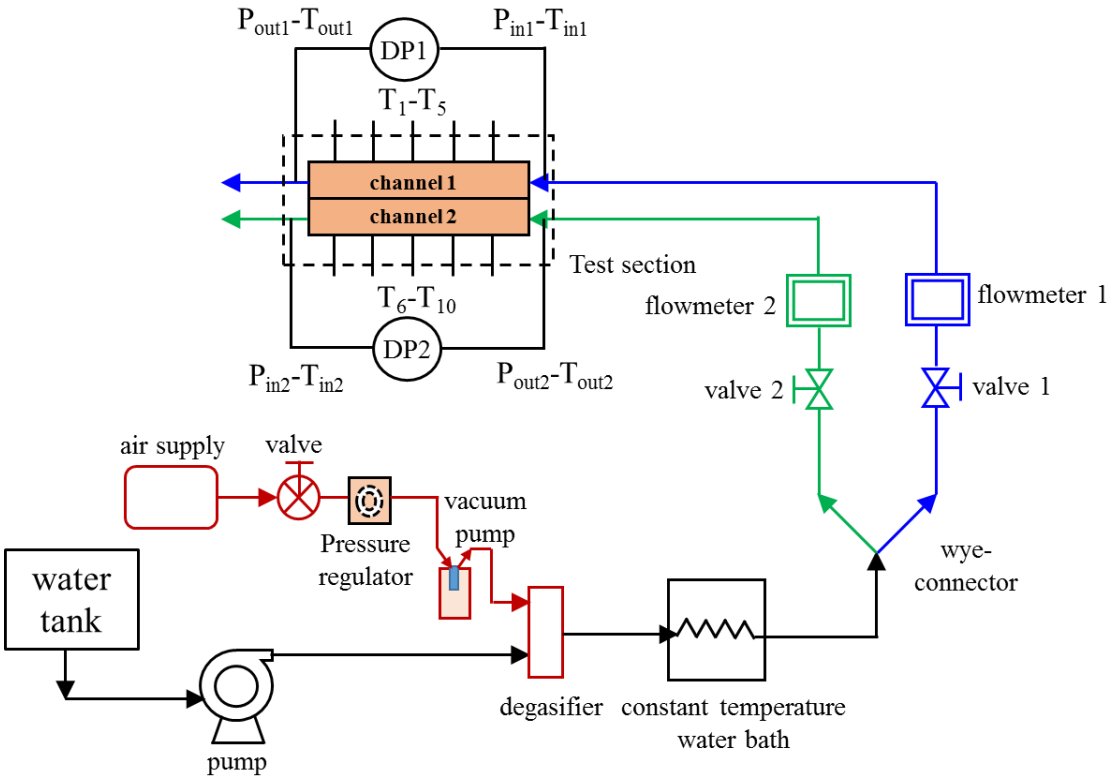

Figure 6.6 Flow loop for parallel flow mini-channel heat sink.

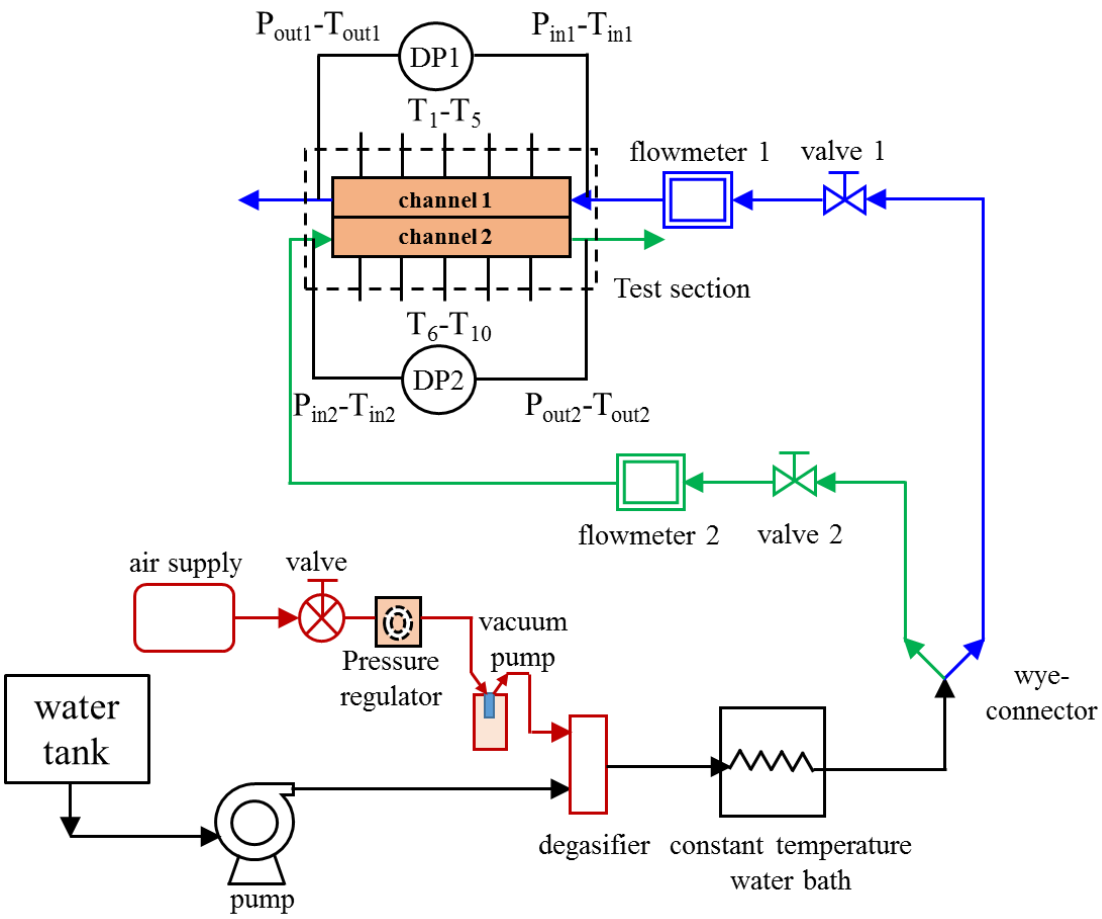

Figure 6.7 Flow loop for counter flow mini-channel heat sink.

measure the pressure drop across the mini-channel heat sink. Additionally, two high precision differential pressure transducers (PX2300-5BDI) were used to measure the pressure difference directly across both channels. One reservoir was placed in the downstream of both outlets to collect the exiting water from the test section which was opened to the atmosphere.

6.3.2 Degasification System

To remove dissolved gas from the from the coolant (deionized water), a degasification system has been installed before the chiller. The de-gasification system

consists of an air supply, a flow control valve, a pressure regulator manufactured by ARO Fluid management whose maximum pressure capacity was 200 psi, a vacuum pump manufactured by Cole Parmer and a degasifier (Mini Module Membrane Contractors). Figure 6.8 shows the schematic diagram of the degasifier system. Before the experiments, air supply was turned on by using the flow control valve and by controlling the pressure regulator, degasifier system pressure was set at 7 PSI throughout all the experiments. Afterward, pressurized air was supplied to the vacuum pump, which was connected to the vertically installed degasifier as shown in Figure 6.8. Finally, vacuum pump sucks all the dissolved gasses from the incoming liquid.

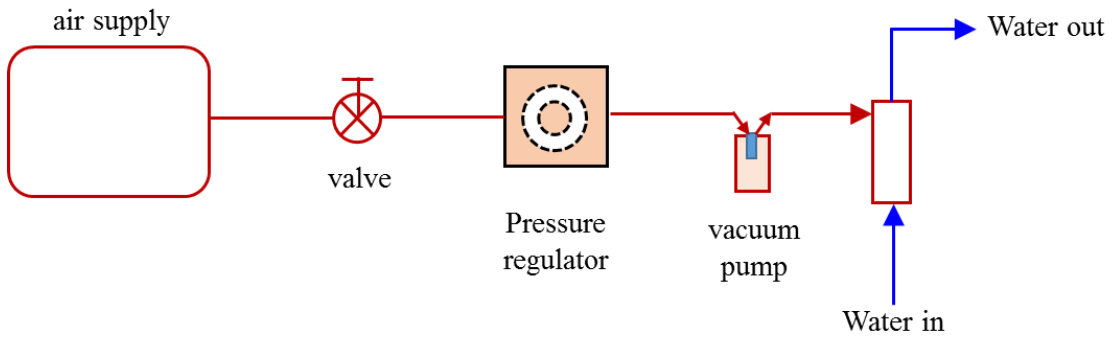

Figure 6.8 Schematic diagram of the de-gasification system.

6.3.3 Test Section Assembly

Figure 6.9 illustrates the actual test assembly of the mini-channel heat sink. Figure 6.10 shows the exploded view of the test section assembly. The test section comprises of six parts such as (1) polycarbonate clear plastic cover plate to visualize the flow behavior through the channels; (2) a housing block fabricated from G-7 fiberglass consists of inlet and outlet plenum and manifold which can sustain high temperature; (3) the copper mini-channel heat sink; (4) four cartridge heater which were inserted vertically into the heat sink; (5) two insulating blocks; (6) polycarbonate bottom plastic with four holes for heater wire

which was screwed to the top cover plastic to ensure tight contact of all six elements of test assembly. In the cover plastic, four holes were drilled for the inlet and outlet thermocouples. Moreover, on the side walls of the housing block along with the middle point of the inlet and outlet plenum, four pressure ports were drilled to hold the pressure transducers, as shown in Figure 6.11. In order to reduce the contact resistance between the heater elements and the copper heat sink, a thin layer of high heat conductive thermal adhesive (Arctic Silver) was applied on the surface of all the heater. The free space between the copper heat sink and housing block was filled with glass wool to minimize convective and radiative heat loss. Apart from that, a groove was cut on the G-7 housing block which was filled with silicon (Momentive RTV106) to prevent water leaking.

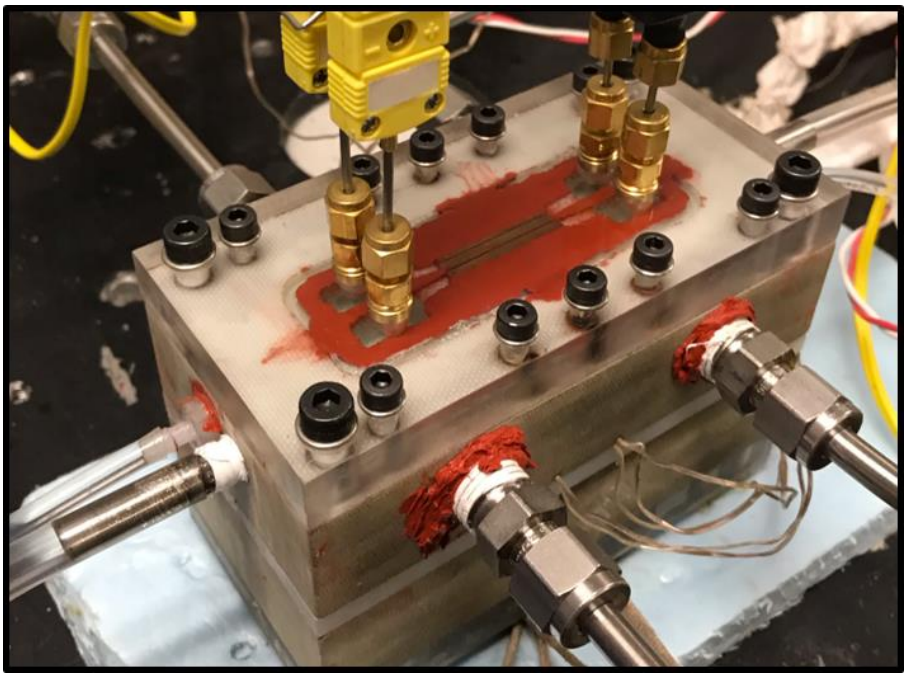

Figure 6.9 Actual test section assembly

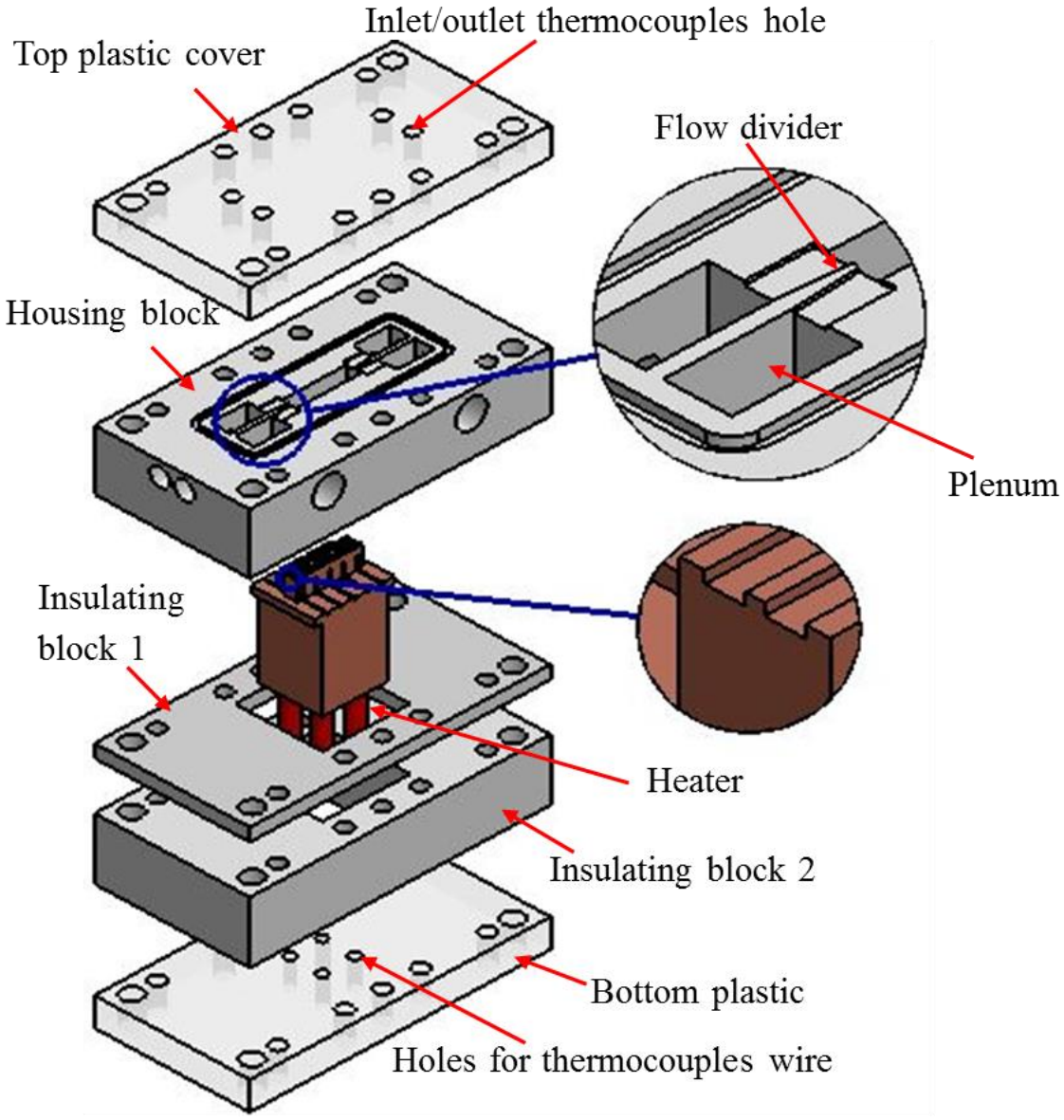

Figure 6.10 Exploded view of the test section assembly

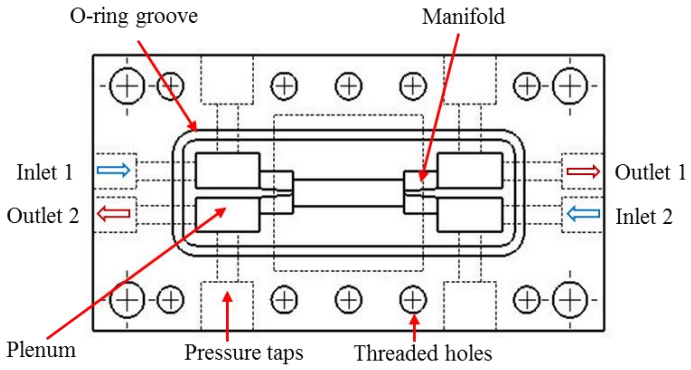

Figure 6.11 Top view of the housing block.

6.3.4 Power Supply System

Figure 6.12 shows the power supply system along with all the wire connections. The target mini-channel heat sink was heated by four 225W cartridge heaters (CHROMALOX, CIR-101 240V) which were inserted into the heat sink. A variable transformer (variac), model SRV-1000-R was used to supply AC power, which was connected to eight port terminal block. All four cartridge heaters were connected in parallel connection via the terminal block, as shown in Figure 6.12. The magnitude of the current and voltage was controlled by the sliding regulator of the variac.

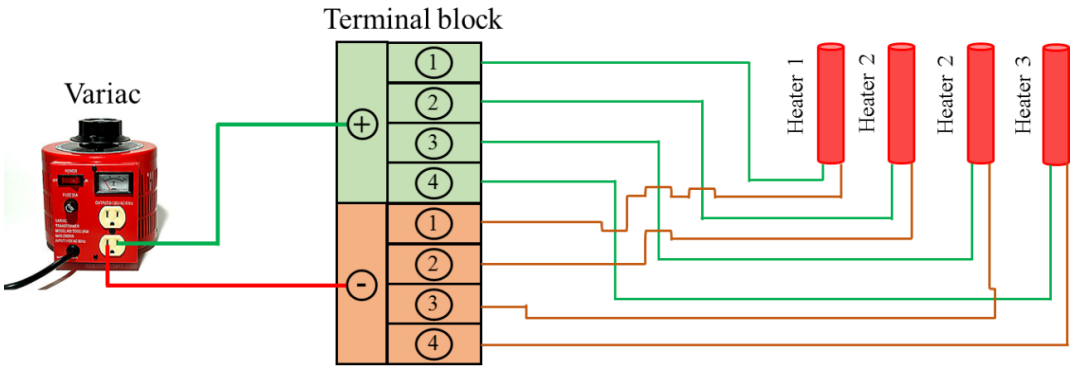

Figure 6.12 Schematic diagram of the power supply.

6.3.5 Data Acquisition System

Data from fourteen K-type thermocouples, four pressure transducers, and two differential pressure transducers along with two flow meters were recorded by a compact data acquisition system (cDAQ-9178) manufactured by Nationals Instruments. All thermocouples were connected to the LabVIEW program through the four NI 9210 DAQ module while all the pressure transducers and both flow meters were connected to the to the LabVIEW program through NI 9203 DAQ module. For all experiments, data acquisition frequency was set at 6 Hz. A block diagram and customized control window (front panel) have been built in LabVIEW to monitor and record the date provided by the measurement equipment. Figure 6.13 and Figure 6.14 show the block diagram and front panel that have been used to monitor and record the system data. The pressures were measured in PSI, and the temperatures were measured in ^{o}C.

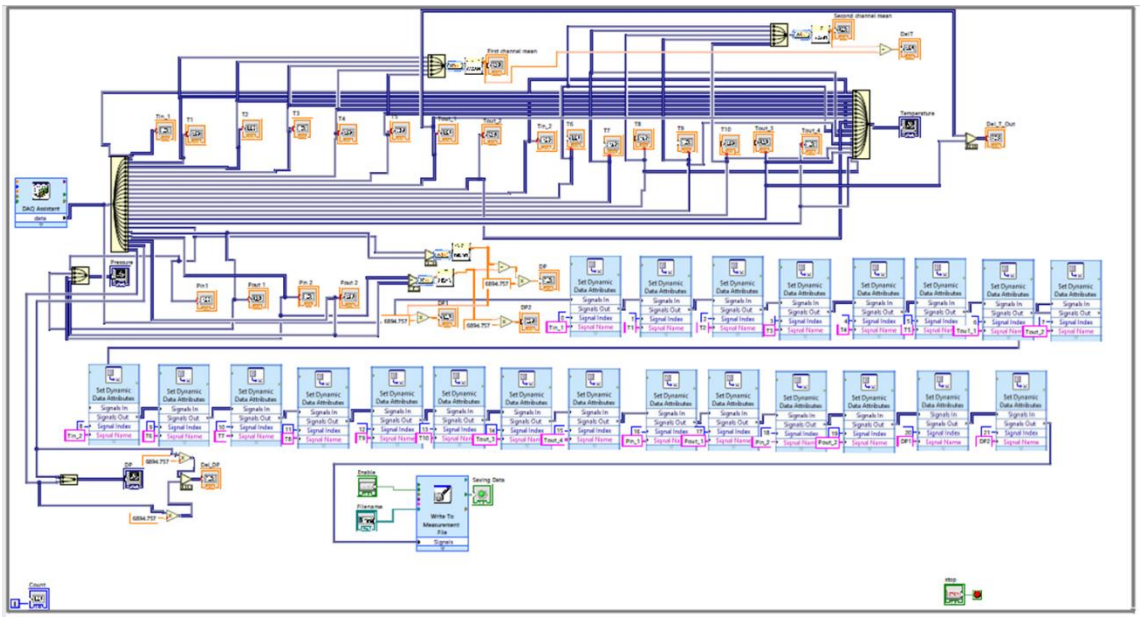

Figure 6.13 Block diagram of the LabVIEW program.

Figure 6.14 Front panel of the LabVIEW program.

6.4 Experimental Procedure

After assembling the test section, the whole assembly was placed on a foam box to minimize the radiative and convective heat loss from the bottom plastic. The gear pump was set at the desired flow rate without any heat supply. The chiller was set at the required temperature to maintain a constant coolant inlet temperature throughout all the experiments. Control valves were used to ensure the same flowrate through both channels. Once the flow rate and inlet temperature become stable, the power supply of the heaters was turned on and set at the desired value by adjusting the variac controller.

Real-time temperature reading of all thermocouples was monitored continuously by using LabVIEW software, and steady-state condition was considered to be reached when all the thermocouple readings were within ±0.2^{o}C for 10 min. period. Generally, 30-90 min. was required to reach the steady state condition based on the flow rate. Once

steady-state was reached, the temperature, pressure, and flow rate readings were recorded by LabVIEW for at least ten minutes time-period. Time-average of all recorded values were calculated to obtain a single data point. For each flow rate, two readings of the voltage and current input of the power supply were recorded manually by using a precision FLUKE multi-meter, and finally, their average value was used for the data reduction. Total heat input and coolant flow rate were kept at the same values for both conventional and inter-connected counter flow mini-channel heat sink for a fair comparison. Experiments were conducted under laminar flow regime for a Reynolds number ranging from 110 to 480, and for all experiments, the total heat input was ~18.2W.

6.5 Experimental Data Reduction

Surface temperature of the heat sink was calculated by taking the average of the ten thermocouples reading which were embedded in the underneath of the mini-channels:

$$T_{w,b} = \frac{\sum_{i=1}^{10} T_{w,b,i}}{10} \tag{6.1}$$

Where, $T_{w,b,i}$ is the temperature reading of ten thermocouples.

Since the ambient temperature was constant during the experiments, therefore heat loss was a function of surface temperature, $T_{w,b}$ of the heat sinks only. By measuring the surface temperature of the test section at different heating conditions without water flow, a heat loss equation was established as a linear function of $T_{w,b}$ as shown below. A similar heat loss characterization method was utilized by Jenget et al. [79].

$$Q_{loss} = 0.0526T_{w,b} - 0.4683 \tag{6.2}$$

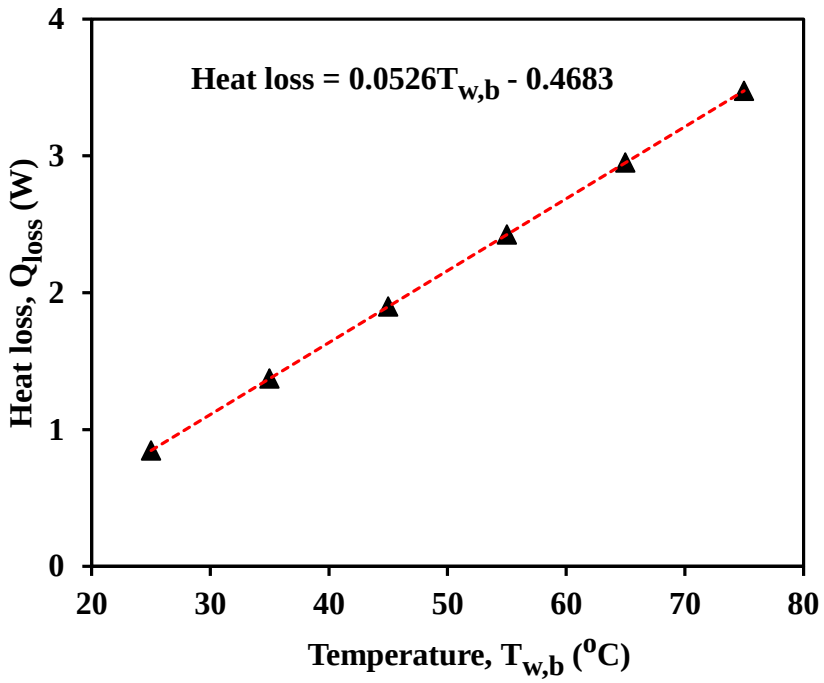

Figure 6.15 Heat loss as a function of heat sink temperature.

Total electric heat input was calculated as:

$$Q_{input} = VI \tag{6.3}$$

Where, V and I are the supplied voltage and current to the heater.

The effective heat input was calculated as follows:

$$Q_{eff} = Q_{input} - Q_{loss} \tag{6.4}$$

The effective heat flux was evaluated as

$$Q''_{eff} = \frac{Q_{eff}}{int} \tag{6.5}$$

Where A_{int} is the interfacial area for convective heat transfer.

By assuming 1D conduction heat transfer in the copper block, the bottom surface temperature of the mini-channel was calculated by extrapolating from the measured surface temperature of the heat sink:

$$T_{int} = T_{w,b} - \frac{Q''_{eff}\Delta X}{K_{so}} \tag{6.6}$$

Where K_{so} is the thermal conductivity of the copper substrate and ΔX is the distance between thermocouples and the bottom surface of the mini-channels.

The average fluid temperature was measured by averaging the inlet and outlet temperature of the coolant:

$$T_m = \frac{T_{in}+T_{out}}{2} \tag{6.7}$$

Where $T_{in} = \frac{T_{in,1}+T_{in,2}}{2}$ is the average coolant inlet temperature and $T_{out} = \frac{T_{out,1}+T_{out,2}}{2}$ is the average coolant outlet temperature.

Average heat transfer coefficient was calculated by using the following equation:

$$h = \frac{Q''_{eff}}{T_{int}-T_m} \tag{6.8}$$

The corresponding average Nusselt number was calculated as follows:

$$Nu = \frac{hD_h}{k_f} = \frac{Q''_{eff}D_h}{(T_{int}-T_m)k_f} \tag{6.9}$$

Where K_f is the thermal conductivity of the fluid, and D_h is the hydraulic diameter of the mini-channel heat sink which was defined as:

$$D_h = \frac{2WH}{W+H} \tag{6.10}$$

Where W and H are the width and height of the mini-channels respectively.

Overall thermal resistance of the heat sink was defined as:

$$R_{th} = \frac{T_{w,b} - T_{in}}{Q_{eff}} \tag{6.11}$$

The friction factor was calculated using the following equation:

$$f = \frac{-2\frac{\Delta p}{L} D_h}{\rho_f {u_m}^2} \tag{6.12}$$

Where $\Delta p = p_{in} - p_{out}$ is the average pressure difference across the both channels, ρ_f is the water density, and u_m is the coolant mean velocity which was calculated as follows:

$$u_m = \frac{\dot{Q}}{A_c} \tag{6.13}$$

Where $\dot{Q}$ is the coolant flowrate through each channel and $A_c (= WH)$ is the cross-sectional area of the mini-channels.

Reynolds number was defined as:

$$Re = \frac{\rho_f v_m D_h}{\mu_f} \tag{6.14}$$

Where μ_f is the coolant viscosity.

6.6 Thermo-physical Properties

All thermo-physical properties of the coolant were evaluated at the mean coolant temperature (T_m) by using the following polynomial equations:

$$\rho_f = 999.8748 + 6.6821 \times 10^{-2} T_m - 9.2686 \times 10^{-2} {T_m}^2 + 1.2318 \times 10^{-4} {T_m}^3 - 1.8895 \times 10^{-6} {T_m}^4 + 1.4385 \times 10^{-8} {T_m}^5 \quad (6.15)$$

$$\mu_f = 1.7866 \times 10^{-3} - 6.039 \times 10^{-5} T_m + 1.4718 \times 10^{-6} {T_m}^2 - 2.5655 \times 10^{-8} {T_m}^3 + 2.7464 \times 10^{-10} {T_m}^4 + 1.3109 \times 10^{-12} {T_m}^5 \quad (6.16)$$

$$k_f = 0.5650285 - 9.412945 \times 10^{-4} {T_m}^{(1/2)} + 2.6363895 \times 10^{-3} T_m - 1.2516934 \times 10^{-4} {T_m}^{(3/2)} - 1.5154915 \times 10^{-6} {T_m}^2 \quad (6.17)$$

Where mean coolant temperature, T_m is in Degree Celsius.

The thermal conductivity of the copper substrate was assumed constant (391 $W.m^{-1}.K^{-1}$).

6.7 Experimental Uncertainty Analysis

The average uncertainty of all geometric dimensions was less than 2% whereas the uncertainties of current and voltage measurement were less than 4%. All K-type thermocouples uncertainty was ±0.5°C. Flow meters and pressure transducers with an uncertainty of less than 5% and 3% were utilized for flow rate and pressure measurements respectively.

The uncertainty of all the derived parameters was calculated by the standard error propagation equation proposed by Kline and McClintock [80]. For example, if a derived parameter, F is a function of some measured parameters such as $a_1, a_2, \ldots . a_n$ and if we know uncertainties of all the measured parameters such as $U_{(a_1)}, U_{(a_2)}, \ldots . . U_{(a_n)}$, the uncertainity of F, U_F can be calculate by using the following equation:

$$F = f(a_1, a_2, \ldots . a_n) \rightarrow U_F = \sqrt{\sum_{i=1}^{n} \left\{ \frac{\partial F}{\partial a_i} U_{(a_i)} \right\}^2} \quad (6.18)$$

The average uncertainty of all the calculated parameters are listed in the following Table 6.1:

Table 6.1 Uncertainty calculation

Parameter	% of uncertainty
Re	6.15
Nu	7.25
Nu/Nu_o	10.25
f	7.05
f/f_o	10.00
Thermal resistance, R_{th}	6.50
Pumping power, P_p	5.85
Entropy generation rate, S	11.5
PEC	11.75

6.8 Experimental Validation

To validate the accuracy and reliability of the experimental setup, experimentally obtained Nu for the conventional parallel flow mini-channel heat sink were compared with the corresponding experimental results of Fan et al. [57] as shown in Figure 6.16. The comparison illustrated that the experimentally obtained Nu was in good agreement with the experimental work of Fan et al. The average deviation between the present Nu and Nu reported by Fan et al. [57] was less than 5.16%. However, a maximum deviation of

9.36% was recorded at the lowest considered Re ($Re = 110$) which can be attributed to significantly higher flow rate measurement uncertainty of the used flowmeters at the lowest Re. Moreover, the % deviation reduced gradually as the flow rate increased and reached to a minimum deviation of ~0.32% at the highest considered Re ($Re = 480$).

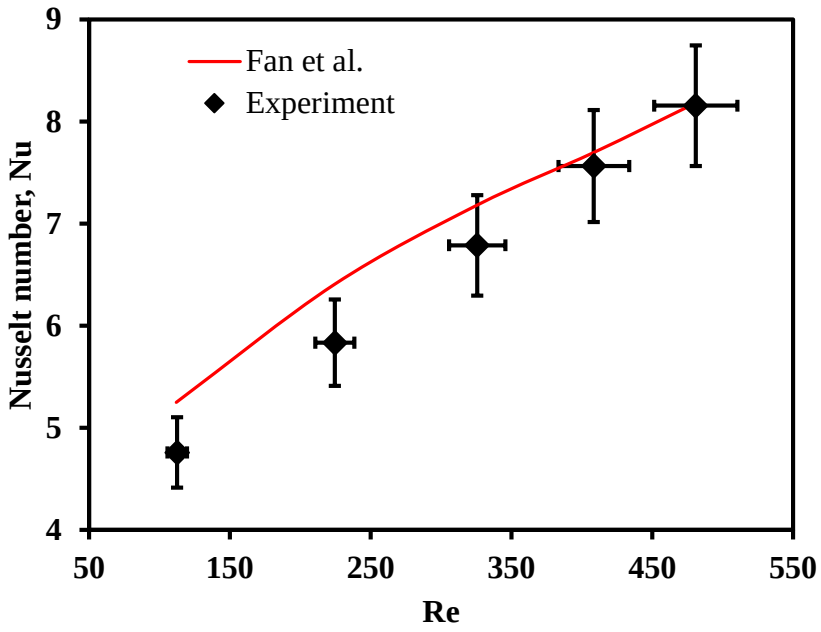

Figure 6.16 Comparison of present experimentally obtained Nu with the experimental results of Fan et al. [57] for parallel flow heat sink.

Similarly, experimentally obtained f for conventional parallel flow mini-channel was compared with the well stablished Shah and London correlation [57] as shown in Figure 6.17. From the Figure 6.17, it can be seen that predicted f values from the correlation lied within the uncertainty limit of the experimental f for all considered Re range. The average deviation between the experimental f and correlation was less than 1.43%. whereas a maximum deviation of 1.77% was recorded at the highest considered Re ($Re = 480$).

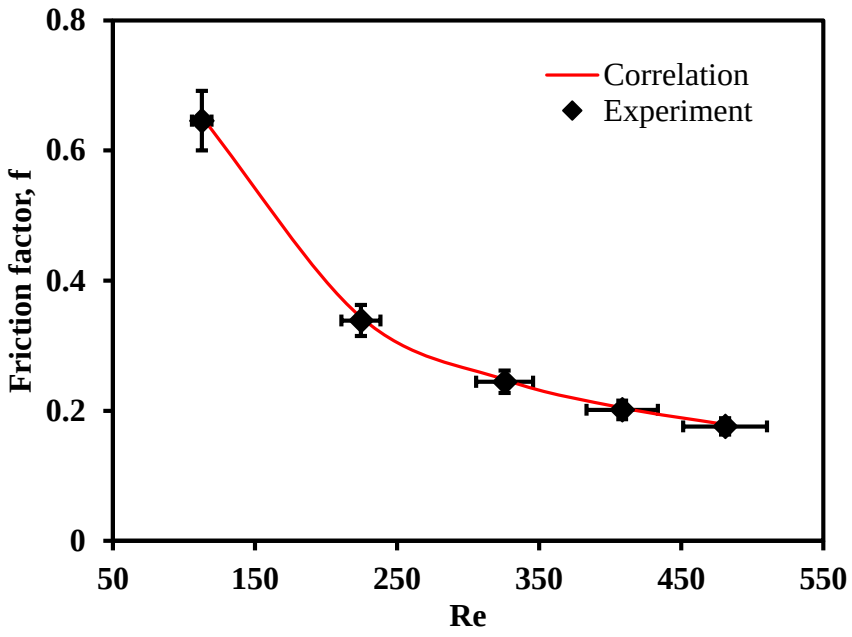

Figure 6.17 Comparison of present experimentally obtained f for parallel flow heat sink with Shah and London correlation [75].

6.9 Repeatability

To check the reliability and also, to ensure that the data obtained from the mini-channel heat sinks setup were free from any random errors, for all considered mini-channel heat sinks, the entire sets of experiments were repeated for at least two times. Figure 6.18 illustrates the Nu values obtained from both test for all conventional and inter-connected parallel and counter flow mini-channel sinks. From the Figure 6.18, it can be observed that the deviations between each two data sets were within the experimental uncertainties. For example, for conventional parallel flow mini-channel heat sink, the average deviation between the two tests was less than 2.17%. Similarly, the average deviation between the two tests for inter-connected parallel flow, counter flow, and inter-connected counter flow mini-channel heat sinks were less than 0.70%, 1.08%, and 1.71% respectively. Similarly,

the repeatability of f was also checked for all considered heat sinks. Finally, for all parameters, the average value of the data obtained from the two tests were used for the final calculation.

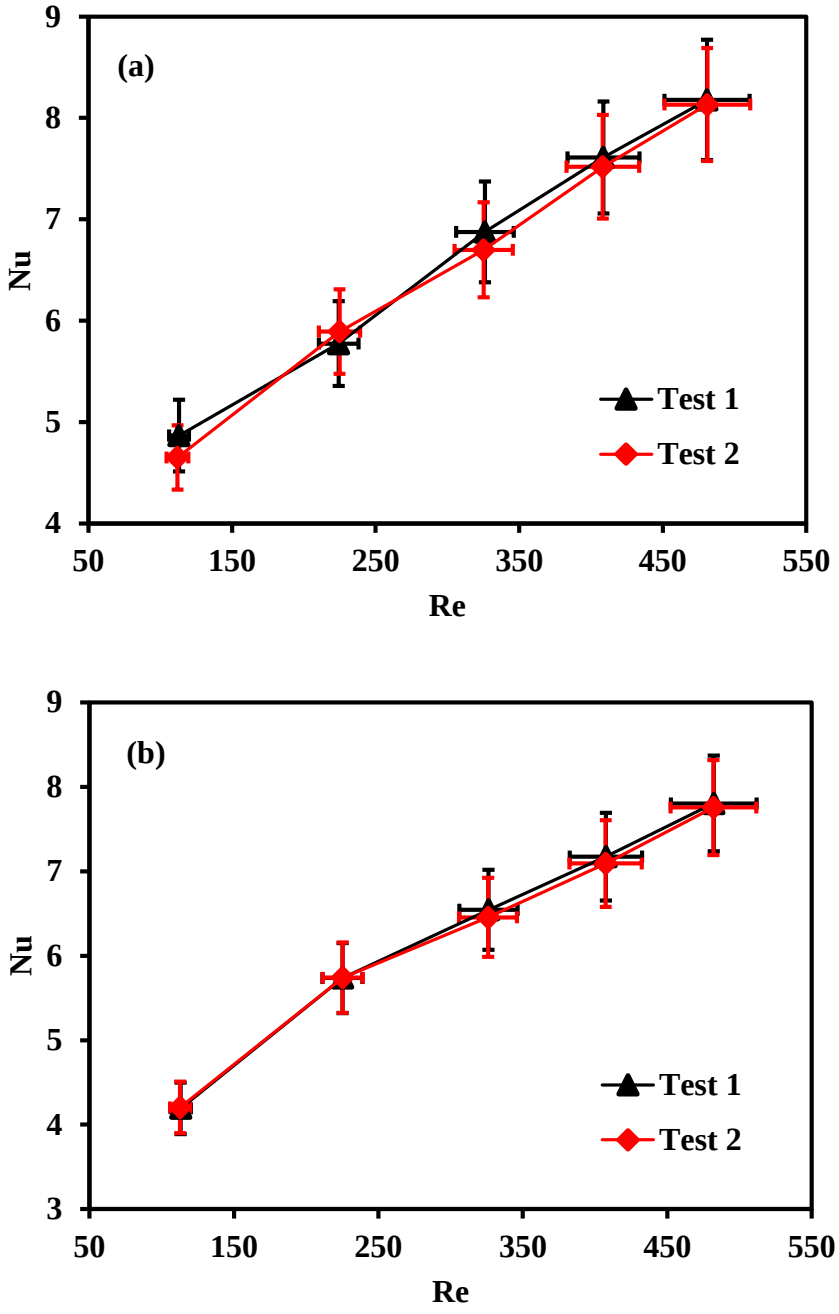

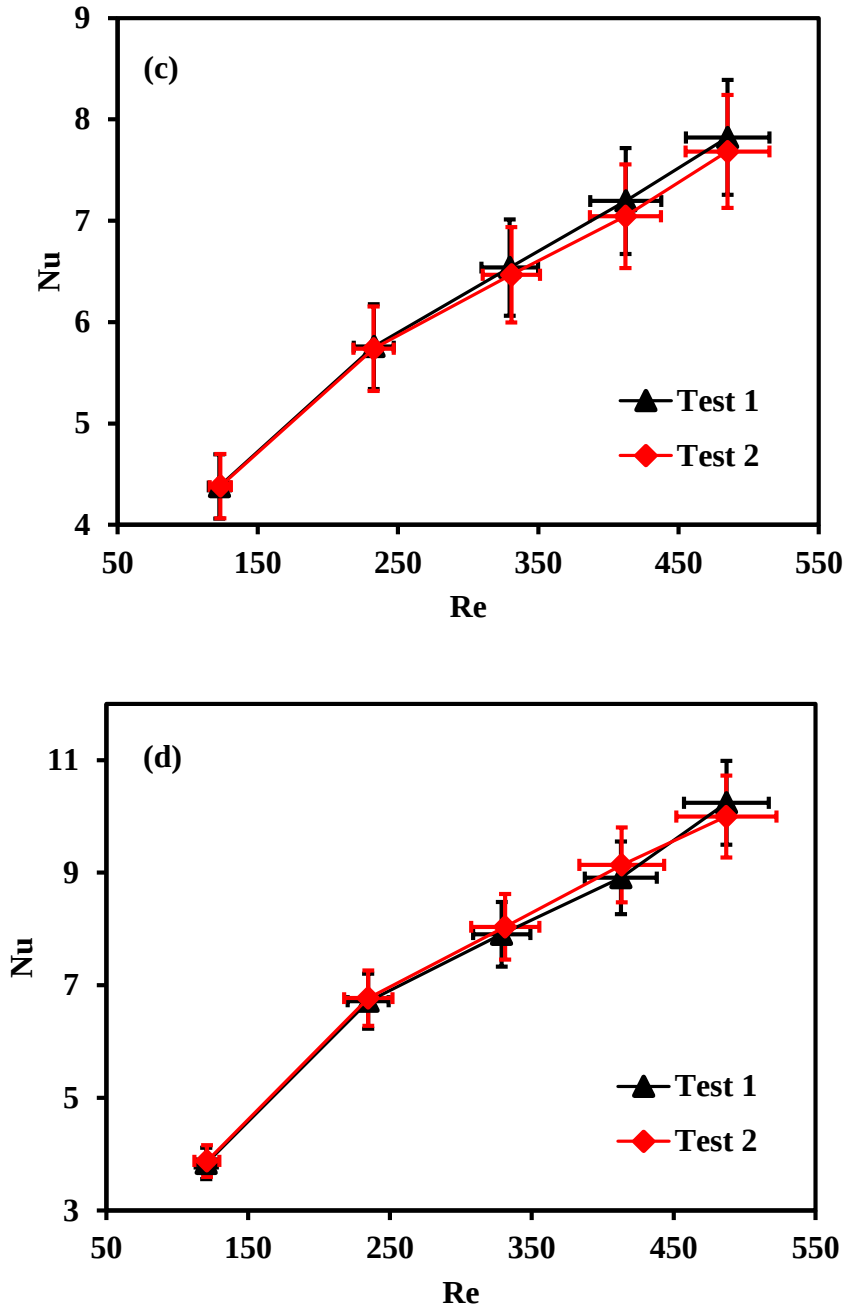

Figure 6.18 Nu vs. Re graph as repeatability test for (a) parallel flow, (b) inter-connected parallel flow, (c) counter flow, and (d) inter-connected counter flow mini-channel heat sinks.

6.10 Results and Discussions

6.10.1 Local temperature distribution

Figure 6.19 depicts the local surface temperature distribution for all considered mini-channel heat sinks at $Re = 330$. For parallel flow mini-channel heat sink, surface temperature gradually increases from the inlet to the outlet because of the gradually growing thermal boundary layers. Similar temperature distribution is evident for inter-connected parallel flow mini-channel heat sink because of almost no secondary flow through the inter-connectors. Moreover, in case of inter-connected parallel flow mini-channel heat sink, higher surface temperature is evident for all considered Re as shown in the Figure 6.19. This can be attributed to the stationary recirculation zones inside the inter-connectors. For counter flow mini-channel heat sink, much uniform and symmetric temperature distribution is evident because of the opposite flow direction in the adjacent channels.

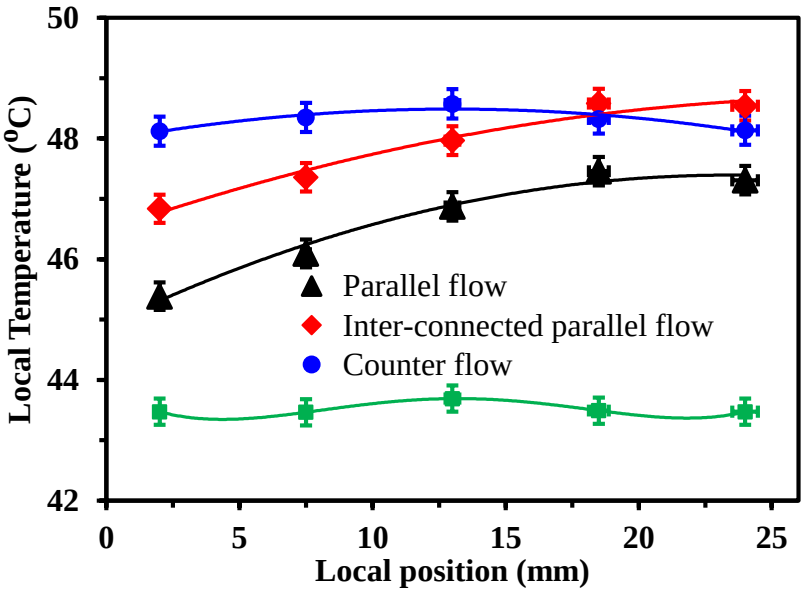

Figure 6.19 Local temperature distribution at $Re = 330$.

However, in case of counter flow mini-channel, higher surface temperature is corded at both inlets compared to the inlet of the parallel flow mini-channel heat sink. Moreover, in case of inter-connected counter flow mini-channel heat sink, a significant amount of secondary flow breakup the thermal boundary layer and hence reduces the surface temperature significantly as shown in Figure 6.19.

6.10.2 Base Surface Temperature

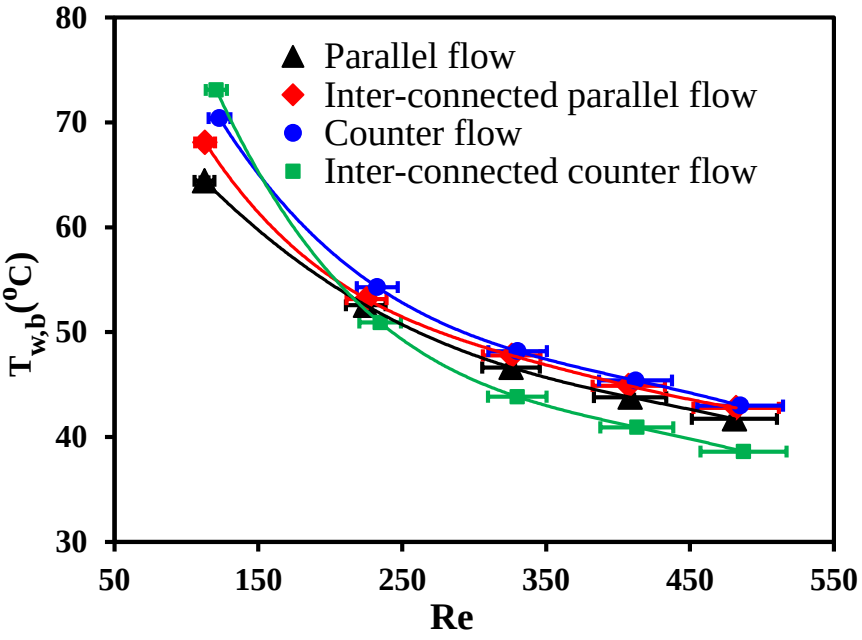

Figure 6.20 Base surface temperature vs. Re.

Figure 6.20 depicts the bottom surface temperature distribution for all considered mini-channel heat sinks as a function of Re. From the Figure 6.20, it can be seen that the inter-connected parallel flow mini-channel heat sink provides higher temperature compared to the conventional parallel flow mini-channel heat sink because of the no secondary flow through the inter-connectors as explained earlier. Moreover, conventional counter flow mini-channel heat sink also provides higher surface temperature compared to

the conventional parallel flow mini-channel. It is worth mentioning that in case of counter flow mini-channel, half of the incoming coolant enters into the heat sink through the opposite inlet resulting in higher surface temperature in both end of the heat sink. Form the Figure 6.20, it can also be observed that at low Re ($Re \leq 200$), counter flow mini-channel equipped with inter-connectors provides higher surface temperature while at higher Re ($Re > 200$), inter-connected counter flow mini-channel heat sink provides substantial lower surface temperature compared to the conventional parallel and counter flow mini-channel heat sink. At low Re, most of the incoming coolant flows transversely through the inter-connectors resulting higher surface temperature in-between two inter-connectors. For example, at $Re = 110$ and for inter-connected counter flow mini-channel, surface temperature increased by ~8.67^{o}C compared to the parallel flow channel. On the contrary, moderate amount of transverse flow resulting in lower surface temperature at high Re. At $Re = 480$, a maximum 3.12^{o}C reduction of the surface temperature of the heat sink was achieved for modified counter flow heat sink compared to the parallel flow heat sink.

6.10.3 Heat Transfer Characteristics

Figure 6.21 and Figure 6.22 illustrates the variation of Nusselt number, Nu and Nusselt number ratio, Nu/Nu_o as a function of Re for all configurations. For all configurations, Nu progressively increases as Re increases. It is worth mentioning that the thickness of the thermal and hydraulic boundary layers reduces gradually as coolant velocity increases which eventually results in higher heat dissipation, i.e., higher Nu. In case of inter-connected parallel flow and conventional counter flow mini-channel heat sinks, higher heat sink temperature leads to lower Nu and hence provide the value of Nu/Nu_o less than 1 for all Re range as shown in the Figure 6.21 and Figure 6.22. For

example, at $Re = 110$ and for modified parallel and conventional counter flow mini-channel heat sinks, Nu reduced by ~11.80% and ~7.95% respectively compared to the conventional parallel flow mini-channel heat sink. However, in case of inter-connected counter flow mini-channel heat sink, two opposite heat transfer behavior is evident at low and high Re. At the lowest considered coolant flowrate ($Re \leq 200$), higher surface temperature leads to lower Nu. For example, in case of modified counter flow mini-channel and at $Re = 110$, Nu reduced by ~18.87% compared to the conventional parallel flow heat sink. However, as Re increases, modified heat sink provides substantially lower surface temperature as explained earlier which eventually results in higher Nu in comparison with the conventional counter flow mini-channel heat sink. For example, at $Re = 480$, the overall Nu of the modified heat sink was ~24% higher than the conventional mini-channel heat sink.

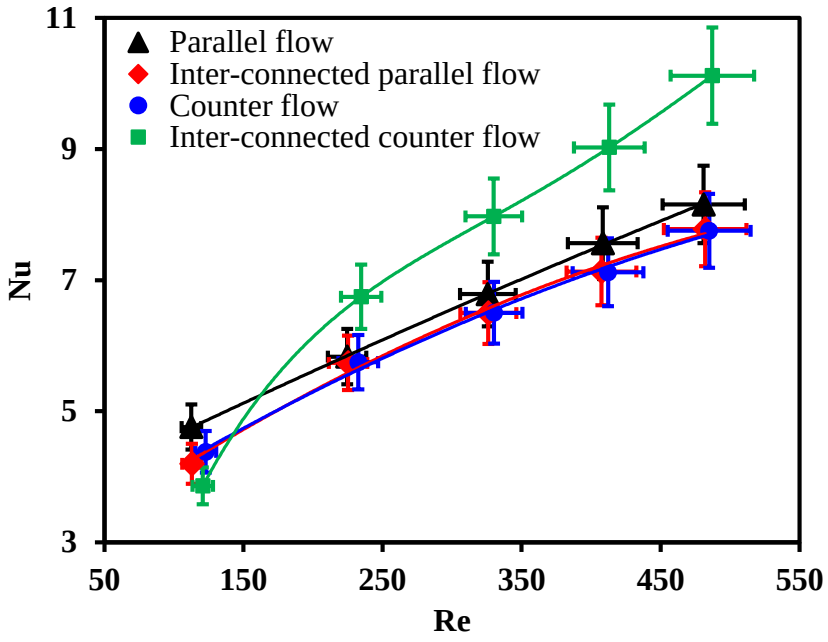

Figure 6.21 Nusselt number, Nu vs. Re.

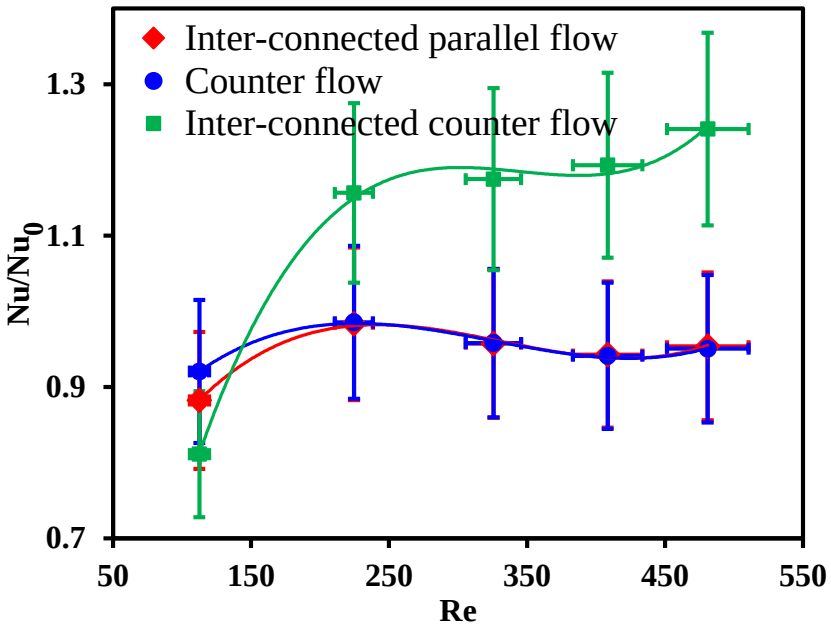

Figure 6.22 Nusselt number ratio, Nu/Nu_o vs Re.

6.10.4 Friction Factor Characteristics

Figure 6.23 and Figure 6.24 presents the variation of friction factor, f and friction factor ratio, f/f_o with Re for both conventional and modified parallel and counter flow mini-channel heat sinks. Interestingly, in case of inter-connected parallel flow mini-channel heat sink and at low Re ($Re \leq 200$), friction factor value increased compared to the conventional channel. This can be attributed to the generated recirculation zone inside and around the secondary channels. For example, at $Re = 110$, f raised by ~8.30% compared to the parallel flow mini-channel. On the contrary, reduced dynamic viscosity resulting in friction factor reduction at higher Re despite of almost no secondary flow as shown in the Figure 6.23. For example, at $Re = 480$, f reduced by ~6.0% compared to the conventional parallel flow mini-channel. Moreover, in case of the conventional counter flow mini-channel heat sink and at low Re ($Re \leq 200$), higher surface temperature reduces

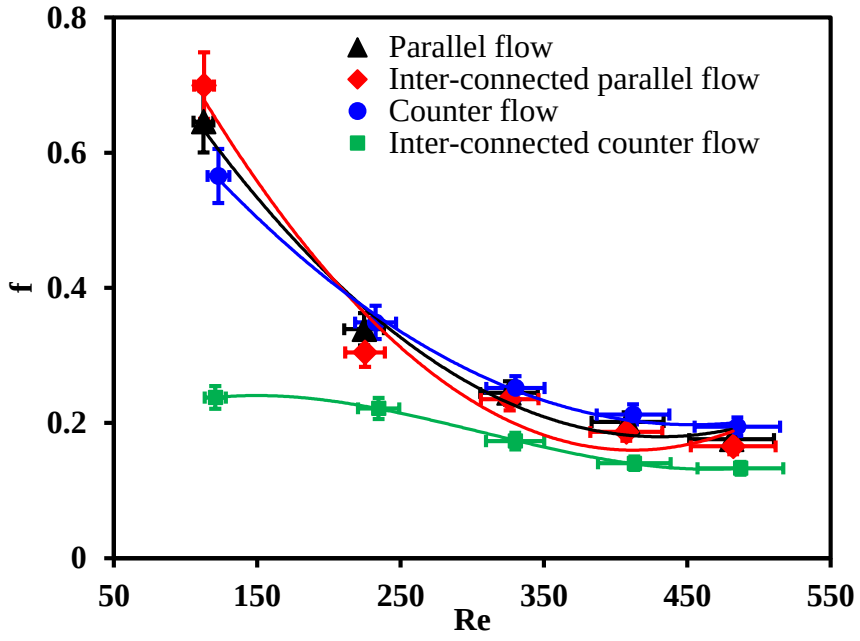

Figure 6.23 friction factor, f vs. Re.

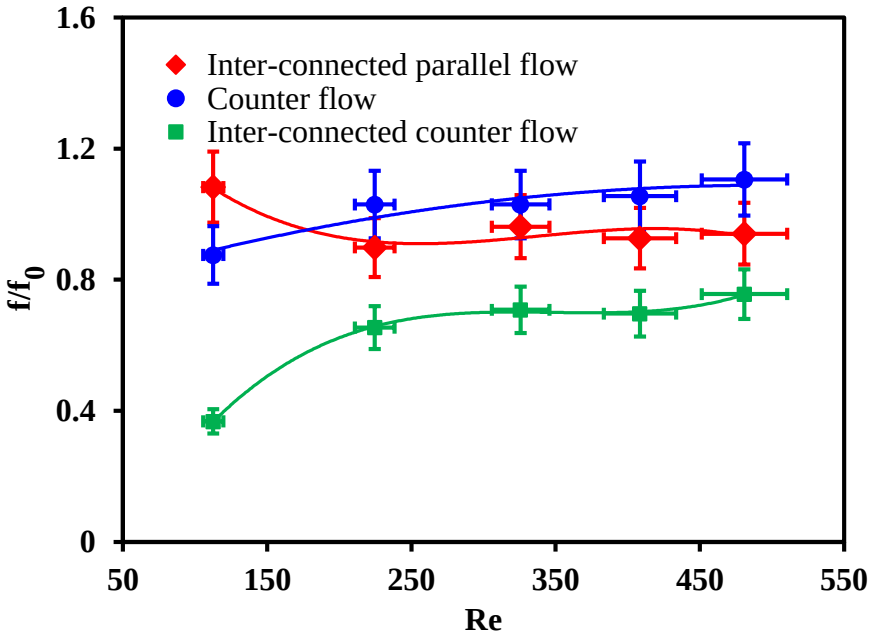

Figure 6.24 Ratio of friction factor, f/f_o vs. Re.

the dynamic viscosity of the coolant, which eventually reduced the friction factor compared to the conventional channel. However, for counter flow mini-channel heat sink, friction

factor value increased at higher Re $(Re > 200)$. For example, for counter flow mini-channel and at $Re = 110$, f reduced by ~12.50% and at $Re = 480$, f increased by ~10.55% compared to the conventional channel. From the Figure 6.23, it can also be seen that, inter-connected counter flow mini-channel heat sink provides a substantial reduction in f at low Re. Low Re indicates less flow inertia of the incoming coolant which allows higher transverse flow despite of less pressure difference across the inter-connectors. Therefore, surface and coolant temperature increased significantly in-between two inter-connectors. As a resultant of these two effects, pressure drop requirement reduced by ~63.21% compared to the parallel flow mini-channel at the lowest Re of 110. As Re increases, the amount of transverse flow reduces because of higher flow inertia results in relatively higher f. However, the magnitude of f for the modified counter flow mini-channels was still significantly lower in comparison with the conventional channel. For example, at $Re = 480$, the overall f of the modified heat sink was ~24.40% lower than the conventional channel.

6.10.5 Thermal Resistance Vs. Pumping Power

Figure 6.25 shows the overall thermal resistance vs. pumping power graph for all configurations. Since coolant inlet temperature and total heat input were constant during all experiments, the overall thermal resistance mainly depends on bottom surface temperature and follows the same trend of $T_{w,b}$. Similarly, pumping power requirement follow the same trend as friction factor as shown in the Figure 6.25. At lower Re $(Re \leq 200)$, inter-connected counter flow mini-channel heat sink shows higher thermal resistance with a significant reduction of pumping power requirement while at higher Re $(Re > 200)$, modified counter flow heat sink provides significantly lower thermal

resistance with a moderate reduction of pumping power compared to the conventional channel. For example, in case of the modified counter flow heat sink and at $Re = 110$, the overall thermal resistance increased by ~14.70% and pumping power reduced by ~64.60% while at $Re = 480$, the overall thermal resistance reduced by a maximum ~18.14% and pumping power reduced by ~24.40% compared to the parallel flow mini-channel heat sink.

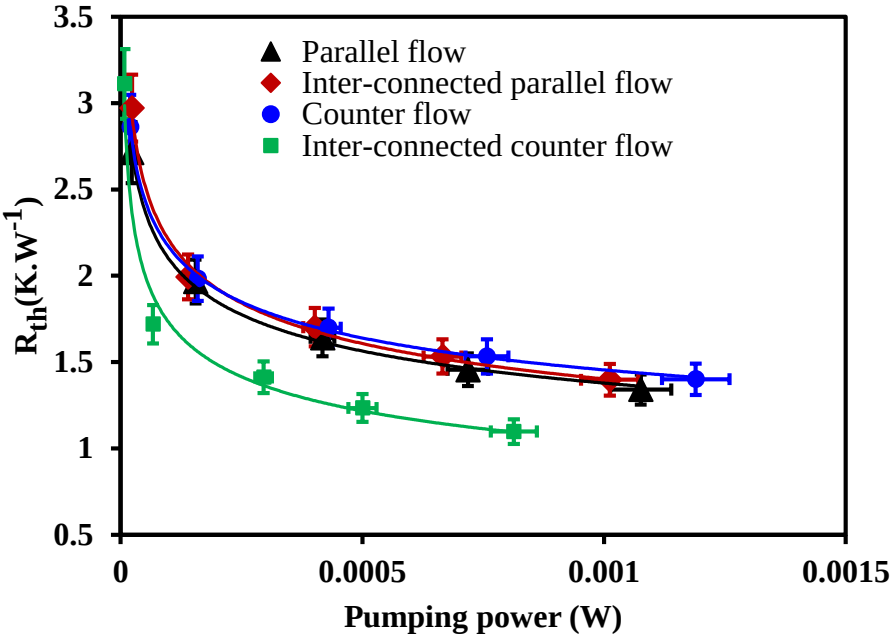

Figure 6.25 Thermal resistance vs. required pumping power.

6.10.6 Characteristics of Entropy Generate Rate

Figure 6.26 illustrated the entropy generation rate, S as a function of Re for all configurations. From the figure, it can be seen that, for all configurations, the magnitudes of S gradually reduces as Re increases. However, inter-connected parallel flow mini-channel heat sinks provides higher S for all considered Re. For example, at $Re = 110$ and for inter-connected parallel flow mini-channel heat sinks, S increased by ~5% compared to the conventional parallel flow mini-channel. On the contrary, counter flow mini-channel

provides higher S at lower Re ($Re \leq 150$) and lower S at higher Re ($Re > 150$) compared to the parallel flow mini-channel heat as shown in the Figure 6.26. For example, in case of counter flow mini-channel heat sink and at $Re = 110$, S increased by ~1% whereas at $Re = 480$, S reduced by ~6% compared to the conventional heat sink. Similar entropy generation profile is evident for inter-connected counter flow mini-channel heat sink. For example, in case of inter-connected counter flow mini-channel heat sink and at $Re = 110$, S increased by ~4.27% whereas at $Re = 480$, S reduced by ~14.70% compared to the conventional heat sink.

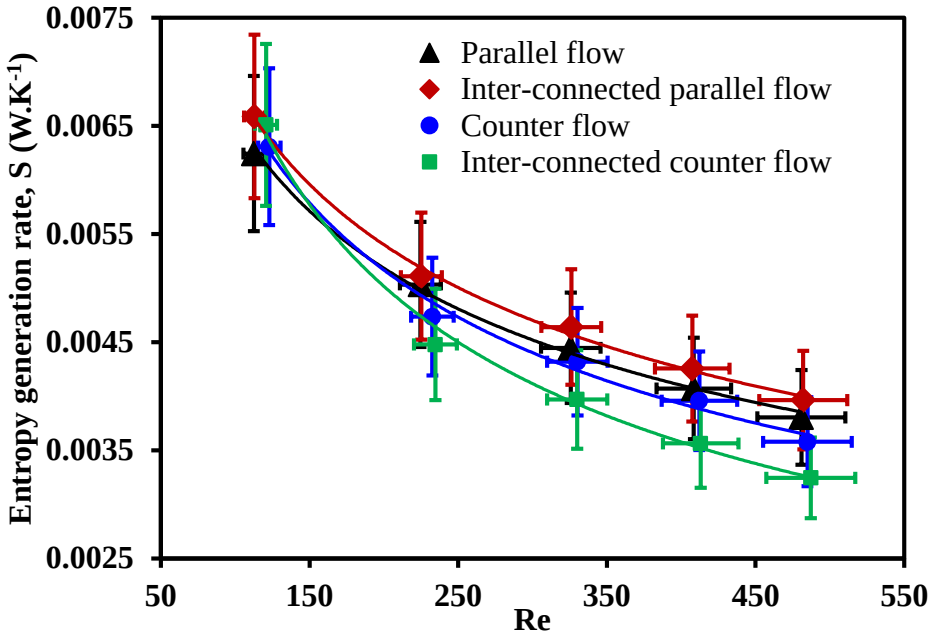

Figure 6.26 Entropy generation rate, S vs. Re.

6.10.7 Performance Evaluation Criteria

Figure 6.27 shows the characteristics of performance evaluation criteria (PEC) as a function of Re for all considered configurations. In case of inter-connected parallel flow

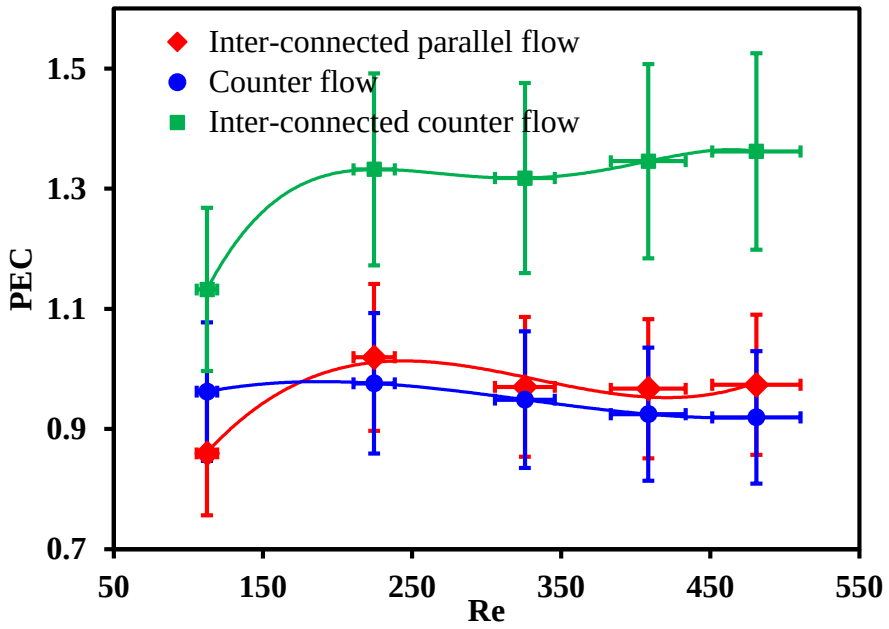

Figure 6.27 PEC vs Re.

mini-channel heat sink, the ratio of Nu were less than 1, and the ratio of f were very comparable to the conventional parallel flow channel as shown in Figure 6.22 and Figure 6.24. Therefore, PEC value become less than 1 for inter-connected parallel flow mini-channel heat sink and for all considered Re except $Re = 225$ as evident in the Figure 6.27. However, for conventional counter flow mini-channel heat sink, higher f/f_o compared to the inter-connected parallel flow heat sink leads to lower PEC value than the conventional parallel flow channel despite of almost similar Nu/Nu_o except for the lowest Re. At $Re = 110$, counter flow mini-channel heat sink provides relatively higher Nu and lower f compared to the inter-connected parallel flow mini-channel as discussed earlier resulting in higher PEC value as shown in the Figure 6.27. It is worth mentioning that in case of inter-connected counter flow mini-channel heat sink, higher Nu/Nu_o except for the lowest Re and lower f/f_o for all considered Re resulting in higher PEC value as shown in the Figure 6.27. For example, at $Re = 480$, PEC value reached to ~1.36 for inter-connected

counter flow mini-channel. Additionally, in the case of inter-connected counter flow mini-channel heat sink, PEC reached to an almost constant value of ~1.34 with a variation of less than ±2.2% for a wide range of Re ($225 \leq Re \leq 480$). Interestingly, at the lowest Re ($Re = 110$), significant reduction of f, in particular ~63.21%, results in a PEC value greater than 1 despite of reduced Nu as explained in Figure 6.22. For example, at Re=110, inter-connected counter flow mini-channel heat sink provides a PEC value of ~1.13.

6.11 Comparison Between Experimental and Numerical Results

In order to compare the experimental obtained Nu and f results with the corresponding numerically predicted results, numerical simulations were re-run again for case 9 of CHAPTER 5 at the appropriate experimental conditions, i.e., effective heat flux, flow rate, inlet temperature, and coolant thermo-physical properties. Figure 6.28 to Figure 6.31 show the comparison between the experimental and numerical results for conventional and inter-connected parallel and counter flow mini-channel heat sinks. From the Figure 6.28 (a) to Figure 6.31 (a), it can be seen that the numerically predicted Nu are in good agreement with the experimentally obtained Nu for all configurations. For example, in case of conventional parallel flow mini-channel heat sink, the average deviation between the experimental and numerical Nu was less than 8.12%. Similarly, the average deviation between the experimental and numerical Nu were less than 4.17%, 9.50%, and 7.18% for the inter-connected parallel flow, counter flow, and inter-connected counter flow mini-channel heat sinks respectively. Moreover, numerical simulation can also predict the f as compared to the experimental results for all configurations except the inter-connected counter flow mini-channel heat sink as evident in Figure 6.28 to Figure 6.31 (b). For example, the average deviation between the experimental and numerical f were less than

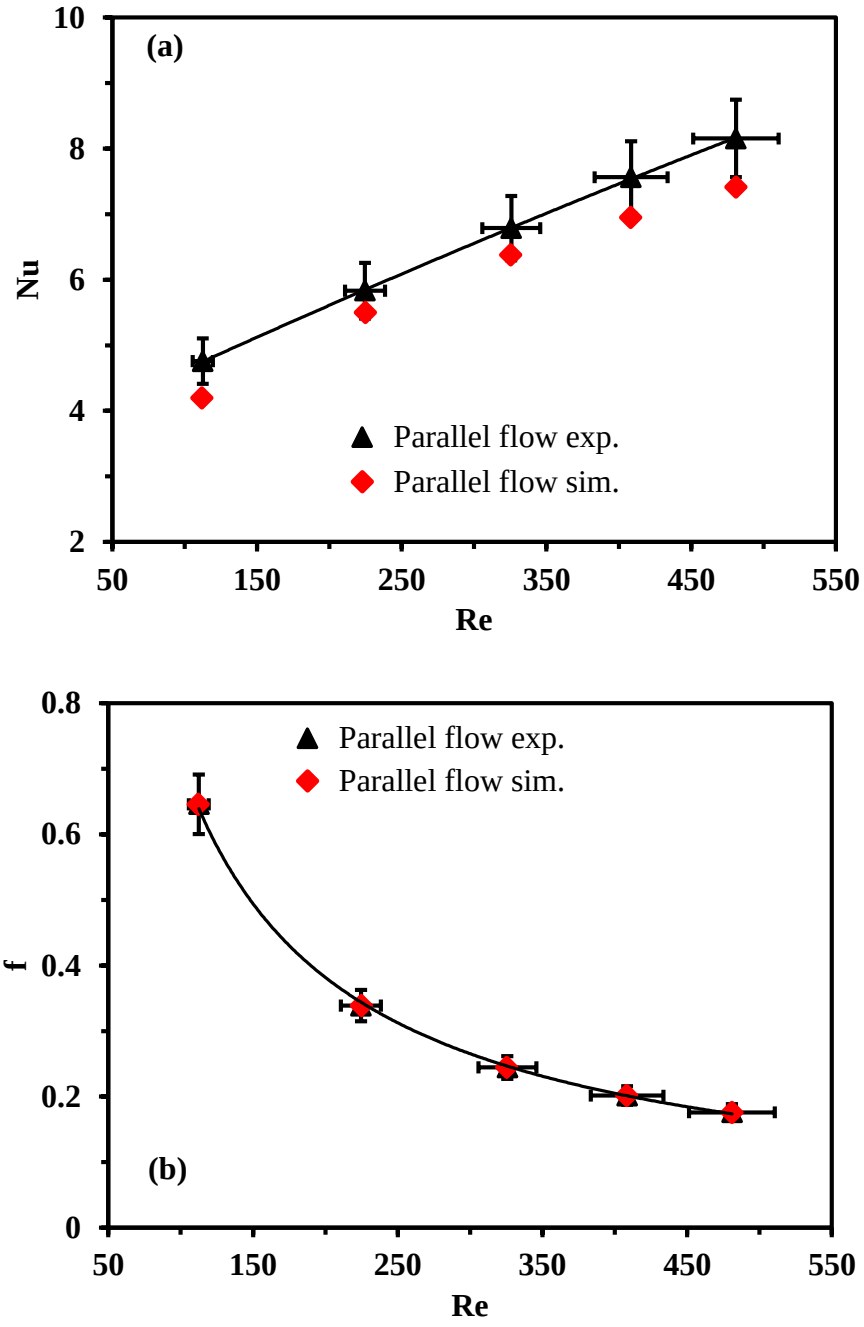

Figure 6.28 Comparison between experimental and numerical (a) Nu and (b) f for parallel flow mini-channel heat sink.

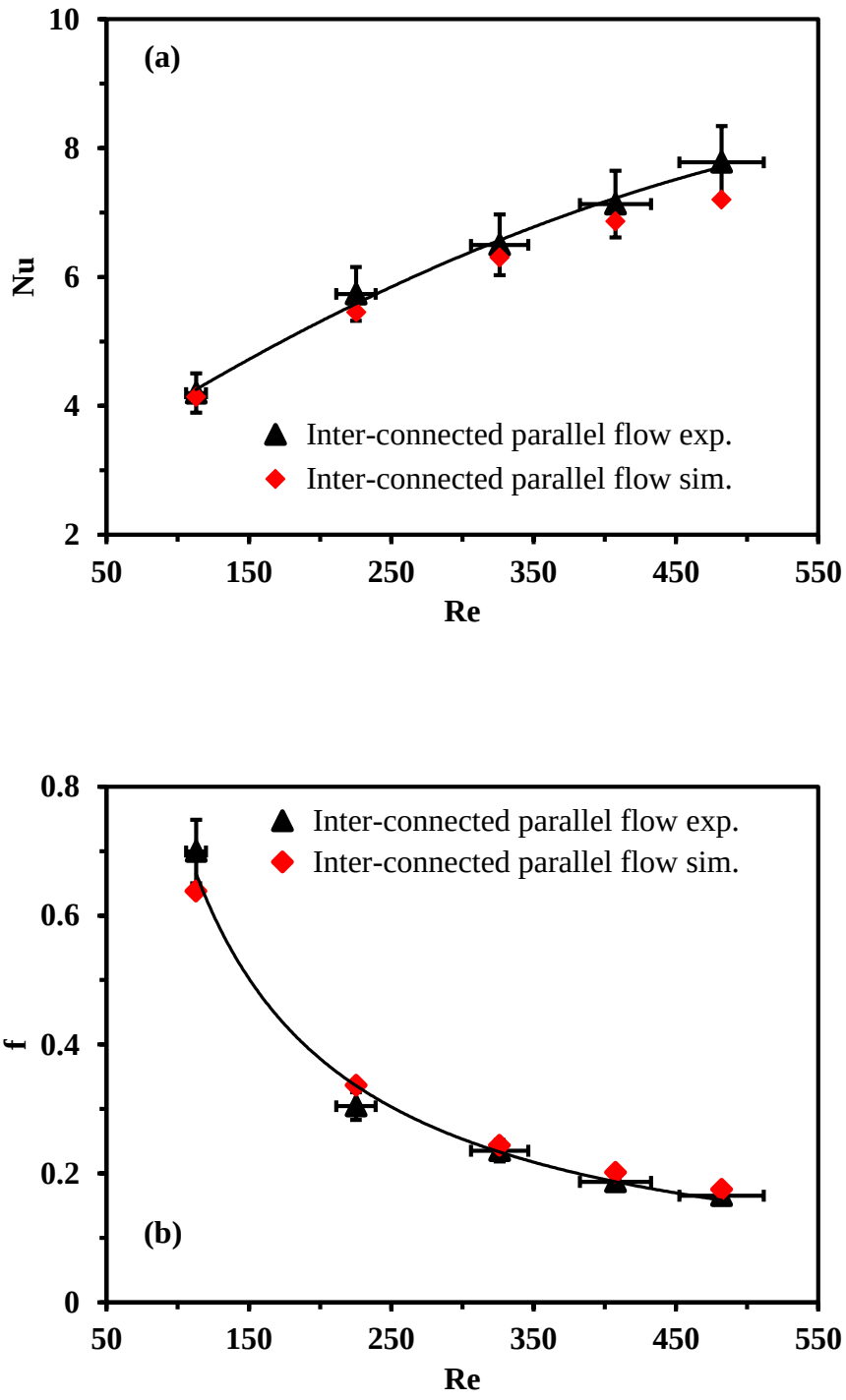

Figure 6.29 Comparison between experimental and numerical (a) Nu and (b) f for inter-connected parallel flow mini-channel heat sink.

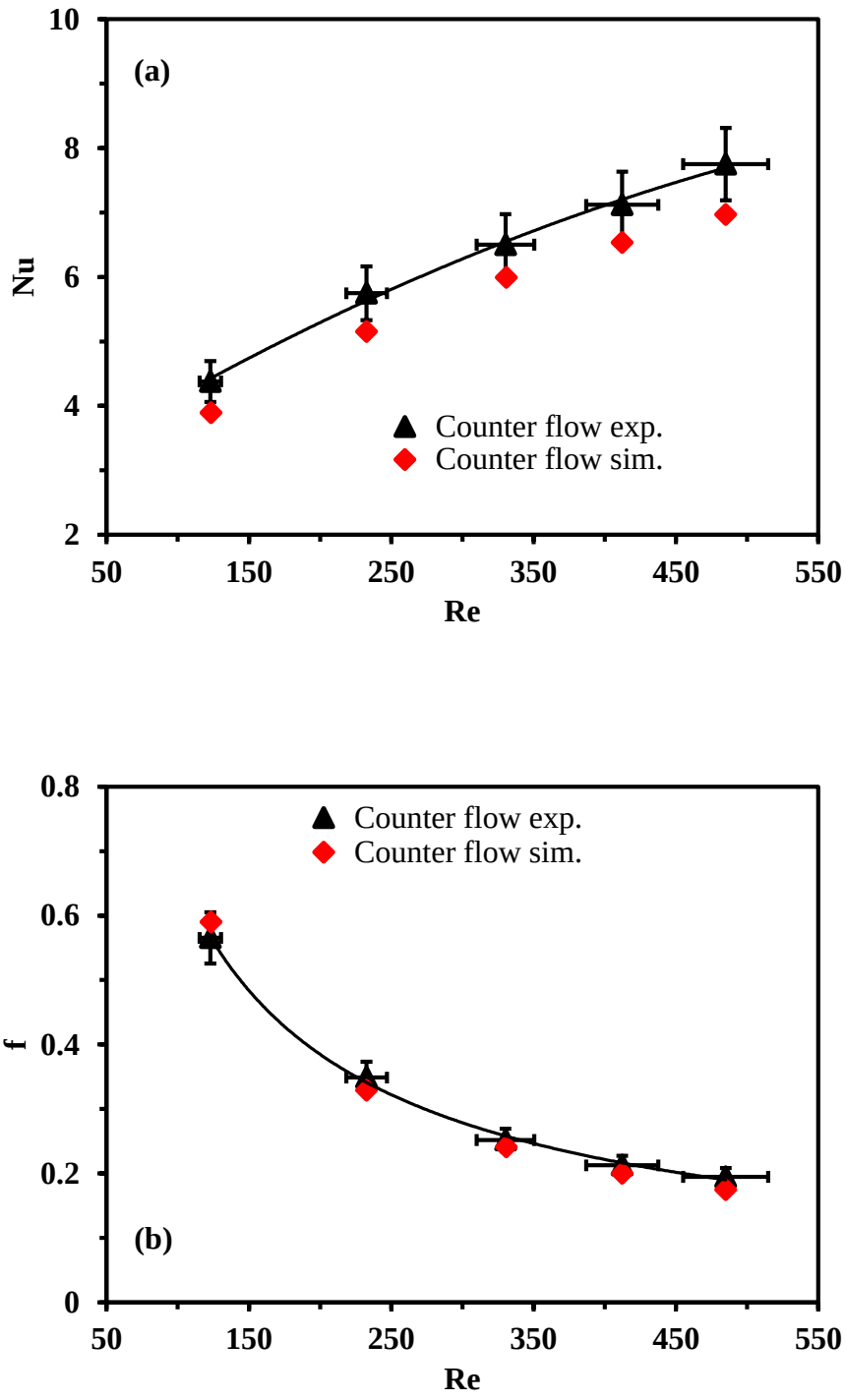

Figure 6.30 Comparison between experimental and numerical (a) Nu and (b) f for counter flow mini-channel heat sink.

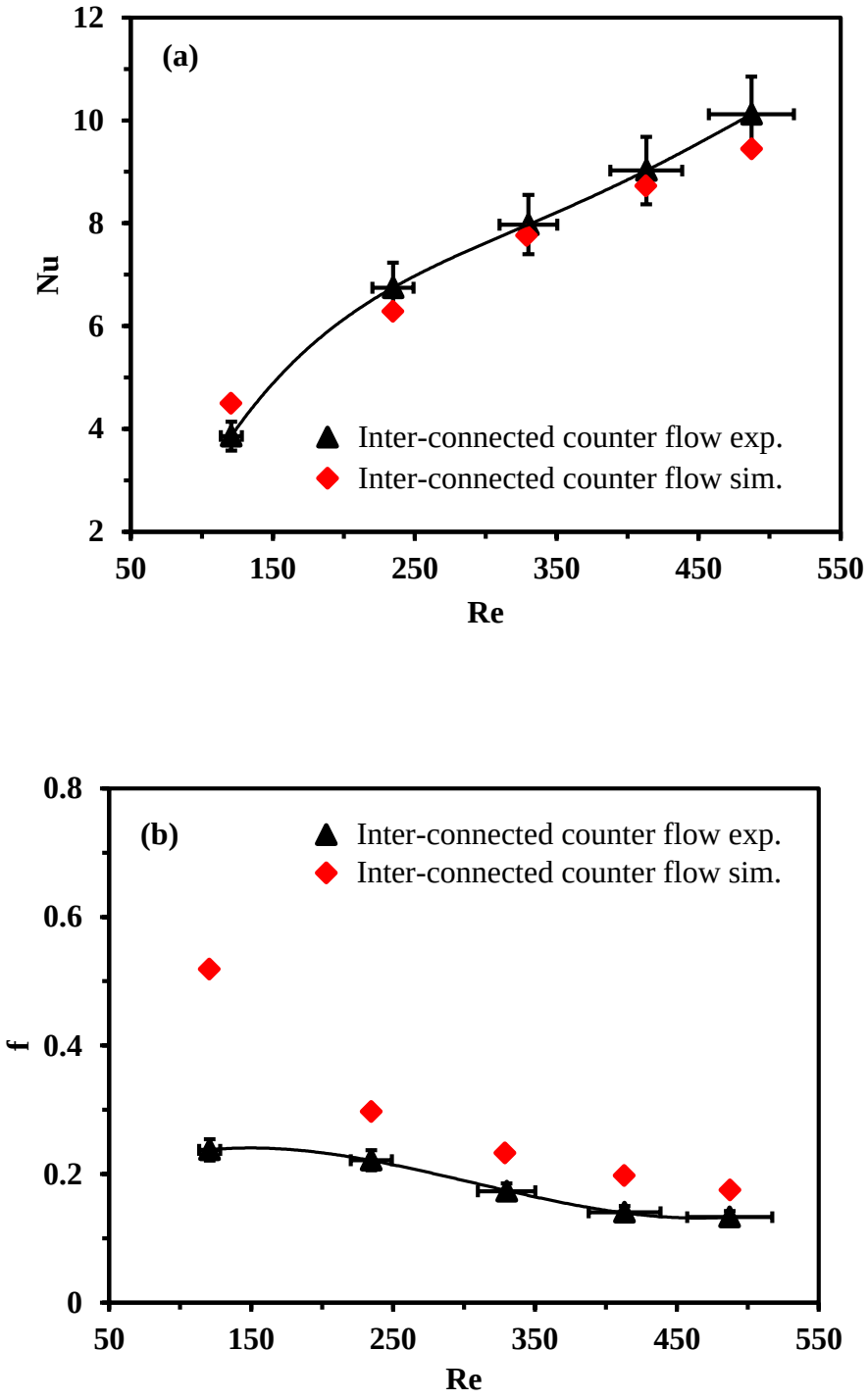

Figure 6.31 Comparison between experimental and numerical (a) Nu and (b) f for inter-connected counter flow mini-channel heat sink.

1.0%, 3.80%, and 4.36% for the conventional parallel flow, inter-connected parallel flow, and counter flow mini-channel heat sinks respectively. However, in case of inter-connected counter flow mini-channel, numerical model significantly over predicts the f values especially at lower Re compared to the experimental results as shown in the Figure 6.31 (b). This can be attributed to the slightly different coolant flow rates through the adjacent channels in actual experiments and also to the constant thermo-physical properties assumption in numerical modeling.

6.12 Summary

The effect of secondary flow on the thermal-hydraulic performance of parallel and counter flow mini-channel heat sinks have been experimentally examined under laminar flow regime. Two inter-connectors were made-up to enable transverse flow between two adjacent mini-channels. Average base surface temperature, overall Nusselt number, friction factor, overall thermal resistance, pumping power, entropy generation rate and performance evaluation criteria were calculated to quantify the effect of secondary flow on the heat transfer and flow friction of the parallel and counter flow mini-channel heat sink. Finally, experimental results were also compared with the numerical results. The following conclusions can be drawn from the experimental findings:

1. Substantial reduction of the substrate temperature was achieved, especially at higher Re. A maximum 3.12^{o}C temperature reduction was attained by enabling transverse flow in counter flow mini-channel heat sink at $Re = 480$.

2. At low Re, inter-connectors adversely affect the thermal performance of the mini-channel heat sink while at higher Re, enhanced thermal performance was achieved for the inter-connected mini-channel heat sink.

3. A maximum ~63.21% reduction in friction factor was recorded in case of inter-connected counter flow mini-channel heat sink at the lowest Re because of the substantial transverse flow. On the contrary, at the highest Re, a maximum ~24.40% reduction of friction factor was achieved for modified counter flow mini-channel heat sink compared to the conventional parallel flow mini-channel heat sink.

4. Overall thermal resistance followed the same trend as surface temperature for all configurations and modified counter flow mini-channel heat sink provided a maximum ~18.14% reduction in thermal resistance compared to the conventional parallel flow heat sink.

5. Conventional and inter-connected counter flow mini-channel heat sinks provided significant reduction in entropy generation rate, especially at higher Re.

6. The maximum value of PEC for inter-connected counter flow mini-channel heat sinks reached up to 1.36 at $Re = 480$.

7. Numerical model can better predict the thermal performance of the modified mini-channel heat sinks than the hydrodynamic performance, especially for inter-connected counter flow mini-channel heat sink.

CHAPTER 7 CONCLUSION

Three-dimensional conjugate heat transfer analysis and experimental investigation have been performed to characterize the thermal-hydraulic performance of the inter-connected parallel and counter flow mini-channel heat sink in the laminar flow regime ($Re = 150 - 1044$) under constant heat flux. From the numerical and experimental results, the following conclusions can be drawn.

7.1 The Effect of Inter-Connectors Width on the Overall Performance of Parallel and Counter Flow Mini-Channel Heat Sink

To quantify the effect of the inter-connector width on the fluid flow and heat transfer behavior of both parallel and counter flow heat sink, five different width of the inter-connector (case 1-5) were considered and for every inter-connector width, overall performance were compared based on friction factor, Nusselt number, non-dimensional pumping power, thermal resistance, and performance evaluation criteria (PEC). Based on the numerical investigation following conclusions can be summarized:

1. The inter-connector has a negligible effect on the thermal and hydraulic performance for parallel flow mini-channel heat sink because of the small pressure difference across the inter-connector which results in almost “no secondary flow” through the inter-connector.

2. In case of counter flow mini-channel heat sink, higher disruption of thermal and hydraulic boundary layer occurs because of higher secondary flow. At the same time, for low flow rate, coolant velocity reduces significantly in-between two inter-connectors which results in higher surface temperature along with less pressure drop.
3. The width of the inter-connector is an important geometric parameter to determine the significance of the cross flow on the Nu for both parallel and counter flow mini-channel heat sink. A maximum 36.43% increment of Nu for inter-connected counter flow heat sink was achieved for the highest inter-connectors width (case 5) and Re.
4. The pressure drop of the working fluid decreased significantly in inter-connected counter flow mini-channel heat sink especially at low Re; this reduction is more profound at the higher width of the inter-connector. For the highest inter-connectors width (case 5), a maximum 31.83% reduction of friction factor is recorded at $Re = 150$.
5. The maximum value of PEC for parallel flow mini-channel heat sink is ~0.99 for the highest inter-connectors width (case 5) whereas in case of counter flow heat sink with inter-connector, the value of PEC reached up to 1.33 for the same case and it shows an increasing trend with Re.

7.2 The Combined Effect of Inter-Connector Location and Width on the Overall Performance of Counter Flow Mini-Channel Heat Sink

The effects of inter-connectors location and width on the overall performance of counter flow mini-channel heat sink were examined numerically and compared with the

overall performance of the conventional counter flow mini-channel heat sink. Three different locations and for each location, three different inter-connectors widths (case 1-9) were chosen for the numerical modeling. The following conclusions can be drawn based on the numerical analysis:

1. The amount of secondary flow reduced gradually with the Re regardless of the inter-connectors location and width. Moreover, the amount of the secondary flow changed in descending order from the smaller to the higher length of zone 1 and zone 3, and in ascending order from the lower to the higher width of the inter-connectors.

2. For all inter-connected counter flow mini-channel heat sinks, friction factors (f) reduced significantly at lower Re compared to the conventional counter flow mini-channel heat sink because of higher secondary flow, whereas at higher Re, f became very comparable to case 0. This phenomenon increases with the inter-connectors width and decreases with the reduction of the length of zone 1 and 3. Maximum ~48.37% reduction in f was recorded for the lowest length of zone 1 and 3 and the highest inter-connectors width (case 3) at $Re = 150$ compared to case 0 while a maximum ~7.0% enhancement in f was recorded for highest length of zone 1 and 3 and the highest inter-connectors width (case 9) case 9 and at $Re = 1044$.

3. The inter-connected counter flow mini-channel heat sinks showed improved overall thermal performance compared to the conventional counter flow mini-channel heat sink, especially at higher Re. At $Re = 1044$, maximum ~45% enhancement in Nu

is detected for the intermediate length of zone 1 and 3 and the highest inter-connectors width (case 9). However, in cases of the smaller and intermediate length of zone 1 and 3 (case 1-6) and at low Re, the inter-connectors affect the Nu adversely.

4. Inter-connectors location and width have a substantial effect on the thermal performance of the counter flow mini-channel heat sinks. For the smallest length of zone 1 and 3 (case 1-3), the lowest inter-connectors width provides better thermal performance. On the contrary, for the intermediate and highest length of zone 1 and 3 (case 4-9) and at low Re, the lowest inter-connectors width gives better heat transfer performance while at higher Re, the highest inter-connectors width depicts better heat transfer performance.

5. For all inter-connected counter flow mini-channel heat sinks, a significant reduction in thermal resistance was recorded for any particular pumping power except for case 1-3 and $Re = 150$. A maximum ~48% reduction in pumping power was recorded for the lowest length of zone 1 and 3 and the highest inter-connectors width (case 3) compared to case 0 while a maximum ~29.48% reduction in thermal resistance was evident for the intermediate length of zone 1 and 3 and the highest inter-connectors width (case 6).

6. At low Re, PEC value changed in descending order from the lower to the higher width of the inter-connectors regardless of the inter-connectors location. However, at higher Re, higher PEC value was achieved for the higher width of the inter-connectors. At $Re = 150$, a maximum PEC value of ~1.22 was recorded for the

highest length of zone 1 and 3 and the lowest inter-connectors width (case 7), and at $Re = 1044$, a maximum PEC value of ~1.42 was recorded for the intermediate length of zone 1 and 3 and the highest inter-connectors width (case 6).

7.3 Experimental Investigation of Overall Performance of the Inter-Connected Parallel and Counter Flow Mini-Channel Heat Sink

The effect of secondary flow on the thermal-hydraulic performance of parallel and counter flow mini-channel heat sinks have been experimentally examined under laminar flow regime. Experimental results were also compared with the numerical results. The following conclusions can be drawn from the experimental findings:

1. Substantial reduction of the substrate temperature was achieved, especially at higher Re. A maximum 3.12^{o}C temperature reduction was attained by enabling transverse flow in counter flow mini-channel heat sink at $Re = 480$.

2. At low Re, inter-connectors adversely affect the thermal performance of the mini-channel heat sink while at higher Re, enhanced thermal performance was achieved for the inter-connected mini-channel heat sink.

3. A maximum ~63.21% reduction in friction factor was recorded in case of inter-connected counter flow mini-channel heat sink at the lowest Re because of the substantial transverse flow. On the contrary, at the highest Re, a maximum ~24.40% reduction of friction factor was achieved for modified heat sink compared to the conventional parallel flow mini-channel heat sink.

4. Overall thermal resistance followed the same trend as surface temperature for all configurations and modified counter flow mini-channel heat sink provided

a maximum ~18.14% reduction in thermal resistance compared to the conventional parallel flow heat sink.

5. Conventional counter flow and inter-connected counter flow mini-channel heat sinks provided significant reduction in entropy generation rate, especially at higher Re.

6. The maximum value of PEC for inter-connected counter flow mini-channel heat sinks reached up to 1.36 at $Re = 480$.

7. Numerical model can better predict the thermal performance of the modified mini-channel heat sinks than the hydrodynamic performance, especially for inter-connected counter flow mini-channel heat sink.

CHAPTER 8 FUTURE RESEARCH DIRECTIONS

In the present research, numerical and experimental investigation were performed to quantify the effect of the secondary flow on the overall thermal-hydraulic performance of the parallel and counter flow mini-channel heat sinks. However, there are many other parameters that are needed to be addressed to further improve the overall performance of the mini-channel heat sink utilizing secondary flow.

The following are suggested for future research:

1. To enhance the thermal-hydraulic performance of the mini-channel heat sink using secondary flow, the number of inter-connectors should be optimized.
2. In the current research, to enable counter flow through the adjacent channels in a multi-channel heat sink, new inlet-outlet plenum needs to be designed.
3. The effects of inter-connectors on the overall performance of the mini-channel heat sink in the two-phase flow regime need to be investigated.

REFERENCES

[1] G. E. Moore, “Cramming more components onto integrated circuits,” *Electronics*, vol. 38, no. 8, Apr. 1965.

[2] M. Bohr, “The new era of scaling in an SoC world,” in IEEE ISSCC Dig. Tech. Papers, Feb. 2009, pp. 22–27.

[3] S. G. Kandlikar, “Fundamental issues related to flow boiling in mini-channels and microchannels,” *Exp. Therm. Fluid Sci.*, vol. 26, no. 2–4, pp. 389–407, 2002.

[4] D. B. Tuckerman and R. F. W. Pease, “High-Performance Heat Sinking for VLSI,” no. 5, pp. 126–129, 1981.

[5] G. Wang, N. Qian, and G. Ding, “Enhancement in microchannel heat sink with bidirectional rib,” *Int. J. Heat Mass Transf.*, vol. 136, pp. 597–609, 2019.

[6] R. J. Phillips, “Forced-Convection, Liquid-Cooled, MicroChannel Heat Sinks,” 1988.

[7] W. Qu and I. Mudawar, “Experimental and numerical study of pressure drop and heat transfer in a single-phase micro-channel heat sink,” *Int. J. Heat Mass Transf.*, vol. 45, pp. 2549–2565, 2002.

[8] J. Li, G. P. Peterson, and P. Cheng, “Three-dimensional analysis of heat transfer in a micro-heat sink with single-phase flow,” *Int. J. Heat Mass Transf.*, vol. 47, no. 19–20, pp. 4215–4231, 2004.

[9] A. G. Fedorov and R. Viskanta, “Three-dimensional conjugate heat transfer in the

microchannel heat sink for electronic packaging," *Int. J. Heat Mass Transf.*, vol. 43, pp. 399-415, 2000.

[10] T. M. Adams, S. I. Abdel-Khalik, S. M. Jeter, and Z. H. Qureshi, "An experimental investigation of single-phase forced convection in microchannels," *Int. J. Heat Mass Transf.*, vol. 41, no. 6–7, pp. 851–857, 1998.

[11] P. Lee and S. V Garimella, "Thermally developing flow and heat transfer in rectangular microchannels of different aspect ratios," *Int. J. Heat Mass Transf.*, vol. 49, pp. 3060–3067, 2006.

[12] T. M. Harms, M. J. Kazmierczak, and F. M. Gerner, "Developing convective heat transfer in deep rectangular microchannels," *Int. J. Heat Fluid Flow*, vol. 20, pp. 149-157, 1999.

[13] H. Shen, C. C. Wang, and G. Xie, "A parametric study on thermal performance of microchannel heat sinks with internally vertical bifurcations in laminar liquid flow," *Int. J. Heat Mass Transf.*, vol. 117, pp. 487–497, 2018.

[14] T. D. J. Teng, "Comparisons of the heat transfer and pressure drop of the microchannel and mini-channel heat exchangers," *Heat Mass Transf.*, pp. 1311–1322, 2011.

[15] M. H. Sinks, A. Afzal, M. Samee, and S. A. Khan, "Comparative Heat Transfer Analysis in Different Comparative Heat Transfer Analysis in Different Mini-channel Heat Sinks," Int. *J. Recent Research Aspects*, vol. 4, no. December 2017, pp. 41–45.

[16] X. L. Xie, Z. J. Liu, Y. L. He, and W. Q. Tao, "Numerical study of laminar heat transfer and pressure drop characteristics in a water-cooled mini-channel heat sink,"

Appl. Therm. Eng., vol. 29, no. 1, pp. 64–74, 2009.

[17] X. L. Xie and W. Q. Tao, "Numerical Study of Turbulent Heat Transfer and Pressure Drop Characteristics in a Water-Cooled Mini-channel Heat Sink," *J. of Electronic Packaging*, vol. 129, no. September 2007, pp. 247–255.

[18] A. Tikadar, M. Hossain, and A. K. M. M. Morshed, "Numerical Investigation of Thermal Performance of a Water-Cooled Mini-channel Heat Sink for Different Chip Arrangement," *AIP Conf. Proc.*, vol. 050007, 2016.

[19] T. Saenen, "Effect of Flow Pulsation on the Heat Transfer Performance of a Minichannel Heat Sink," *J. Heat Transf.*, vol. 134, pp. 1–7, 2012.

[20] R. Fang and J. A. Khan, "Active Heat Transfer Enhancement in Single-Phase Microchannels by Using Synthetic Jets," *Journal of Thermal Science and Engineering Applications*, vol. 5, pp. 1–8, 2013.

[21] W. Li, F. Yang, T. Alam, X. Qu, B. Peng, J. Khan, and C. Li, "Enhanced flow boiling in microchannels using auxiliary channels and multiple micronozzles (I): Characterizations of flow boiling heat transfer," *Int. J. Heat Mass Transf.*, vol. 116, pp. 208–217, 2018.

[22] Y. L. Zhai, G. D. Xia, X. F. Liu, and Y. F. Li, "Exergy analysis and performance evaluation of flow and heat transfer in different micro heat sinks with complex structure," vol. 84, pp. 293–303, 2015.

[23] L. Chai, G. Xia, L. Wang, M. Zhou, and Z. Cui, "Heat transfer enhancement in microchannel heat sinks with periodic expansion-constriction cross-sections," *Int. J. Heat Mass Transf.*, vol. 62, no. 1, pp. 741–751, 2013.

[24] G. Croce and P. D. Agaro, "Numerical simulation of roughness effect on

microchannel heat transfer and pressure drop in laminar flow," *J. Phys. D: Appl. Phys.* vol. 38, pp. 1518-1538, 2005.

[25] A. Behnampour, O. A. Akbari, M. R. Safaei, M. Ghavami, A. Marzban, G. A. Sheikh Shabani, M. zarringhalam, and R. Mashayekhi, "Analysis of heat transfer and nanofluid fluid flow in microchannels with trapezoidal, rectangular and triangular shaped ribs," *Phys. E Low-Dimen. Syst. Nano.*, vol. 91, pp. 15–31, 2017.

[26] C. J. Ho, L. C. Wei, and Z. W. Li, "An experimental investigation of forced convective cooling performance of a microchannel heat sink with Al2O3/water nanofluid," *Appl. Therm. Eng.*, vol. 30, no. 2–3, pp. 96–103, 2010.

[27] M. Kalteh, A. Abbassi, M. Saffar-avval, A. Frijns, and A. Darhuber, "Experimental and numerical investigation of nanofluid forced convection inside a wide microchannel heat sink," *Appl. Therm. Eng.*, vol. 36, pp. 260–268, 2012.

[28] M. Khoshvaght-Aliabadi, M. Sahamiyan, M. Hesampour, O. Sartipzadeh, "Experimental study on cooling performance of sinusoidal-wavy mini-channel heat sink," *Appl. Therm. Eng.*, vol. 92, pp 50-61, 2016.

[29] G. Xia, Y. Zhai, and Z. Cui, "Numerical investigation of thermal enhancement in a micro heat sink with fan-shaped reentrant cavities and internal ribs," *Appl. Therm. Eng.*, vol. 58, no. 1–2, pp. 52–60, 2013.

[30] M. E. Steinke and S. G. Kandlikar, "Single-Phase Heat Transfer Enhancement Techniques in Micro-channel and Mini-channel Flows," *Microchannels and Minichannels, ICMM2004-2328, pp. 141-148*, 2004.

[31] J. L. Xu, Y. H. Gan, D. C. Zhang, and X. H. Li, "Microscale heat transfer enhancement using thermal boundary layer redeveloping concept," *Int. J. Heat Mass*

Transf., vol. 48, no. 9, pp. 1662–1674, 2005.

[32] Y. J. Lee, P. K. Singh, and P. S. Lee, "Fluid flow and heat transfer investigations on enhanced microchannel heat sink using oblique fins with parametric study," *Int. J. Heat Mass Transf.*, vol. 81, pp. 325–336, 2015.

[33] Y. Fan, P. Seng, and W. Chua, "Investigation on the influence of edge effect on flow and temperature uniformities in cylindrical oblique-finned mini-channel array," *Int. J. Heat Mass Transf.*, vol. 70, pp. 651–663, 2014.

[34] S. K. Oudah, A. Tikadar, R. Fang, K. Egab, and J. A. Khan, "Thermohydraulic characteristics of a knurled microchannel heat sink in single-phase regime," pp. 1425–1436, 2018.

[35] S. K Oudah, R. Fang, A. Tikadar, K. Egab, Chen Li, and J. A. Khan " The effects of hybrid sandblasting patterns on the heat transfer performance in a single-phase microchannel heat sink" *ASME 2017 International Mechanical Engineering Congress and Exposition*, Vol. 8, pp. V008T10A024, 2017.

[36] M. Xu, H. Lu, L. Gong, J. C. Chai, and X. Duan, "Parametric numerical study of the flow and heat transfer in microchannel with dimples ☆," *Int. Commun. Heat Mass Transf.*, vol. 76, pp. 348–357, 2016.

[37] H. E. Ahmed and M. I. Ahmed, "Optimum thermal design of triangular , trapezoidal and rectangular grooved microchannel heat sinks ☆," *Int. Commun. Heat Mass Transf.*, vol. 66, pp. 47–57, 2015.

[38] D. J. Schmitt, J. B. Taylor, A. L. Carrano, J. D. Kozak, and E. Hensel, "Experimental investigation of surface roughness microstructures and their effects on pressure drop characteristics in rectangular mini-channels," 2004.

[39] Y. Li, F. Zhang, B. Sunden, and G. Xie, “Laminar thermal performance of microchannel heat sinks with constructal vertical Y-shaped bifurcation plates,” *Appl. Therm. Eng.*, vol. 73, no. 1, pp. 185–195, 2014.

[40] G. Xie, H. Shen, and C. Wang, “Parametric study on thermal performance of microchannel heat sinks with internal vertical Y-shaped bifurcations,” *Int. J. Heat Mass Transf.*, vol. 90, pp. 948–958, 2015.

[41] Y. Sui, C. J. Teo, P. S. Lee, Y. T. Chew, and C. Shu, “Fluid flow and heat transfer in wavy microchannels,” *Int. J. Heat Mass Transf.*, vol. 53, no. 13–14, pp. 2760–2772, 2010.

[42] H. A. Mohammed, P. Gunnasegaran, and N. H. Shuaib, “Numerical simulation of heat transfer enhancement in wavy microchannel heat sink ☆,” *Int. Commun. Heat Mass Transf.*, vol. 38, no. 1, pp. 63–68, 2011.

[43] M. Dehghan, M. Daneshipour, M. S. Valipour, and R. Rafee, “Enhancing heat transfer in microchannel heat sinks using converging flow passages,” *Energy Convers. Manag.*, vol. 92, pp. 244–250, 2015.

[44] V. S. Duryodhan, A. Singh, S. G. Singh, and A. Agrawal, “Convective heat transfer in diverging and converging microchannels,” *Int. J. Heat Mass Transf.*, vol. 80, pp. 424–438, 2015.

[45] H. Ghaedamini, P. S. Lee, and C. J. Teo, “Developing forced convection in converging – diverging microchannels,” *Int. J. Heat Mass Transf.*, vol. 65, pp. 491–499, 2013.

[46] G. Xia, L. Chai, H. Wang, M. Zhou, and Z. Cui, “Optimum thermal design of microchannel heat sink with triangular reentrant cavities,” *Appl. Therm. Eng.*, vol.

31, no. 6–7, pp. 1208–1219, 2016.

[47] G. Xia, L. Chai, M. Zhou, and H. Wang, “Effects of structural parameters on fluid flow and heat transfer in a microchannel with aligned fan-shaped reentrant cavities,” *Int. J. Therm. Sci.*, vol. 50, no. 3, pp. 411–419, 2011.

[48] L. Chai, G. Xia, M. Zhou, and J. Li, “Numerical simulation of fluid flow and heat transfer in a microchannel heat sink with offset fan-shaped reentrant cavities in sidewall,” *Int. Commun. Heat Mass Transf.*, vol. 38, no. 5, pp. 577–584, 2011.

[49] G. D. Xia, J. Jiang, J. Wang, Y. L. Zhai, and D. D. Ma, “Effects of different geometric structures on fluid flow and heat transfer performance in microchannel heat sinks,” vol. 80, pp. 439–447, 2015.

[50] S.U.S. Choi, “Enhancing thermal conductivity of fluids with nanoparticles, American Society of Mechanical Engineers,” *Fluids Engineering Division (Publication) FED*, pp. 99–105, 1995.

[51] S. P. Jang and S. U. S. Choi, “Cooling performance of a microchannel heat sink with nanofluids,” *Appl. Therm. Eng.*, vol. 26, pp. 2457–2463, 2006.

[52] R. Chein and J. Chuang, “Experimental microchannel heat sink performance studies using nanofluids,” *Int. J. Therm. Sci.*, vol. 46, pp. 57–66, 2007.

[53] M. Saeed and M. Kim, “Heat transfer enhancement using nanofluids (Al_2O_3 -H_2O) in mini-channel heatsinks,” *Int. J. Heat Mass Transf.*, vol. 120, pp. 671–682, 2018.

[54] Y. Lee, P. Lee, and S. Chou, "Experimental investigation of oblique finned micro-channel heat sink$^+$," *2010 12th IEEE Intersociety Conference on Thermal and Thermomechanical Phenomena in Electronic Systems*, Las Vegas, NV, 2010, pp. 1-7.

[55] Y. J. Lee and P. S. Lee, “Enhanced thermal transport in microchannel using oblique fins,” *J. Heat Transf.*, vol. 134, October 2012.

[56] P. S. Lee, “Numerical study of fluid flow and heat transfer in the enhanced microchannel with oblique fins,” *J. Heat Transf.*, vol. 135, pp. 1–10, April 2013.

[57] Y. Fan, P. Seng, L. Jin, and W. Chua, “A simulation and experimental study of fluid flow and heat transfer on cylindrical oblique-finned heat sink,” *Int. J. Heat Mass Transf.*, vol. 61, pp. 62–72, 2013.

[58] Y. Fan, P. Seng, L. Jin, W. Chua, and D. Zhang, “A parametric investigation of heat transfer and friction characteristics in cylindrical oblique fin minichannel heat sink,” *Int. J. Heat Mass Transf.*, vol. 68, pp. 567–584, 2014.

[59] N. R. Kuppusamy, R. Saidur, N. N. N. Ghazali, “Numerical study of thermal enhancement in micro-channel heat sink with secondary flow,” *Int. J. Heat Mass Transf.*, vol. 78, pp. 216-223, 2014.

[60] Z. Lin, P. Seng, P. Kumar, and N. Mou, “Investigation of fluid flow and heat transfer in wavy micro-channels with alternating secondary branches,” *Int. J. Heat Mass Transf.*, vol. 101, pp. 1316–1330, 2016.

[61] M. Hossain and A. K. M. M. Morshed, “Enhanced Heat Sink with Geometry Induced Wall-jet,” *AIP Conf. Proc.*, vol. 1754, 2016.

[62] S. Soleimanikutanaei, E. Ghasemisahebi, and C. Lin, “Numerical study of heat transfer enhancement using transverse microchannels in a heat sink,” *Int. J. Therm. Sci.*, vol. 125, no. July 2017, pp. 89–100, 2018.

[63] W. Mohd, A. Aziz, N. Azwadi, C. Sidik, S. Mat, J. Sultan, Y. Petra, and J. Semarak, “A comprehensive study on heat transfer enhancement in microchannel heat sink

with secondary channel," *Int. Commun. Heat Mass Transf.*, vol. 99, no. November, pp. 62–81, 2018.

[64] S. Deldar and M. Khoshvaght-aliabadi, "Analysis of flow and heat transfer of different miniature chambers with / and / without rectangular pin: Numerical investigation with empirical validation," *Appl. Therm. Eng.*, vol. 150, no. December 2018, pp. 923–936, 2019.

[65] M. A. Ahmed, M. Z. Yusoff, K. C. Ng, and N. H. Shuaib, "Effect of corrugation profile on the thermal-hydraulic performance of corrugated channels using CuO-water nanofluid," *Case Stud. Therm. Eng.*, vol. 4, no. February 2016, pp. 65–75, 2014.

[66] M. Nojoomizadeh, A. Karimipour, M. Firouzi, and M. Afrand, "Investigation of permeability and porosity effects on the slip velocity and convection heat transfer rate of Fe_3O_4/water nanofluid flow in a microchannel while its lower half filled by a porous medium," *Int. J. Heat Mass Transf.*, vol. 119, pp. 891–906, 2018.

[67] L. Chai and L. Wang, "Thermal-hydraulic performance of interrupted microchannel heat sinks with different rib geometries in transverse microchambers," *Int. J. Therm. Sci.*, vol. 127, no. February, pp. 201–212, 2018.

[68] T. J. John, B. Mathew, and H. Hegab, "Parametric study on the combined thermal and hydraulic performance of single phase micro pin-fin heat sinks part I: Square and circle geometries," *Int. J. Therm. Sci.*, vol. 49, no. 11, pp. 2177–2190, 2010.

[69] W. A. Khan, J. R. Culham, and M. M. Yovanovich, "Optimization of Microchannel Heat Sinks Using Entropy Generation Minimization Method," no. April 2006, 2014.

[70] A. Behnampour, O. A. Akbari, M. R. Safaei, M. Ghavami, A. Marzban, G. A.

Sheikh Shabani, M. zarringhalam, and R. Mashayekhi, “Analysis of heat transfer and nanofluid fluid flow in microchannels with trapezoidal, rectangular and triangular shaped ribs,” *Phys. E Low-Dimensional Syst. Nanostructures*, vol. 91, no. February, pp. 15–31, 2017.

[71] A. Arabpour, A. Karimipour, D. Toghraie, and O. A. Akbari, “Investigation into the effects of slip boundary condition on nanofluid flow in a double-layer microchannel,” *J. Therm. Anal. Calorim.*, vol. 131, no. 3, pp. 2975–2991, 2018.

[72] Reference Manual, ANSYS FLUENT 6.1, “SIMPLE vs. SIMPLEC” section 24.8.1.

[73] C. J. Ho and W. C. Chen, “An experimental study on thermal performance of Al2O3/water nanofluid in a mini-channel heat sink,” *Appl. Therm. Eng.*, vol. 50, no. 1, pp. 516–522, 2013.

[74] M. K. Moraveji and R. M. Ardehali, “CFD modeling (comparing single and two-phase approaches) on thermal performance of Al_2O_3/water nano fluid in mini-channel heat sink,” *Int. Commun. Heat Mass Transf.*, vol. 44, pp. 157–164, 2013.

[75] R. K. Shah, A.L.London “Laminar Flow Forced Convection in Ducts,” *Academic Press. New Tork*, 1975.

[76] B. Kanargi, P. S. Lee, and C. Yap, “A numerical and experimental investigation of heat transfer and fluid flow characteristics of an air-cooled oblique-finned heat sink,” *Int. J. Heat Mass Transf.*, vol. 116, pp. 393–416, 2018.

[77] P.N.N. Shankar, M.D.D. Deshpande, Fluid mechanics in the driven cavity, *Annu. Rev. Fluid Mech.* pp. 93–136, 2018.

[78] A. Tikadar, U. Najeeb, T. C. Paul, S. K. Oudah, A. S. Salman, A. M. Abir, L. A. Carrilho, and J. A. Khan, “Numerical investigation of heat transfer and pressure drop

in nuclear fuel rod with three-dimensional surface roughness," *Int. J. Heat Mass Transf.*, vol. 126, pp. 493–507, 2018.

[79] T. Jeng, S. Tzeng, and Q. Huang, "Heat transfer performance of the pin – fin heat sink filled with packed brass beads under a vertical oncoming flow," *Int. J. Heat Mass Transf.*, vol. 86, pp. 531–541, 2015.

[80] A. S. Salman and J. A. Khan, "experimental investigation of spray cooling heat transfer on circular grooved," *ASME 2017 Heat Transf. Summer Conf.*, vol. 2, pp. 1–9, 2017.

[81] F. R. Menter, "Two-equation eddy-viscosity turbulence models for engineering applications," AIAA Journal, vol. 32, no. 8, 1994.

[82] F. R. Menter, "Improved two-equation k – ω turbulence models for aerodynamic flows," *NASA Technical Memorandum 103975*, 1992.

[83] F. R. Menter, D. Layer, and F. W. Analysis, "Influence of freestream values *on* k – ω *turbulence model predictions*," *AIAA Journal*, vol. 30, no. 6, pp. 1657–1659.

[84] O. A. Akbari, D. Toghraie, and A. Karimipour, "Numerical simulation of heat transfer and turbulent flow of water nanofluids copper oxide in rectangular microchannel with semi-attached rib," vol. 8, no. 4, pp. 1–25, 2016.

[85] Reference Manual, ANSYS FLUENT, "Turbulence Modelling," section 12.5.2.

[86] Reference Manual, ANSYS FLUENT, "Turbulence Modelling," section 25.9.1.

[87] Reference Manual, ANSYS FLUENT, "Turbulence Modelling," section 25.9.2.

APPENDIX A TURBULENT FLOW MODEL

For turbulent flow simulation, SST $k-\omega$ turbulence model developed by Menter [81-82] was chosen. SST $k-\omega$ turbulence model is a two equation eddy viscosity turbulence model which is a mixture of $k-\omega$ and $k-\varepsilon$ model to use the advantages of both models. The standard $k-\omega$ model is more accurate inside the boundary layer; hence this model was successfully implemented to simulate the turbulent flow with moderate adverse pressure gradients but this model is too sensitive to the inlet free stream turbulence properties. In the free stream region, the standard $k-\varepsilon$ model is more accurate than the standard $k-\omega$ model. To utilize the advantage of both standard $k-\omega$, and $k-\varepsilon$ model, the SST model divides the flow domain into two regions: (1) near wall region, and (2) free stream region, and use a blending function to switch between *k-ε,* and *k-ω* models in the preferred region. The blending function is designed to be one in the near wall region, which activate the standard $k-\omega$ model, and zero away from the wall boundary, which activate the $k-\varepsilon$ model [83]. This numerical method solves the Reynolds Averaged Navier Stokes equations along with the equations of *k, ω,* and *ε*.

Before establishing the simplified governing equations for the turbulent flow field and heat transfer, following assumptions were incorporated:

(i) the fluid is incompressible.

(ii) steady fluid flow and heat transfer.

(iii) the properties of the working fluid are constant, and are not function of temperature.

(iv) negligible convection and radiation heat loss.

(v) effect of gravity, and any other body forces are negligible.

(vi) effect of viscous dissipation is taken into account.

Governing Equations

Based on the above assumptions, the conservation equations of mass, momentum, and energy to describe the turbulent fluid flow and heat transfer are expressed as follows,

Continuity equation:

$$\frac{\partial}{(\partial x_i)(\rho u_i)} = 0 \tag{A.1}$$

Momentum equation:

$$\frac{\partial}{\partial x_j}(\rho u_i u_j) = -\frac{\partial P}{\partial x_i} + \frac{\partial}{\partial x_j}\left[\mu\left(\frac{\partial u_i}{\partial x_j} + \frac{\partial u_j}{\partial x_i}\right)\right] + \frac{\partial}{\partial x_j}\left(-\rho\overline{u_i' u_j'}\right) \tag{A.2}$$

Energy equation :

$$\frac{\partial}{\partial x_i}(\rho u_i h_{tot}) = \frac{\partial}{\partial x_i}\left(k\frac{\partial T}{\partial x_i} - \rho\overline{u_i' h}\right) + \mu\Phi - \frac{\partial \mu_i}{\partial x_j}\left(\rho\overline{u_i' u_j'}\right) \tag{A.3}$$

where, Φ is the energy dissipation term which is defined as:

$$\Phi = \left(\frac{\partial u_i}{\partial x_j} + \frac{\partial u_j}{\partial x_i}\right)\frac{\partial u_i}{\partial x_j} \tag{A.4}$$

where, u and x are the velocity and direction components $i, j = 1, 2$ (for 2D), ρ is the fluid density, μ is the fluid viscosity, k is the fluid thermal conductivity, h_{tot} is the mean total viscosity, and $\rho\overline{u_i'h}$, $\rho\overline{u_i'u_j'}$ are the additional term due to the turbulent fluxes.

The transport equations for the shear stress transport $k-\omega$ model are as follows,

$$\frac{\partial}{\partial x_i}(\rho k u_i) = \frac{\partial}{\partial x_j}\left(\Gamma_k \frac{\partial k}{\partial x_j}\right) + \tilde{G}_k - Y_k + S_k \tag{A.5}$$

$$\frac{\partial}{\partial x_i}(\rho \omega k u_i) = \frac{\partial}{\partial x_j}\left(g_\omega \frac{\partial \omega}{\partial x_j}\right) + G_\omega - Y_\omega + D_\omega + S_\omega \tag{A.6}$$

where, $\tilde{G}_k$ and G_ω are the production of the turbulence kinetic energy due to mean velocity gradient and the generation of specific dissipation rate, ω respectively.

$$\tilde{G}_k = \min(G_k, 10\rho\beta^* k\omega) \tag{A.7}$$

where, G_k is defined in the same manner as in the standard $k-\omega$ model,

$$G_k = -\frac{\rho\overline{u_i'u_j'}(\partial u_j)}{\partial x_i} \tag{A.8}$$

The production of specific dissipation rate, ω is represented as follows,

$$G_\omega = \frac{\alpha}{\vartheta_t} G_k \tag{A.9}$$

$$\alpha = \frac{\alpha_\infty}{\alpha^*}\left[\frac{\alpha_o + Re_t/R_\omega}{1 + Re_t/R_\omega}\right] \tag{A.10}$$

where, R_ω is a constant.

The coefficient α^* damps the turbulent viscosity causing a low-Reynolds number correction.

$$\alpha^* = \alpha_\infty^* \left(\frac{\alpha_o^* + Re_t/R_k}{1 + Re_t/R_k}\right) \quad \text{(A.11)}$$

where, $\alpha_o^* = \frac{\beta_i}{3}$ and $Re_t = \frac{\rho k}{\mu \omega}$ (A.12)

In the case of high Reynolds number, α^*= α_∞^* =1

$$\alpha_\infty = F_1 \alpha_{\infty,1} + (1 - F_1)\alpha_{\infty,2} \quad \text{(A.13)}$$

where, $\alpha_{\infty,1} = \frac{\beta_{i,1}}{\beta_\infty^*} - \frac{k^2}{\sigma_{\omega,1}\sqrt{\beta_\infty^*}}$ and $\alpha_{\infty,2} = \frac{\beta_{i,2}}{\beta_\infty^*} - \frac{k^2}{\sigma_{\omega,2}\sqrt{\beta_\infty^*}}$ (A.14)

The effective diffusivity (Γ) of k and ω in SST $k - \omega$ model are defined as below,

$$\Gamma_k = \mu + \frac{\mu_t}{\sigma_k} \quad \text{(A.15)}$$

$$\Gamma_\omega = \mu + \frac{\mu_t}{\sigma_\omega} \quad \text{(A.16)}$$

Here, μ_t is the turbulent viscosity which is defined as follows,

$$\mu_t = \frac{\rho k}{\omega} \frac{1}{\max\left[\frac{1}{\alpha^*}, \frac{SF_2}{a_1 \omega}\right]} \quad \text{(A.17)}$$

where, S is the strain rate magnitude.

The turbulent Prandtl number for k is, $\sigma_k = \frac{1}{\frac{F_1}{\sigma_{k,1}} + \frac{1-F_1}{\sigma_{k,2}}}$ (A.18)

Moreover, the turbulent Prandtl number of ω is, $\sigma_\omega = \frac{1}{\frac{F_1}{\sigma_{\omega,1}} + \frac{1-F_1}{\sigma_{\omega,2}}}$ (A.19)

The blending functions, F_1 and F_2 are defined as follows,

$$F_1 = \tanh(\Phi_1^4) \quad \text{(A.20)}$$

$$\Phi_1 = \min\left[\max\left(\frac{\sqrt{k}}{0.09\omega y}, \frac{500\mu}{\rho y^2 \omega}\right), \frac{4\rho k}{\sigma_{\omega,2} D_\omega^+ y^2}\right] \quad \text{(A.21)}$$

$$D_\omega^+ = \max\left[2\rho \frac{1}{\sigma_{\omega,2}} \frac{1}{\omega} \frac{\partial k}{\partial x_j} \frac{\partial \omega}{\partial x_j}, 10^{-10}\right] \quad \text{(A.22)}$$

$$F_2 = \tanh(\Phi_2^2) \quad \text{(A.23)}$$

$$\Phi_2 = \max\left[2\frac{\sqrt{k}}{0.09\omega y}, \frac{500\mu}{\rho y^2 \omega}\right] \quad \text{(A.24)}$$

where, y is the distance to the next surface and D_ω^+ is the positive portion of the cross diffusion term which is defined as

$$D_\omega = 2(1 - F_1)\rho\sigma_{\omega,2} \frac{1}{\omega} \frac{\partial k}{\partial x_j} \frac{\partial \omega}{\partial x_j} \quad \text{(A.25)}$$

Dissipation of the turbulent kinetic energy is, $Y_k = \rho\beta^* k\omega$ (A.26)

Dissipation of the specific dissipation rate ω is,

$Y_\omega = \rho\beta\omega^2$ where, $\beta_i = F_1\beta_{i,1} + (1 - F_1)\beta_{i,2}$ (A.27)

In equation 9 and 10, S_k and S_ω are user defined source term which are zero in this case.

All the model constants are summarized in Table A.1.

Table A.1 Values of the constants used in SST k − ω turbulence model [84-85]

$\alpha_0 = {}^1/_9$	$R_\omega = 2.95$	$R_k = 6$	$\beta_i = 0.072$	α^*=1
α_∞^* =1	$k = 0.41$	$\beta_\infty^* = 0.09$	$\beta_{i,1} = 0.075$	$\beta_{i,2} = 0.0828$
$\sigma_{\omega,1} = 2.0$	$\sigma_{\omega,2} = 1.168$	$a_1 = 0.31$	$\sigma_{k,1} = 1.176$	$\sigma_{k,2}$=1.0
	$\alpha_\infty = 0.52$	$R_\beta = 8$	$\zeta^* = 1.5$	

The numerical analysis was performed by the finite volume based commercial computational fluid dynamics software ANSYS FLUENT 16.0. The solution domain was discretized by the second-order upwind scheme for momentum equations, turbulent kinetic energy and specific dissipation rate. For the pressure-velocity coupling, semi-implicit method for pressure linked equations (SIMPLE) algorithm was used for its stable solving capabilities of turbulent flow [86]. To ensure stable solution within minimal computational time, under-relaxation factors for pressure, momentum, and turbulent kinetic energy equations were set at 0.3, 0.7, and 0.8 respectively [87], which are default values of under-relaxation factors of the solver. When the normalized residual values were less than 10^{-5} for all variables except for the energy equation, the solution was considered to be converged. For the energy equation, the convergence criterion was set at 10^{-6}.

APPENDIX B DETAIL DRAWING OF THE HEAT SINK

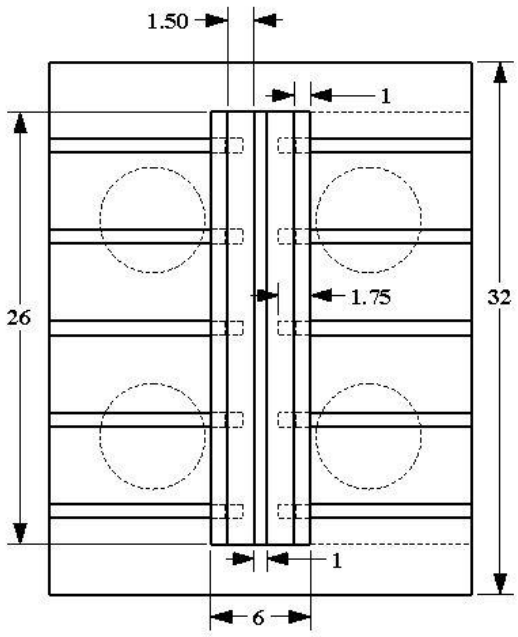

Figure B.1 Top view of the mini-channel heat sink.

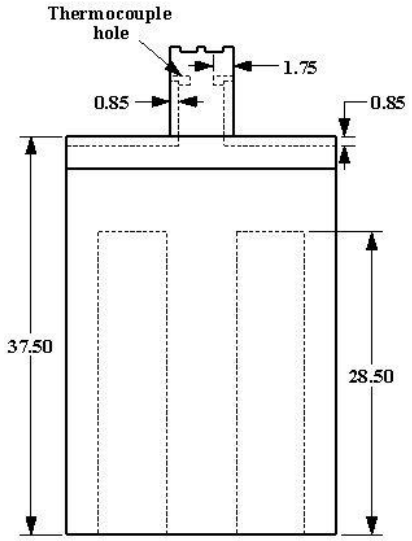

Figure B.2 Front view of the mini-channel heat sink.

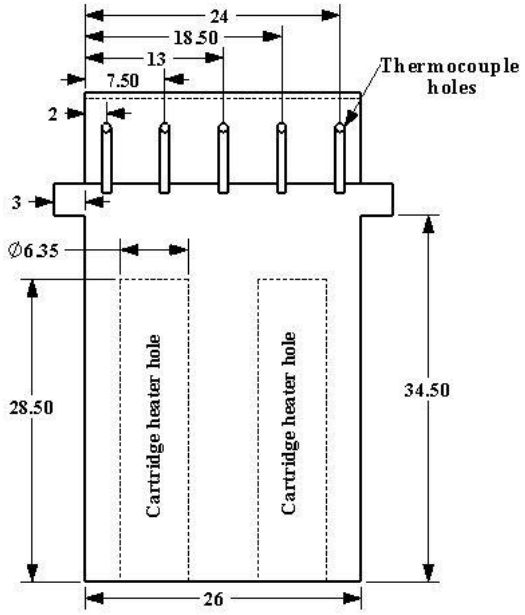

Figure B.3 Side view of the mini-channel heat sink.

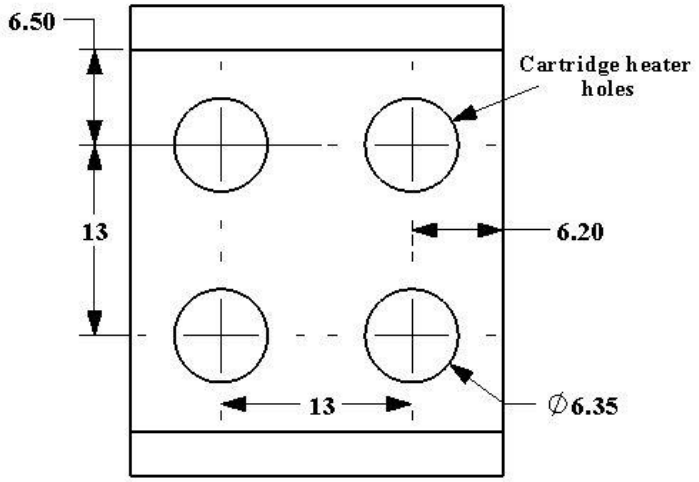

Figure B.4 Bottom view of the mini-channel heat sink.